EXPANDING THE SCOPE OF NONPARAXIAL SCALAR DIFFRACTION THEORY

A THESIS SUBMITTED TO
THE GRADUATE SCHOOL OF NATURAL AND APPLIED SCIENCES
OF
MIDDLE EAST TECHNICAL UNIVERSITY

BY

METE GÜNÖVEN

IN PARTIAL FULFILLMENT OF THE REQUIREMENTS
FOR
THE DEGREE OF DOCTOR OF PHILOSOPHY
IN
MICRO AND NANOTECHNOLOGY

JANUARY 2020

Approval of the thesis:

EXPANDING THE SCOPE OF NONPARAXIAL SCALAR DIFFRACTION THEORY

submitted by **METE GÜNÖVEN** in partial fulfillment of the requirements for the degree of **Doctor of Philosophy in Micro and Nanotechnology, Middle East Technical University** by,

Prof. Dr. Halil Kalıpçılar
Dean, Graduate School of **Natural and Applied Sciences** _____

Prof. Dr. Almıla Güvenç Yazıcıoğlu
Head of the Department, **Micro and Nanotechnology** _____

Prof. Dr. Raşit Turan
Supervisor, **Physics, METU** _____

Prof. Dr. Hüsnü Emrah Ünalan
Co-Supervisor, **Metallurgical and Materials Eng., METU** _____

Examining Committee Members:

Assoc. Prof. Dr. Alpan Bek
Physics, METU _____

Prof. Dr. Raşit Turan
Physics, METU _____

Assoc. Prof. Dr. Özgür Ergül
Electrical and Electronics Engineering, METU _____

Assoc. Prof. Dr. Halil Berberoğlu
Physics, Ankara Hacı Bayram Veli University _____

Assoc. Prof. Dr. Kemal Efe Eseller
Electrical and Electronics Engineering, Atılım University _____

Date: 31.01.2020

I hereby declare that all information in this document has been obtained and presented in accordance with academic rules and ethical conduct. I also declare that, as required by these rules and conduct, I have fully cited and referenced all material and results that are not original to this work.

Name, Last name : Mete Günöven

Signature :

ABSTRACT

EXPANDING THE SCOPE OF NONPARAXIAL SCALAR DIFFRACTION THEORY

Günöven, Mete
Doctor of Philosophy, Micro and Nanotechnology
Supervisor: Prof. Dr. Raşit Turan
Co-Supervisor: Prof. Dr. Hüsnü Emrah Ünalan

January 2020, 107 pages

The modelling of light scattering from rough textured surfaces is important to assess the light trapping performances of thin film solar cells. In this regard, Harvey-Shack scalar scattering theory is a method of choice established in the solar cell community. It can be used to calculate the angular intensity distribution both in reflection and in transmission, by using the Fourier transform of the optical phase light accumulates while traversing the rough surface texture to evaluate a far-field approximation of the Rayleigh-Sommerfeld scalar diffraction integral, observed on a hemisphere centered around the sample aperture.

In this work, different versions of the Harvey-Shack scalar scattering theory are implemented, and their results are compared to actual angular intensity measurements, using a purpose-built high-resolution goniometric instrument. These comparisons generally show remarkable quantitave predictions, which validate the overall approach.

However, differences with the measurements suggest that the optical phase accumulation could benefit from an additional correction factor for rough surfaces

containing lateral feature sizes on the order of the wavelength, which can be attributed to effective medium effects. Moreover, secondary interactions within the surface topography are shown to be a mechanism that partly redistributes scattered power, affecting angular intensity distribution results. These mechanisms emerge as the two main limitations of the generalized nonparaxial Harvey-Shack theory in the far-field.

When applied to the scattering into an optically denser medium, this model predicts polar angle regions where no scattering should accur, regardless of the angle of incidence or the roughness of the texture. This prediction points at a limitation of light trapping using rough textured interfaces.

Furthermore, the near-aperture and near-field terms of the Rayleigh-Sommerfeld scalar diffraction integral were investigated using a modification to the generalized Harvey-Shack theory computational algorithm. Within the restrictions of its scalar nature, this novel method can be an important tool for the characterization of near-field diffraction for thin film solar cells and many other problems.

Keywords: Harvey-Shack Theory, Scalar Scattering Theory, Rayleigh-Sommerfeld Diffraction Integral, Near-Field Terms, Light Trapping

ÖZ

PARAKSİYAL OLMAYAN SKALAR KIRILMA TEORİSİNİN KAPSAMININ GENİŞLETİLMESİ

Günöven, Mete
Doktora, Mikro ve Nanoteknoloji
Tez Yöneticisi: Prof. Dr. Raşit Turan
Ortak Tez Yöneticisi: Prof. Dr. Hüsnü Emrah Ünalan

Ocak 2020, 107 sayfa

Işığın pürüzlü yapılardan saçılmasının modellenmesi ince film güneş gözelerinin ışık hapsetme performansının değerlendirilmesi açısından önemlidir. Bu bağlamda Harvey-Shack skalar saçılım teorisi güneş enerjisi araştırmalarında sıklıkla kullanılan bir yöntemdir. Işığın pürüzlü yüzeyden yansırken veya geçerken kazandığı optik fazın Fourier dönüşümü kullanılarak, Rayleigh-Sommerfeld kırılma integralinin örneğin bulunduğu açıklık çevresindeki bir yarımküre üzerinde gözlemlenmesi sayesinde ışığın açısal yoğunluk dağılımının hesaplanmasında kullanılır.

Bu çalışmada, Harvey-Shack skalar saçılım teorisinin çeşitli türleri açısal dağılım hesaplamasına uygulanmış, ve bu sonuçlar özel üretilen yüksek açısal çözünürlüklü saçılım düzeneği ile yapılan ölçümlerle karşılaştırılmıştır. Karşılaştırmalar genel olarak yöntemin kayda değer niceliksel öngörüler verdiğini doğrulamaktadır.

Öte yandan, ölçümler ile aradaki bazı farklılıklar, optik faz kazanımının, yanal boyutları dalgaboyu seviyesinde olan yüksek pürüzlü yüzeylerden geçerken, efektif ortam etkilerini içerecek bir düzeltme katsayısından faydalanabileceğini

önermektedir. Ayrıca, yüzey topografisi üzerindeki ikincil etkileşimlerin saçılan gücü kısmen farklı doğrultulara dağıtarak açısal ışık yoğunluğu dağılımını değiştiren bir mekanizma olduğu gösterilmiştir.Bu iki mekanizma, genelleştirilmiş paraksiyal olmayan Harvey-Shack teorisinin uzak-alandaki temel kısıtlamaları olarak ortaya çıkmaktadır.

Optik kırılma indisi daha yüksek bir malzemeye doğru saçılıma uyarlandığında, bu model belli bir kutupsal açı bölgesine hiç saçılma olmadığını öngörmektedir. Bu öngörü, rastgele pürüzlü yapılarının genel olarak ışık hapsetme performansları bir sınırına işaret etmektedir.

Öte yandan, Rayleigh-Sommerfeld kırılma integralinin yakın-alan ve açıklık-yakınında önem kazanan terimleri, genelleştirilmiş Harvey-Shack sayısal hesap algoritmasına yapılan bir değişiklikle incelenmiştir. Skalar doğasının getirdiği sınırlamalar dahilinde, önerilen bu yeni yöntem ince film güneş gözelerinin ve başka birçok yakın-alan kırılma probleminin modellemesinde kullanılabilir.

Anahtar Kelimeler: Harvey-Shack Teorisi, Skalar Saçılım Teorisi, Rayleigh-Sommerfeld Kırılma İntegrali, Yakın-Alan, Işık Hapsetme

To the faithful departed

Ömer, Ali Zahit, Lebibe, Rukiye, Baise, Tahsin

Emel, Susam

Lux æterna luceat eis

ACKNOWLEDGMENTS

First and foremost, I would like to thank my family for their unwavering support and the unrequited love they have shown me from the day I was born. I must also thank Pelin for walking a small part of the way with me.

I would like to thank Fırat Es, Hande Çiftpınar, Hisham Nasser, Zeynep and Olgu Demircioğlu, Mehmet Karaman, Serim İlday, Engin Özkol, Ergi Dönerçark, Salar Sedani, Ozan Aydın, Çiğdem Doğru and Özden Başar Balbaşı, my dear colleagues at GÜNAM, with whom I shared many fond memories over the years. I also would like to thank Mona Zolfaghari Borra, Murat Öztürk, Özge Demirbaş, Fırat İdikut, Alim Yolalmaz and Hüseyin Umut Tepe, my fellow mates at the NanoOptics lab; as well as Sinan Gündoğdu, Mustafa Elçi, and Seval Arslan from the Bilkent QCL project, for their help and friendship.

I owe a heartfelt gratitude to Kutlu Kutluer for the invaluable Labview codes, Mustafa Kulakçı for his warm welcome, Mustafa Ünal for his extraordinary samples, and Ece Kuyululu for the chocolates.

Our department assistants Alper İnce, Melda İşler Binay and Yeliz Galioğlu, and our dear GÜNAM secretary Buket Gökbakan have always been benevolent and dependable to overcome many an administrative hurdle.

I am grateful to Kurtuluş Abak and Kamil Çınar, my fellow Ph.D. inmates, for their camaraderie, as well as for seamlessly filling the sorely missed function of a post-doc with their deep and wide knowledge.

I am most obliged to Prof. Dr. Atilla Aydınlı for his supervision and his sincere life advices. I really appreciate Dr. Ertuğrul Alp, my uncle, for the engineering insight he brought at key moments, and for proof-reading my work. I wish to express my heartfelt gratitude to Ali Günöven, my father and industrial design teacher, who has brought his immense workshop acumen to help me design and build the angular light

intensity meter instrument, which proved to have a precision almost beyond the tools he used to create it.

I would like to thank Assoc. Prof. Dr. Özgür Ergül for monitoring my progress and the fruitful discussions, and Assoc. Prof. Dr. Kemal Efe Eseller and Assoc. Prof. Dr. Halil Berberoğlu for the interest they showed in my work.

Last but not least, I would like to express my most sincere gratitude to my two thesis advisors. Prof. Dr. Raşit Turan let me be a part of the GÜNAM research staff for five long years, and has never wavered in his patience and trust for me through my days of adversity. Assoc. Prof. Dr. Alpan Bek has been constant source of reassurance and guidance with his immediate physical insights. I should have consulted both of them more frequently. I owe both of them a huge debt for not letting me abandon this endeavor. Thank you.

TABLE OF CONTENTS

ABSTRACT v

ÖZ vii

ACKNOWLEDGMENTS x

TABLE OF CONTENTS xii

LIST OF TABLES xv

LIST OF FIGURES xvi

LIST OF ABBREVIATIONS xx

CHAPTERS

1 INTRODUCTION 1

1.1 Surface scatter phenomena 1

1.2 Light trapping in solar cells 1

1.3 Organization of this dissertation 4

2 SURFACE MORPHOLOGY AND ITS INTERACTION WITH LIGHT. DEFINITIONS. 5

2.1 Introduction 5

2.2 Snell's law and Fresnel equations 5

2.2.1 Multiple incoherent reflection coefficients 7

2.3 Diffraction phenomena in periodic ordered structures 8

2.4 Randomly textured surfaces and their statistical quantities 9

2.5 Definitions of radiometric quantities 11

2.5.1 Intensity 12

2.5.2 Radiance 14

3 EXPERIMENTAL WORK 15
3.1 Surface topography characterization by atomic force microscopy 15
3.2 Surface preparation 16
3.3 Goniometer: instrumentation and AID measurements 18
4 ON HARVEY-SHACK SCALAR SCATTERING THEORY 23
4.1 Introduction 23
4.2 Review of Harvey-Shack scalar scattering theory 25
4.2.1 Diffraction from an empty aperture observed on a hemisphere 25
4.2.2 Radiant angular power distribution 28
4.2.3 Harvey's original surface scatter theory 31
4.2.4 Direct phase screen approach and its discrete implementation 32
4.2.5 Surface autocorrelation method 39
4.3 Generalized Harvey-Shack theory 42
4.4 Discussion on limitations and improvements to GHS theory 50
4.4.1 An effective medium correction factor? 50
4.4.2 Effects of secondary interactions 56
4.5 Scattering into optically denser media 60
4.6 Conclusion 62
5 INVESTIGATION OF NEAR-FIELD TERMS 65
5.1 Introduction 65
5.2 Revisiting near-field terms of the Rayleigh-Sommerfeld integral 67
5.2.1 Case 1: r=5000μm, n_i=1.87→n_s=1, θ_i=15.508° (θ_t=30°) 70
5.2.2 Case 2: r=50μm, n_i=1.87→n_s=1, θ_i=15.508° (θ_t=30°) 72
5.2.3 Case 3: r=5μm, n_i=1→n_s=1.87, 15.508° (θ_t=30°) 74

5.2.4 Case 4: r=5 μm with window function, n_i=1.87→n_s=1, 15.508° (θ_t=30°)76

5.2.5 Case 5: r=5 μm with window function, n_i=1.87→n_s=1, θ_i=30° (θ_t=15.508°) 77

5.3 Total intensity distribution 79

5.4 Conclusion 81

6 CONCLUSIONS AND FUTURE PROSPECTS 83

REFERENCES 87

APPENDICES

A. Measurement calibrations and corrections 99

A.1 Intensity measurement calibrations 99

A.2 Peak signal level corrections to account for lock-in time constant 102

B. Circling the Square: elements partly outside the diffraction hemisphere 103

C. Spectral leakage problems 105

CURRICULUM VITAE 107

LIST OF TABLES

TABLES

Table 3.1 Surface roughness σ and autocorrelation length acl extracted from AFM topography images. Asterisks indicate values taken from the optically relevant part of two-Gaussian fit of radial autocorrelation function. 16

Table 4.1 Empirical corrective coefficients, for normal incidence transmission, obtained using a dichotomous search optimization. Asterisks indicate values taken from the optically relevant part of two-Gaussian fit of radial autocorrelation function. 52

LIST OF FIGURES

FIGURES

Figure 1.1. a) Principle of light scattering in thin film solar cells. b) Absorption enhancement that can be obtained by ideal light trapping, compared to a single pass without any light trapping, for c-Si absorber layers of 1 and 5 μm thicknesses. 2
Figure 2.1. Snell's law 6
Figure 2.2. Multiple beams reflected from and transmitted through a non-absorbing dielectric slab. 7
Figure 2.3. Sinusoidal 1D grating. 8
Figure 2.4. Height profile, PSDF, ACF, σ, acl, and their Fourier transform relations. Adapted from [52,60]. 11
Figure 2.5. Scattering geometry, in spherical coordinates, drawn here for the reflection hemisphere. 12
Figure 2.6. a) AID, b) TID 13
Figure 3.1. AFM images, height and slope angle distributions 17
Figure 3.2. a) General schematic of instrumentation, shown for AID in transmission measurement. b) Aperture width and sample thickness minimizing multiple reflection effects, shown for AID in reflection measurement. c) Photograph of the goniometric instrument. 19
Figure 4.1. Geometric configuration of the incident plane wave, diffracting aperture and the observation hemisphere. Adapted from [52,55]. 26
Figure 4.2. Irradiance inside hemispheric collector area elements expressed in direction cosine space. 28
Figure 4.3. OHS interface optical path difference accumulation model. 32
Figure 4.4. 2D FFT operation and associated direction cosine coordinates. 33
Figure 4.5. Azimuthal projection algorithm for isotropic samples. a) Position of an element with respect to the unshifted center in 2D space b) Because of circular symmetry, only radial distance of elements needs to be considered, flattening the problem to 1D c) applying the shift due to the angle of incidence d) position of the

specular beam e) resulting AID, after division by the solid angles corresponding to each element with respect to shifted center. 35
Figure 4.6. AID in reflection (right) and in transmission (left), respectively for incidence and refraction angles of 0°, 30° and 60°. Symbols represent calculations according to the OHS algorithm in (4.20), lines represent measurements. For reflection calculations, incidence is through air; for transmission, incidence is through glass (n=1.52 for samples A, B, C) or Al:ZnO (n=1.87 for samples D, E). Dashed lines represent a Lambertian intensity distribution weighted by fR,T. Note the absence of data of a few degrees around the angle of incidence for reflected AID measurements, where the detector arm blocks incident laser beam. 37
Figure 4.7. Comparison of AID calculated with OHS pupil function using DPS (blue squares) and ACF (red triangles) methods, together with angular measurements (line) for samples B and D. 41
Figure 4.8. Diffraction angles in reflection and transmission predicted by OHS and GHS theories for normally incident light (λ=532 nm) on a Si pyramid surface with varied facet angles, and compared to reflection and refraction angles. n1=1 n2=3.5. Partly adapted from [51]. 43
Figure 4.9. GHS interface optical path difference accumulation model..... 44
Figure 4.10. Comparison of OHS and GHS pupil functions. a) Reflection into n=1, for 0°, 30° and 60° incidence angles. b) Transmission from n_1=1.52 to n_2=1, for 0°, 30° and 60° refraction angles. c) Transmission from n_1=1 to n_2=1.52, for 0°, 30° and 60° incidence angles. 47
Figure 4.11. AID in reflection (right) and in transmission (left), respectively for incidence and refraction angles of 0°, 30° and 60°. Symbols represent calculations according to the GHS algorithm in (4.31), lines represent measurements. For reflection calculations, incidence is through air; for transmission, incidence is through glass (n=1.52, for samples A, B, C) or Al:ZnO (n=1.87, for samples D, E). Dashed lines represent a Lambertian intensity distribution weighted by fR,T. 48
Figure 4.12. AID in transmission, for refraction angles of 0°, 30° and 60°, for samples D and E, calculated with optimized corrective coefficients (red triangles)

for fitting measurements (lines), and without the corrective coefficient (blue squares). 53
Figure 4.13. Phase accumulation on pyramid facets with different facet angles and sizes. Colors stand for the optical phase accumulated when light traverses each profile. Dotted lines suggest an equivalent height profile, encompassing effective medium effects 54
Figure 4.14. a) Illustration of secondary interactions on a pyramid-like surface texture, top view. b) Side view of goniometer aperture illustrating a secondary interaction from the surface topography (dark green line) or sides of the aperture with different radii (lighter green lines). 57
Figure 4.15. Left: AID measurements with s polarizer (red), p polarizer (green) and without polarizer (blue) in front of the detector. Incident beam is s polarized. Right: s/no polarizer and p/no polarizer ratios, measured using 3mm and 6mm diameter aperture sizes. 58
Figure 4.16. GHS pupil function, with respect to scatter angle, transmission from n_1=1.87 to n_2=1, for 0°, 30° and 60° incidence angles. 60
Figure 4.17. AID calculations for light scattering from sample D, for 0° and 30° incidence from air. Blue lines show transmission into ns=1.87, red lines show reflection into air, (green) lines show reflection measurements. 61
Figure 5.1. Top: Geometric visualization of near-field terms A, C and D. The $l - r + \alpha x' + \beta y'$ quantity in term D corresponds to the small distance in bright green. Bottom: Geometric visualization of the direction cosine space (black) centered on the real, aperture space (orange), with distances r (red) and l (blue). 69
Figure 5.2. Select calculation steps for r=5000μm, θ_i=15.508° 71
Figure 5.3. Diffraction geometries with a) r=50μm, b) r=5μm observation radii, under θ_i=15.508 incidence angle (θ_t=30°) 72
Figure 5.4. Select calculation steps for r=50μm, θ_i=15.508° (θ_t=30°) 73
Figure 5.5. Select calculation steps for r=5μm, θ_i=15.508° (θ_t=30°) 75
Figure 5.6. 2D Nuttall [n=16] window [102] placed at the center of an [N=256] square matrix. The rest of the matrix elements are filled with zeros. 76

Figure 5.7. Results for r=5μm, θ_i=15.508°, using a central Nuttall window function 77
Figure 5.8. Results for r=5μm, θ_i=30°, using a central Nuttall window function... 78
Figure 5.9. TID for sample D, with incidence angle θ_i=30°. (blue) and (green) show results respectively for transmission and reflection, for r=5μm, using a central Nuttall window function. (red) shows a TID for transmission calculated in the far-field. (black) and (pink) curves represent Lambertian distributions, calculated using Equation (2.9) and weighted by fR,T, respectively for transmission and reflection. 80
Figure A.1. Angular measurements for normal incidence transmission for sample D, with and without a diffuser film in front of the optical fiber. The scatter signal has been normalized with the incident signal and the larger (film) collector solid angle. 99
Figure A.2. Coupling losses for a) relatively homogeneous diffuse incident light and b) direct laser beam aligned to the center of the diffuser film. 100
Figure A.3. Lock-in measurement error and its correction. The measurement is not fast enough to a) increase to and b) decrease to the correct signal level. 102
Figure A.4. Peak signal level correction points. 103
Figure B.1. Matrix elements partly inside the unit circle. 104
Figure C.1. a) Phase screen resulting from normal incidence reflection for sample A, and b) its corresponding 2D power distribution map. c) and d) The same results with a tapered cosine (Tukey) window function (with parameter 0.1) [102] applied to the AFM image. 106

LIST OF ABBREVIATIONS

ABBREVIATIONS

ACF	Autocorrelation function
acl	Autocorrelation length
AFM	Atomic force microscopy
AID	Angular intensity distribution
AIT	Aluminum induced texturing
DPS	Direct phase screen
FFT	Fast Fourier transform
GHS	Generalized Harvey-Shack
OHS	Original Harvey-Shack
NF	Near-field
PSDF	Power spectral density function
RS	Rayleigh-Sommerfeld
SST	Scalar scattering theory
TID	Total intensity distribution

CHAPTER 1

INTRODUCTION

"Once you have tasted flight you will walk the earth with your eyes turned skyward; for there you have been, and there you will long to return."
Leonardo da Vinci

1.1 Surface scatter phenomena

The scattering of electromagnetic radiation is an important phenomenon in numerous areas of technology. Radars use radio waves to study the signal reflected back from distant objects to determine their positions and movements [1]. Scattering of microwaves is used in a variety of remote sensing applications such as in meteorology or geophysical sciences [2-5], or archeology [6,7], to name a few. Optical applications use surface scattering as a powerful characterization tool in non-contact metrology [8], or study its detrimental effects in x-ray and EUV imaging [9-11] and stray light reduction systems [12]. Scattering is even studied for realistic rendering of surfaces in computer graphics [13].

1.2 Light trapping in solar cells

The design of solar cell devices is fundamentally made around the compromise of balancing light absorption and carrier collection [14]. Increasing the thickness of the active absorber layer increases the number of absorbed photons (and generated minority carriers) through Beer-Lambert law. However, a thicker absorber layer is not ideal for the electronic performance of the device, as generated minority carriers

must diffuse (or drift) through the active layer to be collected, and bulk recombination losses are proportional to layer thickness.

The ideal solution to this compromise is found through the concept of light trapping, which consists of increasing the average path length that light travels inside the absorbing layer, without increasing the physical thickness. In thin film solar cells, this is usually achieved by the scattering of incident light from textured interfaces with micrometer to sub-micrometer size lateral features, as illustrated in Figure 1.1.

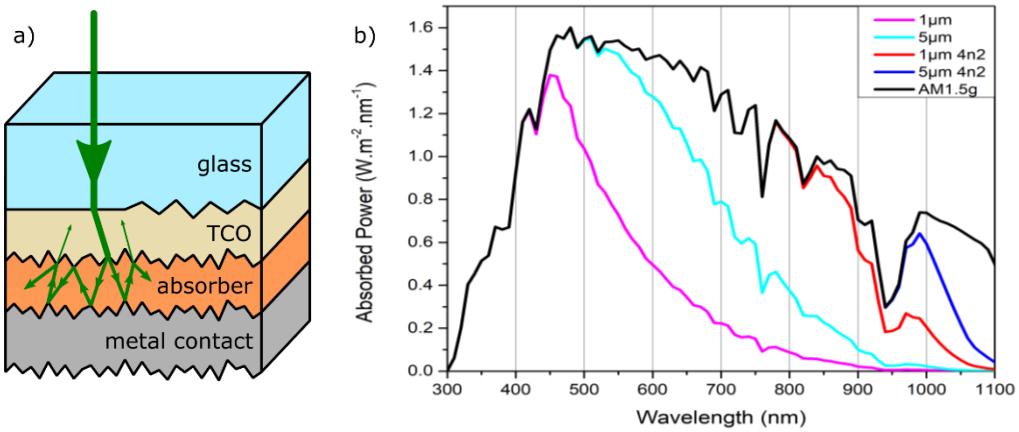

Figure 1.1. a) Principle of light scattering in thin film solar cells. b) Absorption enhancement that can be obtained by ideal light trapping, compared to a single pass without any light trapping, for c-Si absorber layers of 1 and 5 µm thicknesses.

The optimal absorption enhancement corresponds to the Yablonovitch limit [15,16], which is obtained if the incident light were to be completely randomized across all optical modes (or polar angles). This full randomization can be shown to increase the average path length by 2 (compared to a single perpendicular pass), or by 4 if a lossless back reflector is also present. After full randomization, the escape probability of photons at the front surface is reduced to $1/n^2$, thanks to total internal reflections inside the medium of higher refractive index n, where the escape cone is small. Thus, the maximum amount of path length, absorption and photocurrent enhancement that can be attained is $4n^2$ for poorly absorbed photon energies just above the semiconductor bandgap. This maximum enhancement is illustrated in Figure 1.1b), where the spectral portion of AM1.5g solar irradiance [17] absorbed

by 1 μm and 5 μm thick mc-Si layers are plotted, using c-Si absorption coefficient [18], with optimal $4n^2$ light trapping and with no light trapping at all.

However, this level of randomization in a single pass has not been achieved over a broad spectral range in thin film solar cells, neither using traditional random textures [19,20] nor more novel periodic or plasmonic structures [20-26]. Simply increasing surface roughness to improve high-angle scattering is often detrimental to the material quality of subsequent layers, and degrades the electronic performance of the device [27].

Significant efforts have been made in the last decade to better understand and optimize such nanotextured interfaces [26,28-51]. In order to optimize such textures, it is desirable to have a modelling approach which is accurate, computationally accessible and relatively parameter-free, to predict the angular distribution of light after scattering from randomly and/or orderly textured interfaces, with arbitrary roughness, into slabs of material of arbitrary thickness, arbitrary refractive index, and for arbitrary incidence angles.

After this decades-long period of investigation, a method of choice that got established in the solar cell community for the modelling of light scattering is the Harvey-Shack nonparaxial scalar scattering theory (SST) [42-59]. This scalar approach gives up some of the physical exactitude of rigorous electromagnetic methods that solve Maxwell's equations, such as the coupling between electric and magnetic fields in an electromagnetic wave and boundary conditions at the rough surface, but generally makes up for it in terms of its simplicity, accuracy, range of roughness validity, and ease of applicability for random textures.

This leads to the main motivation of this dissertation: to apply the Harvey-Shack nonparaxial SST to modelling the scattering of light from such rough textures as those employed in solar cells, and to test and expand its various domains of applicability.

1.3 Organization of this dissertation

In chapter 2, some useful quantities regarding surface morphology and its interaction with light will be introduced, and relevant radiometric quantities regarding the exchange of radiation between two surfaces will be defined.

In chapter 3, experimental details regarding the preparation of nanotextured samples, characterization of surface microtopography using atomic force microscopy, and instrumentation for angular intensity distribution measurements will be presented.

In chapter 4, which is the central chapter of this dissertation, Harvey's scalar surface scattering theory will be derived and implemented. This computationally efficient method uses Fourier transforms on the optical phase light accumulates while traversing the rough texture to evaluate a modified Rayleigh-Sommerfeld (RS) diffraction integral. Various versions of this method were implemented and compared to actual far-field angular intensity measurements. These comparisons reveal two notable deviations. The first one concerns rough textures with lateral feature sizes on the order of the wavelength, which can be linked to effective medium effects. The second one is explained by a redistribution of part of scattered power, which has been experimentally linked to secondary interactions within the surface topography.

In chapter 5, terms that are important when the observation point is near the aperture and in the near-field and that are usually left out of the RS diffraction integral will be analyzed using a modification to the approach developed for the nonparaxial generalized Harvey-Shack theory.

CHAPTER 2

SURFACE MORPHOLOGY AND ITS INTERACTION WITH LIGHT. DEFINITIONS.

"What does the dosimeter say?
3.6 roentgen, but that's as high as the meter...
3.6. Not great, not terrible."
Chernobyl miniseries

2.1 Introduction

The purpose of this chapter is to establish some basic notions on the interaction of light with surfaces, surface statistics and radiometric terms that are going to find use throughout the rest of this dissertation.

Since the scattering of light into different angles due to surface textures is being investigated, the scope of this dissertation will be limited to the purely photonic cases of non-absorptive, dielectric sample surfaces that are free from additional scattering mechanisms such as plasmonic interactions, or from attenuation due to absorption. Therefore, throughout the rest of this dissertation, relative magnetic permeabilities μ_r of studied materials reduce to unity, and relative dielectric permittivities ε_r can be replaced by the square of the real part of the refractive index n^2.

2.2 Snell's law and Fresnel equations

The interaction of a monochromatic plane wave of vacuum wavelength λ_0 incident on an optically flat surface separating two materials with different refractive indices,

as illustrated in Figure 2.1, is the result of Maxwell's equations and their boundary conditions. Here, "optically flat" means that any roughness protrusion from the flat surface is much smaller than the wavelength.

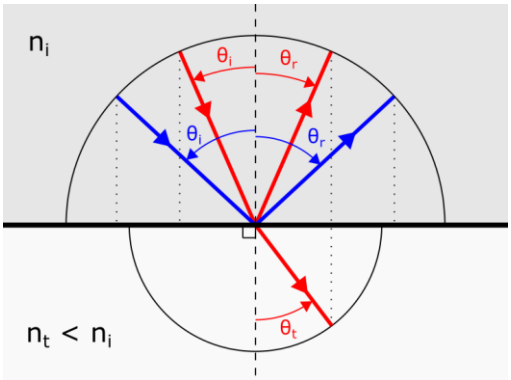

Figure 2.1. Snell's law

The continuity of the tangential components of the wave vectors of incident, reflected and transmitted waves lead to these three wave vectors being on a single plane of incidence (the plane of Figure 2.1), their angles being given by Snell's law:

$$n_1 \sin\theta_i = n_1 \sin\theta_r = n_2 \sin\theta_t \tag{2.1}$$

The amplitude of the wave vector $k_j = 2\pi n_j/\lambda_0$ is greater in a optically denser material with higher refractive index, as a consequence when light is incident from a medium with higher refractive index at an angle higher than the critical angle $\theta_c = \sin^{-1}(n_t/n_i)$, total internal reflection occurs.

The continuity of tangential electric fields lead to the Fresnel equations describing the amplitudes of the refracted and transmitted electric fields as functions of incidence angle, polarization, and the refractive indices of the materials bound by the flat surface. Fresnel coefficients corresponding to reflected and transmitted power are:

$$f_{R,s} = \left|\frac{n_1 \cos\theta_1 - n_2 \cos\theta_2}{n_1 \cos\theta_1 + n_2 \cos\theta_2}\right|^2 \tag{2.2}$$

$$f_{R,p} = \left|\frac{n_2 \cos\theta_1 - n_1 \cos\theta_2}{n_2 \cos\theta_1 + n_1 \cos\theta_2}\right|^2$$

$$f_{T,s} = 1 - f_{R,s}$$

$$f_{T,p} = 1 - f_{R,p}$$

2.2.1 Multiple incoherent reflection coefficients

Consider a light beam incident on a flat slab of material with constant thickness and refractive index n_2, sandwiched by materials with refractive indices n_1 and n_3, as illustrated by Figure 2.2.

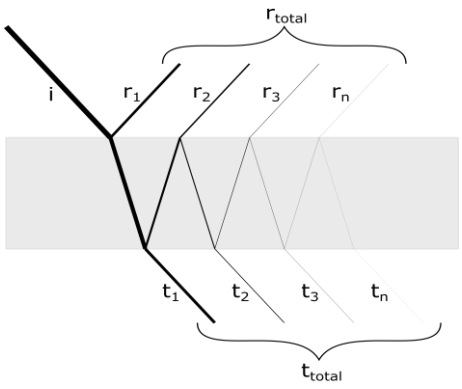

Figure 2.2. Multiple beams reflected from and transmitted through a non-absorbing dielectric slab.

Interference effects would occur between light waves reflected off the front surface and transmitted through the front surface after being reflected from the rear surface, provided that the coherence length of the incident light is greater that the optical path difference of interfering beams. In this case, the amount of light reflected additionally depends on the thickness of the slab and the wavelength. However, if the slab is thick enough, or if the light can be considered incoherent (e.g. due to one side of the slab being textured), the total of reflected power due to these multiple reflections is given by:

$$f_{R\ total,j} = \frac{f_{R1,j} + f_{R2,j} - 2f_{R1,j}f_{R2,j}}{1 - f_{R1,j}f_{R2,j}} \tag{2.3}$$

Here j refers to either s or p polarization.

2.3 Diffraction phenomena in periodic ordered structures

When the dielectric surface consists of a periodic grating structure with a given spatial frequency along one direction, as illustrated in Figure 2.3, constructive interference occurs between light reflected off troughs and crests of the structure, leading to diffraction of light into different orders travelling at different angles.

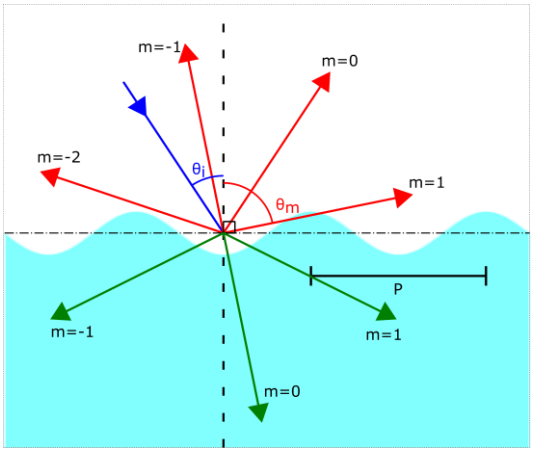

Figure 2.3. Sinusoidal 1D grating.

The distribution of diffracted power into propagating diffraction orders is complicated, and depends on the grating amplitude (i.e. the separation between troughs and crests), polarization of light and the exact shape of the periodic element; but diffraction angles of different orders depend only on the grating equation.

If the direction of grating periodicity is aligned with the plane of incidence, diffracted orders are all in the plane of incidence, and the grating equation is simply:

$$n_i \sin\theta_i + m\frac{\lambda_0}{P} = n_d \sin\theta_{d,m} \tag{2.4}$$

Here, n_i is the refractive index of the medium of incidence, the integer m is the diffraction order, P is the grating period and n_d and $\theta_{d,m}$ are the refractive index and diffraction angle of order m of the medium of diffraction, which can be either reflection or transmission. Therefore, a periodic grating imparts an integer multiple of its grating wave vector λ_0/P into the tangential component of the incident wave vector, along the direction of periodicity. However, note that for a diffraction order $\theta_{d,m}$ to propagate (i.e. be non-evanescent), the condition $|sin\,\theta_{d,m}| < 1$ needs to be satisfied.

2.4 Randomly textured surfaces and their statistical quantities

If the surface is not optically flat but randomly textured, with a random height distribution profile $z = h(x, y)$, the incident light is scattered into all directions, both in reflection and in transmission. For most real randomly textured surfaces, the scattered light is composed of a direct, non-diffracted or specular (i.e. mirror-like) component whose direction is given by Snell's law, and a diffuse part. The angular distribution of scattered power is not trivial, and is the main focus of Chapter 4. However, a lead on this problem can be obtained by considering a 2D random surface texture as a superposition of an infinite number of sinusoidal gratings with different amplitudes and spatial frequencies, in both directions.

This decomposition is usually done by the surface power spectral density function (PSDF), which is the squared modulus of the Fourier transform of the height profile, and gives the amplitude spatial frequency distribution of mean-square surface roughness σ^2 of the height profile:

$$PSDF_{2D}(f_x, f_y) = \lim_{L\to\infty} \frac{1}{L^2} \left| \iint_{-\infty}^{+\infty} h(x,y)\, e^{-i2\pi(f_x x + f_y y)} dxdy \right|^2 \tag{2.5}$$

Here, L is the surface size, f_x and f_y are the spatial frequencies along x and y directions. Hence:

$$\sigma^2 = \frac{1}{L^2}\iint_{-\infty}^{+\infty}\left(h(x,y) - \overline{h(x,y)}\right)^2 dxdy = \iint_{-\infty}^{+\infty} PSDF_{2D}(f_x, f_y)\, df_x df_y \qquad (2.6)$$

Here, $\overline{h(x,y)}$ is the mean value of the surface height profile.

Root-mean-square roughness σ is an indicator of the vertical variations in the height profile, but does not contain any information about the scale of lateral variations. This lateral scale can be obtained from the 2D surface autocorrelation (or autocovariance) function (ACF_{2D}), which is the inverse Fourier transform of the $PSDF_{2D}$, and the geometric average of the surface height profile with a translated version of itself.

$$ACF_{2D}(\tau_x, \tau_y) = \lim_{L\to\infty} \frac{1}{L^2}\iint_{-\infty}^{+\infty} h(x,y)\, h(x-\tau_x, y-\tau_y)\, dxdy \qquad (2.7)$$

When the translation (τ_x, τ_y) is zero, the value at origin of ACF_{2D} is at its maximum at σ^2. The distance at which the ACF_{2D} value falls to $1/e$ of its peak can be defined as the autocorrelation length (acl), and is an indicator of the characteristic lateral distance between features on the surface. However, unlike the definition of σ, the value of the acl depends on the actual form of the ACF function. If the acl is obtained by fitting an analytical expression (e.g. Gaussian, exponential, etc.) on the actual ACF data, as in Chapter 3.1, the choice of the fitting function can change the precise physical meaning of the resulting the acl.

The relations between the surface height profile, PSDF, ACF, surface roughness σ and the autocorrelation length are illustrated in Figure 2.4.

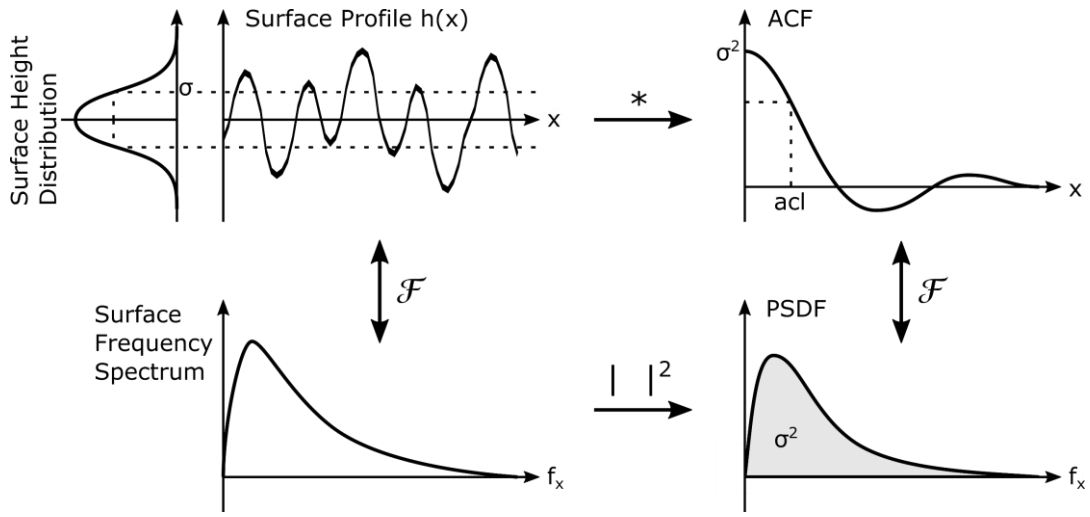

Figure 2.4. Height profile, PSDF, ACF, σ, acl, and their Fourier transform relations. Adapted from [52,60].

A surface texture which is truly random in all directions is isotropic, its PSD_{2D} and ACF_{2D} functions have circular symmetry, and acl is the same in all directions. This might not exactly be the case for all practical randomly textured samples, e.g. due to machining artefacts in some directions, or if an otherwise random texture is deposited on top of an anisotropic, grating-like quasi-periodic structure. Variation of surface statistics along different surface directions are usually linked to variations in surface scattering along corresponding azimuthal directions.

2.5 Definitions of radiometric quantities

As the incident light is scattered from a randomly textured surface into all directions, as illustrated by Figure 2.5, it can be characterized by a detector surface some distance away. Here, relevant radiometric quantities pertaining to the exchange of radiation between these surfaces will be defined.

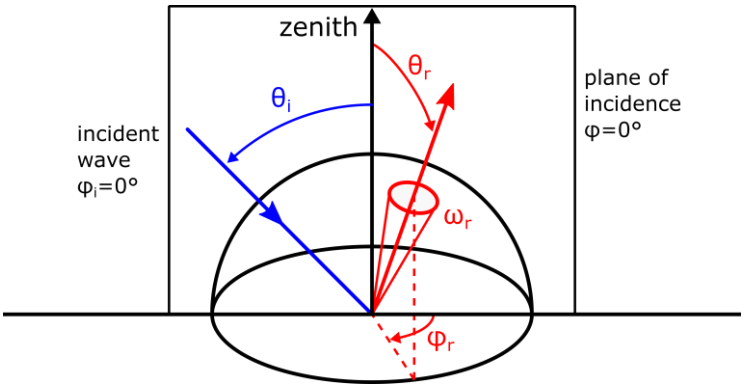

Figure 2.5. Scattering geometry, in spherical coordinates, drawn here for the reflection hemisphere.

A detector measures the radiant power P_c falling onto its surface collector area, which is an extensive quantity that depends on the size of the detector. A corresponding intensive quantity is radiant flux per unit collector area, or irradiance $E_c = \partial P / \partial A_c$, where A_c is the collector area. Note that outside of radiometry terminology, the term intensity is still often used to describe this quantity, but in the following the radiometric convention outlined e.g. by Harvey et al. [55] will be followed. However, the irradiance still depends on the collector distance to the source, because its subtended solid angle changes with distance.

2.5.1 Intensity

Therefore, the proper quantity to characterize and compare light scatter measurements is the radiant power per unit collector solid angle, or radiant intensity $I_c = \partial P / \partial \omega_c$, where ω_c is the solid angle subtended by the collector area from the source, (especially for source areas that are small compared to the square of the separation between the two surfaces). The angular intensity distribution (AID) can be mapped across the entire scattering hemisphere (either in reflection or transmission) in a $I_{2D}(\theta, \varphi)$ plot; or along any cross section of the hemisphere going through the zenith direction in a $I_{1D,\varphi}(\theta)$ plot, as illustrated in Figure 2.6a. A

numerical algorithm for high resolution $I_{1D}(\theta)$ calculation along the plane of incidence, for isotropic textures, from a discrete $I_{2D}(\theta, \varphi)$, map will be presented in Chapter 4.

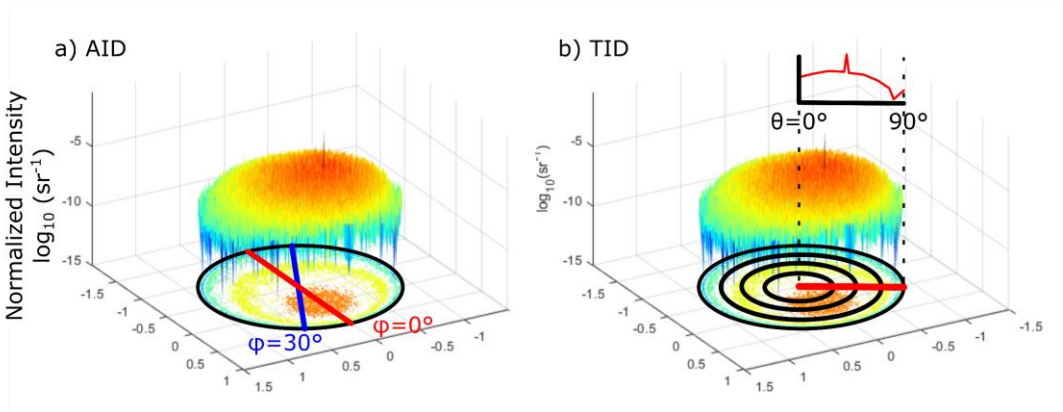

Figure 2.6. a) AID, b) TID

Another method to present radiant intensity is to average it along the azimuthal φ coordinate, i.e. along ring elements with the same θ_s angles from the surface normal. This representation, illustrated in Figure 2.6b, has been called total intensity distribution (TID) [43], and gives the total intensity scattered across the entire hemisphere at a radial angle θ_s. It is useful in situations where directions with the same θ are treated equally, (e.g. corresponding to equivalent modes travelling at different directions within a slab of material). Therefore, it is the relevant quantity for quantitative calculations of absorption and current enhancement. For isotropic samples and under normal incidence, the integration along the φ coordinate is analytically equivalent to $TID(\theta) = I_{1D}(\theta) \times |sin\,\theta|$, but this formula is of limited use for quantitative calculations in real situations where the non-diffracted component carries a significant part of the radiant power, or under oblique incidence. An algorithm for TID calculation from a discrete I_{2D} map will be presented in Chapter 5.

2.5.2 Radiance

An even more fundamental quantity is radiant power per unit collector solid angle per unit projected source area, or radiance $L = \partial^2 P/(\partial\omega_c \partial A_s \cos\theta_s)$, where A_s is the source area, and θ_s is the inclination angle of the source with respect to the collector direction. Radiance is more relevant in situations where the source area is appreciable with respect to the square of the separation between the two surfaces.

An important concept describing an ideal diffuser surface is the Lambertian surface, which has a constant radiance distribution across all directions, regardless of the incidence direction. The value of this constant radiance can be calculated considering a hemispherical collector centered around/on the scattering surface. If the total scattered radiant power in reflection or transmission is $P_{R,T}$:

$$P_{R,T} = \int_{\substack{hemi \\ sphere}} \int_{A_s} L\ cos\,\theta_s\ \partial A_s\ \partial\ \omega_c = L\ A_s \int_0^{\pi/2} \int_0^{2\pi} cos\,\theta_s\ sin\,\theta_s d\theta d\varphi \tag{2.8}$$

$$= 2\pi\ L\ A_s \int_0^{\pi/2} cos\,\theta_s\ sin\,\theta_s\ d\theta = \pi\ L\ A_s$$

$$L_{Lambertian} = \frac{P_{R,T}}{\pi\ A_s} \tag{2.9}$$

CHAPTER 3

EXPERIMENTAL WORK

"Make measurable what cannot be measured."
Galileo Galilei

3.1 Surface topography characterization by atomic force microscopy

Atomic force microscopy (AFM) is a high-resolution surface characterization technique suitable to map the topography of nanotextured surfaces with roughnesses smaller than a several μm. It uses a fine tip, with a tip radius around 10 nm, mounted on a caltilever to move over the surface using piezoelectric elements. In tapping mode, which is preferred for topography measurements, the cantilever is oscillated at a fixed frequency, which changes due to the distance of the tip from the surface through Van-der-Waals interactions. The height information is gathered at regular intervals over the surface, using a feedback loop to keep the oscillation frequency (and hence the distance) constant. There can be other types of interactions between the surface and the tip that compounds the height information, such as on heterogeneous surfaces or where electrostatic or magnetic forces are present; but these are negligible in the case of hard, dielectric surfaces.

A consequence of this discrete sampling is to introduce a high frequency band limit to the height profile and corresponding surface roughness. Therefore, the roughness σ measured from an AFM scan (or any other characterization method) is a bandwidth limited version of the intrinsic surface roughness defined in Equation (2.6) [8,50]. However, for the surfaces and optical wavelengths used in this work, the contribution

of these high spatial frequencies is very small and in any case not relevant for the optical diffraction interaction, which is further explained in section 4.4.1.

If the sample surface is not perfectly aligned with the plane of the cantilever scan, their difference would result in an oblique plane superimposed to the height profile. This is corrected by a single plane subtraction. Polynomial subtractions of higher order are not recommended in this case because they can erode into the low frequency spatial components of the surface, which can lead to artificial dips in later AID distributions near the central frequency.

3.2 Surface preparation

Two different types of samples, covering a wide range of surface roughnesses (σ) and lateral autocorrelation lengths (acl) were used throughout this dissertation. Their relevant surface parameters, indicated in Figure 3.1 and Table 3.1, were extracted from 25x25 μm^2 square AFM images with 256 data points per line, using Gwyddion software [61] after a single plane subtraction for tilt correction followed by zero mean level adjustment. Slope distributions were obtained using local plane fitting around each data point.

Table 3.1 Surface roughness σ and autocorrelation length acl extracted from AFM topography images. Asterisks indicate values taken from the optically relevant part of two-Gaussian fit of radial autocorrelation function.

	A	*B*	*C*	*D*	*E*
σ (nm)	20.5*	67.0*	70.0*	82.7	129.4
acl (nm)	889*	1166*	768*	321	527

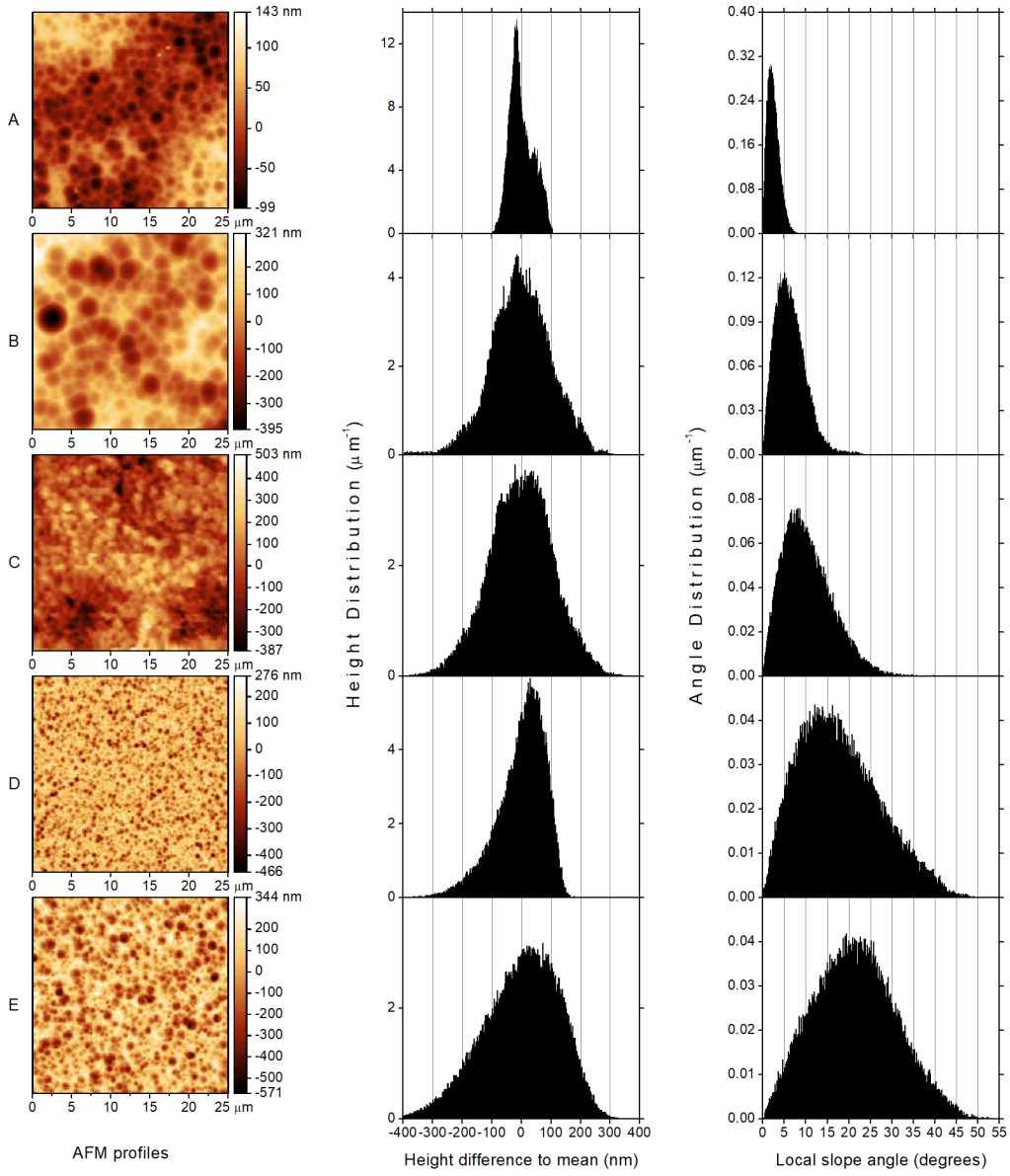

Figure 3.1. AFM images, height and slope angle distributions

Samples A, B and C were prepared using the aluminium induced texturing (AIT) method [62], where a 150 nm thick layer of aluminium is deposited on 3 mm thick soda-lime glass substrates (refractive index n≈1.52) and annealed at 600°C for 60 minutes to produce a textured Al_2O_3 layer with crystalline Si that precipitates with a low nucleation centre density [63] at the interface. These intermediates are then etched away using successive H_3PO_4 and HF:HNO_3 solutions (samples A and B)

[62] or a NaOH:H_2O_2:H_2O solution (sample C) [64], for different etch durations. As can be seen in Figure 3.1, the presence of intermediate Si precipitates creates a coarser length scale with deep valleys and crests, superimposed on an optically relevant smaller length scale. This small texture manifests itself as a micrometer-sized, cusp-like texture for sample A, and a finer, pyramid-like texture for sample B, ranging from smooth ($\sigma/\lambda \approx 0.05$ for sample A for λ=532nm) to moderately rough surfaces. The resulting surface height distribution is usually not Gaussian. The azimuthally-averaged radial ACF is best modelled using a two-Gaussian fit [$f(x) = \sigma_1^2 . e^{-(x/acl_1)^2} + \sigma_2^2 . e^{-(x/acl_2)^2}$], corresponding to the two length scales. For these samples, the optically relevant smaller acl and corresponding σ values are indicated with an asterisk. As will be seen in Chapter 4.2.5, these irregularities make the AID of these samples more challenging to model, but also enables to test the applicability and robustness of the different modelling approaches.

The other type of samples, represented by samples D and E, were prepared by depositing 1.25 μm thick Al:ZnO by sputtering, on 2 mm thick and nominally flat Schott glass substrates, followed by a one-step wet HCl etching [65], for 30s at different concentrations. Ellipsometry analysis indicate a refractive index of n=1.87. The rough textures produced by this method present a highly uniform distribution of "etch pits", resulting in a height distribution with a negative skew. The radial ACF is ideally modelled using a single Gaussian fit [$f(x) = \sigma^2 . e^{-(x/acl)^2}$], leading to smaller autocorrelation lengths. These textures exhibit roughnesses towards the higher end of relevance for solar cells, and without further treatment they might not be ideal to preserve the electrical performance of subsequent active layers [27]. However, once again, they are ideal to test the applicability limits of SST.

3.3 Goniometer: instrumentation and AID measurements

In order to compare with and validate the different implementations of the Harvey-Shack theory, AID of light scattering from these samples along the plane of incidence

were measured using a purpose designed, home-made automated goniometer system. This instrument, illustrated in Figure 3.2a, consists of two concentric rotation stages.

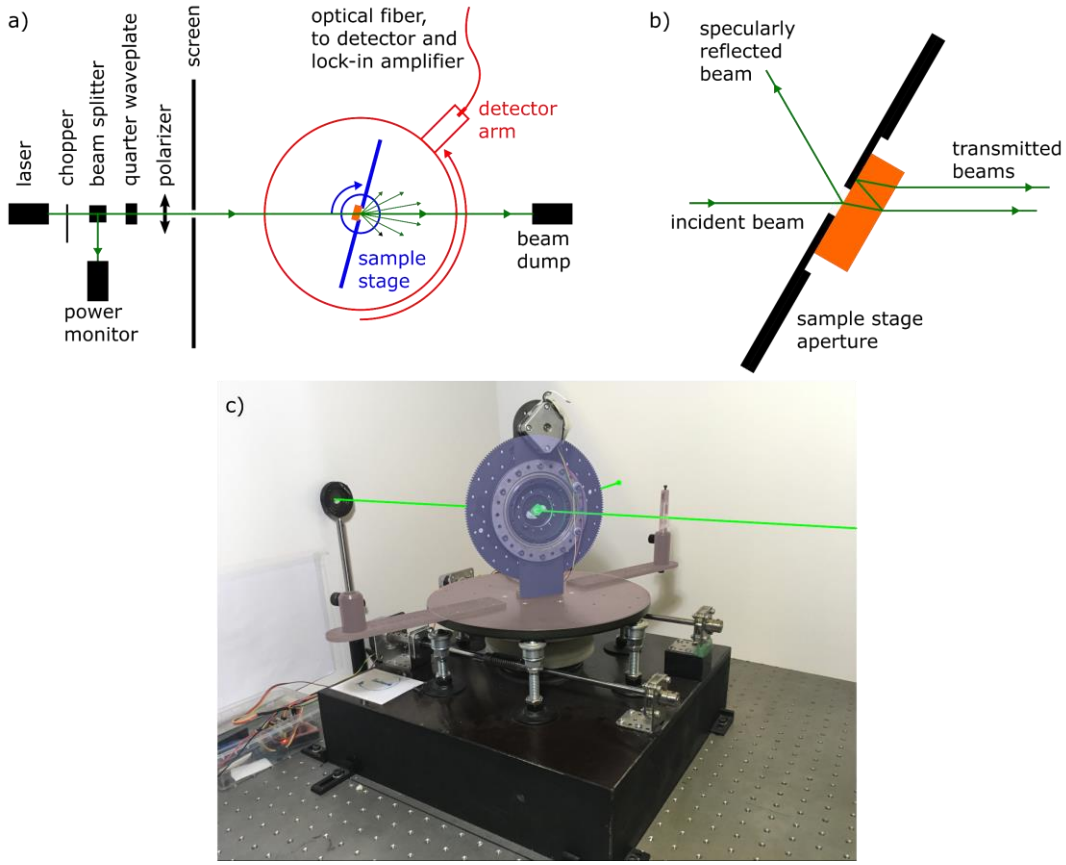

Figure 3.2. a) General schematic of instrumentation, shown for AID in transmission measurement. b) Aperture width and sample thickness minimizing multiple reflection effects, shown for AID in reflection measurement. c) Photograph of the goniometric instrument.

The first one in the center supports a screen, with a 3 mm (or 6 mm) diameter aperture that holds the sample, and controls the angle of incidence. A laser beam of fixed path, with 532 nm wavelength and a 1.45 mm Gaussian beam width traverses the center of this aperture, after being modulated by an optical chopper. The polarization of the incident beam with respect to the plane of incidence is set by a quarter-waveplate and a polarizer pair. In this dissertation, only s-polarized incident light is used. This is because, when vector RS diffraction integral is considered [66] in a

more general vector Fourier optics approach, the scalar approach is shown to match the complex amplitude of waves scattered in the plane of incidence only for s-polarized incident waves. p-polarized incident waves result in more complicated phenomenon such as dips in reflected scatter corresponding to quasi-Brewster angles in the AID measurements.

The second stage controls a detector arm that rotates around the center independently of the first stage, and scans for scatter signal in either reflection or transmission. On the detector arm, scattered light is coupled to a 1 mm core diameter optical fiber through a 3 mm diameter diffuser film at a distance of 244 mm from the center aperture; this corresponds to a light-collecting opening of about $\Delta\Omega s=1.2x10^{-4}$ steradians, or 0.7° around the plane of rotation. This small collector footprint ensures very little blocking of incident light around the incidence direction in reflection measurements, (< 2° wide), while being adequate to measure laser beam power when it is directly incident on the collector. The calibration of this measurement to account for coupling losses between the diffuser disk and the fiber core is the subject of Appendix A.1.

The other side of the fiber is coupled to a variable gain silicon photodetector, whose signal is measured using a lock-in amplifier. The center aperture diameter, in conjunction with laser beam width and sample thicknesses, is selected to be able to reject the effect of multiple reflections inside the glass substrates for 30° and 60° incidence measurements, as illustrated in Figure 3.2b. In cases where multiple reflections and transmissions cannot be avoided, e.g. from the thin Al:ZnO layer or from glass samples under normal incidence, multiple incoherent reflection coefficients from Equation (2.3) are used. A set of screens is employed for stray light reduction.

The scatter signal is then normalized by the incident beam signal (laser beam measured directly by the same collector without sample) and by the subtended solid angle, to obtain the normalized AID in the plane of incidence, expressed in sr^{-1}. In

transmission measurements, the reflection loss at the first flat surface is accounted for, by dividing the signal by the corresponding Fresnel coefficient.

The instrument exhibits a dynamic range of up to 7 orders of magnitude. In most measurements, the noise equivalent normalized intensity level occurs around 10^{-4} steradian^{-1}, although this depends the level attenuation of the laser power by a set of neutral density filters to reduce the power below the damage threshold of polarizers.

The data correction due to the lock-in amplifier time constant not being fast enough to follow the rapidly varying signal at the peak position (and the next data point) is covered in Appendix A.2.

CHAPTER 4

ON HARVEY-SHACK SCALAR SCATTERING THEORY

"If you have two adjustable parameters in your model, you can make it draw an elephant, if you have three adjustable parameters you can make it jump, with four you can make it talk" - Prof. Bill Nicoll

4.1 Introduction

Historically, the two main approximative approaches to the problem of surface scattering based on some approximation of Maxwell's equations consisted of the Rayleigh-Rice small-amplitude vector perturbation theory [67-71], which remains valid for large scatter angles and incorporates polarization effects, but is limited to smooth surfaces ($\sigma/\lambda<<1$), and the Beckman-Kirchhoff SST [72], which remains valid for rough surfaces but contains a paraxial approximation that limits its use to small incidence and scatter angles.

Developments in small amplitude perturbation theory using the reduced Rayleigh equation (RRE) method [73-78] have been applied to the study of higher order coherent localization and multiple scattering effects, albeit for sufficiently small slopes and at the cost of computational complexity.

Derivatives of the former approach, including the work of Carniglia [79], together with earlier work by Bennett et. Al. [80], have been used for total integrated scatter or haze calculations [28], (i.e. the ratio of diffuse reflected or transmitted scatter to total reflectance or transmittance), where the paraxial limitation is not important. However, for many applications including solar cells, haze calculation alone is not

always enough to give an accurate characterization of the scattering ability of a surface [30,31].

Rigorous methods that solve for Maxwell's equations have been used to model light scattering at randomly textured interfaces. These include methods such as RCWA [36] that divides the volume into homogeneous layers, the finite-difference time-domain (FDTD) [33-35] or finite element method (FEM) [37] that discretize the entire volume, and surface integral methods such as the method of moments (MoM) [81] or the non-perturbative implementation of the reduced Rayleigh equation (RRE) method [82-85].

While these rigorous numerical methods are important for validating applicability ranges of more approximate theories, they do not lend themselves well to parametrization for random textures, and they can become computationally intensive for statistically relevant large surfaces.

In this context, a particularly interesting method stems from the work of Harvey et al., who over the years developed a nonparaxial SST based on a Fourier optics linear-systems approach [52-59], suitable for both rough surfaces and large scatter angles. This Harvey-Shack SST has been used to model surface scatter in a wide range of applications [9-11,13], including solar cell research [42-51] for over a decade.

In this chapter, the Harvey-Shack SST will be derived. This computationally efficient method uses Fourier transforms on the optical phase light accumulates while traversing the rough texture to evaluate a modified Rayleigh-Sommerfeld (RS) diffraction integral [86,87]. Different versions of this method will be implemented and compared to actual far-field angular intensity measurements. These comparisons show a remarkable quantitative fit, but also reveal several interesting features and limitations of SST that will be discussed in detail. The first one concerns rough textures with lateral feature sizes on the order of the wavelength, which can be linked to effective medium effects. The second one is explained by a redistribution of part of scattered power, which has been experimentally linked to secondary interactions within the surface topography

4.2 Review of Harvey-Shack scalar scattering theory

The Harvey approach is based on the Fourier optics, linear systems treatment of the problem of scalar diffraction of a time-independent, monochromatic wave passing through a binary aperture [88]. The diffraction aperture creates a binary disturbance $U_0(\hat{x}, \hat{y}, \hat{z} = 0)$ in the complex amplitude distribution of the incident plane wave.

The complex amplitude diffracted into the forward half-space is expressed by the convolution of this initial disturbance with the impulse response of free space, which results in the RS diffraction integral [52,54], here expressed for an observation plane at a distance z from the aperture:

$$U(x, y; z) = \lambda_0 \iint_{-\infty}^{+\infty} U_0(x', y'; 0) \left(\frac{\lambda_0}{2\pi l} - i \right) \frac{z}{l} \frac{e^{i2\pi l/\lambda_0}}{l} dx' dy' \tag{4.1}$$

In this expression, x' and y' are the integration variables mapping the aperture, and $l = \sqrt{(x - x')^2 + (y - y')^2 + z^2}$ is the distance from points in the aperture and the observation point.

4.2.1 Diffraction from an empty aperture observed on a hemisphere

When spatial coordinates are normalized with respect to the vacuum wavelength λ_0, i.e.:

$$\hat{x} = x/\lambda_0, \quad \hat{y} = y/\lambda_0, \quad \hat{z} = z/\lambda_0, \quad \text{and} \quad \hat{r}^2 = \hat{x}^2 + \hat{y}^2 + \hat{z}^2,$$

the Fourier transform of the initial disturbance $U_0(\hat{x}, \hat{y})$ leads to the angular spectrum formulation, where the corresponding reciprocal coordinates $\alpha = \hat{x}/\hat{r}$ and $\beta = \hat{y}/\hat{r}$ become the direction cosines of the propagation vectors of diffracted plane wave components emerging from the aperture [88], with $\gamma = \hat{z}/\hat{r} = \sqrt{1 - (\alpha^2 + \beta^2)}$. This geometric configuration is illustrated in Figure 4.1.

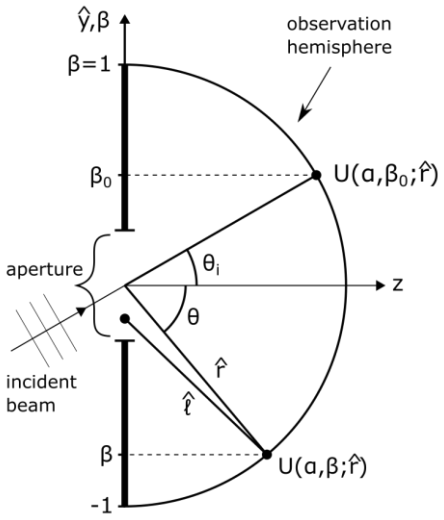

Figure 4.1. Geometric configuration of the incident plane wave, diffracting aperture and the observation hemisphere. Adapted from [52,55].

These direction-cosine coordinates are also related to spherical coordinates centered around the aperture by:

$$\alpha = \sin\theta\cos\varphi \qquad \beta = \sin\theta\sin\varphi \qquad \gamma = \cos\theta \qquad \alpha/\beta = \tan\varphi$$

This choice of coordinates also enables the RS diffraction integral of Equation (4.1) to be evaluated over an observation hemisphere centered around the aperture [52,54]:

$$U(\alpha,\beta;\,\hat{r}) = \gamma\frac{e^{i2\pi\hat{r}}}{\hat{r}}\iint_{-\infty}^{+\infty} U_0(\hat{x}',\hat{y}';0)\left(\frac{1}{2\pi\hat{l}} - i\right)\frac{\hat{r}^2}{\hat{l}^2}e^{i2\pi(\hat{l}-\hat{r})}\,d\hat{x}'d\hat{y}' \qquad (4.2)$$

It is important to distinguish between waves with reciprocal space coordinates that lie inside a unit circle in direction-cosines space, satisfying $\alpha^2+\beta^2 \le 1$, which correspond to propagating waves; and those with $\alpha^2+\beta^2 > 1$, which correspond to evanescent waves that do not radiate power.

This general expression is accurate in all the forward half-space, (so far as it is a scalar expression), for any aperture or observation hemisphere size, right down to the aperture. By setting $\left(\hat{l}-\hat{r}\right) = \widehat{W}(\hat{x},\hat{y};\hat{r}) - (\alpha\hat{x}'+\beta\hat{y}')$, the RS diffraction

integral can be expressed directly as a Fourier transform integral, where all the phase terms except those used in the Fourier kernel are grouped in the $\widehat{W}$ term.

$$U(\alpha,\beta;\,\hat{r}) = \gamma\frac{e^{i2\pi\hat{r}}}{\hat{r}}\iint_{-\infty}^{+\infty} U_0(\hat{x}',\hat{y}';0)\left(\frac{1}{2\pi\hat{l}} - i\right)\frac{\hat{r}^2}{\hat{l}^2}e^{i2\pi\widehat{W}}e^{-i2\pi(\alpha\hat{x}'+\beta\hat{y}')}\,d\hat{x}'d\hat{y}' \tag{4.3}$$

Furthermore, when this observation hemisphere is significantly larger than both the wavelength ($\hat{l} \gg 1$), and the aperture size, i.e. $\hat{l} - \hat{r} \approx -(\alpha\hat{x}' + \beta\hat{y}')$, as is the case in our far-field angular measurements, the only remaining phase variations are those originating at the aperture plane, i.e. $U_0(\hat{x}',\hat{y}';0)$. The effect of these neglected terms is the subject of Chapter 5. The diffraction integral can then be simplified to a single Fourier transform as:

$$\begin{aligned} U(\alpha,\beta;\,\hat{r}) &= \gamma\frac{e^{i2\pi\hat{r}}}{i\hat{r}}\iint_{-\infty}^{+\infty} U_0(\hat{x}',\hat{y}';0)\,e^{-i2\pi(\alpha\hat{x}'+\beta\hat{y}')}\,d\hat{x}'d\hat{y}' \\ &\equiv \gamma\frac{e^{i2\pi\hat{r}}}{i\hat{r}}\mathcal{F}\{U_0(\hat{x},\hat{y};0)\} \end{aligned} \tag{4.4}$$

When the incident light illuminates the aperture at an oblique angle of incidence θ_0, a linear phase variation appears along the aperture. According to the shift theorem of Fourier transform theory, the resulting complex amplitude is simply linearly shifted in direction-cosines space. For an isotropic initial disturbance, the incidence can be chosen along one of the coordinate axes without loss of generality.

In this work, only surfaces that have isotropic textures are considered, i.e. azimuthal directions are equivalent. Hence, for simplicity and without loss of generality, the incidence can be chosen along one of the coordinate axes. For anisotropic textures such as crossed gratings or pyramid textures however, it is straightforward to use a two-component shifting vector. For an angle of incidence along the $\hat{y}$ axis, the complex amplitude becomes:

$$U(\alpha, \beta - \beta_0;\, \hat{r}) = \gamma \frac{e^{i2\pi\hat{r}}}{i\hat{r}} \mathcal{F}\{U_0(\hat{x}', \hat{y}'; 0)\, e^{i2\pi\beta_0\hat{y}}\} \tag{4.5}$$

Note that with an oblique incidence, the irradiance is also attenuated by an obliquity factor of $\gamma_0 = \cos\theta_0$. However, for an accurate comparison with the results of our angular measurements, where the entire laser beam width traverses the aperture regardless of the angle of incidence, this factor should be dropped.

4.2.2 Radiant angular power distribution

In scalar wave optics, irradiance is equal to the squared modulus of the (time independent) complex field amplitude [88]. Notably, on the observation hemisphere surface, the collector area elements make an angle θ with respect to the coordinate axis, as illustrated in Figure 4.2. The irradiance expressed in direction-cosine space is simply:

$$E_{c,2D}(\alpha, \beta - \beta_0) = \frac{|U(\alpha, \beta - \beta_0;\, \hat{r})|^2}{\gamma} \tag{4.6}$$

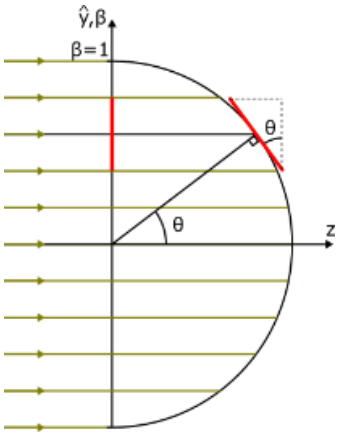

Figure 4.2. Irradiance inside hemispheric collector area elements expressed in direction cosine space.

Moreover, the solid angle subtended by a collector area $d\hat{A}_c = \hat{r}^2 \sin\theta \, d\theta d\varphi$ on the observation hemisphere and viewed from the aperture center is simply $d\omega_c = dA_c/r^2$. Hence, the intensity distribution is:

$$I_{c,2D}(\alpha, \beta - \beta_0) = \hat{r}^2 E(\alpha, \beta - \beta_0) \tag{4.7}$$

The radiant power P_j scattered across any portion j of the observation hemisphere can be found by integrating the irradiance (or the intensity) across its collector area $\hat{A}_{c,i}$ (or its corresponding solid angle $\omega_{c,i}$). Using the change of variables between coordinate systems $d\alpha d\beta = \sin\theta \cos\theta \, d\theta d\varphi$, and the collector area $d\hat{A}_c = \hat{r}^2 \sin\theta \, d\theta d\varphi$, and substituting Equation (4.6):

$$P_j = \iint\limits_{\hat{A}_{c,\mathrm{j}}} E_c(\theta, \theta_0, \varphi) d\hat{A}_c \tag{4.8}$$

$$= \iint\limits_{\omega_{c,\mathrm{j}}} E_c(\theta, \theta_0, \varphi) \; \hat{r}^2 \sin(\theta) \, d\theta d\varphi$$

$$= \iint\limits_{\omega'_{c,\mathrm{j}}} E_c(\alpha, \beta - \beta_0) \, \hat{r}^2 \, \frac{d\alpha d\beta}{\gamma} = \iint\limits_{\omega_{c,\mathrm{j}}} I_c(\theta, \theta_0, \varphi) \, \frac{d\alpha d\beta}{\gamma}$$

$$= \iint_{\omega'_{c,\mathrm{j}}} \frac{\hat{r}^2}{\gamma^2} \, |U(\alpha, \beta - \beta_0; \, \hat{r})|^2 \, d\alpha d\beta$$

$$= \iint_{\omega'_{c,\mathrm{j}}} \left| \mathcal{F}\{U_0(\hat{x}', \hat{y}'; 0)\} \, e^{i2\pi\beta_0 \hat{y}} \right|^2 d\alpha d\beta$$

$$= \iint_{\omega'_{c,\mathrm{j}}} \phi(\alpha, \beta - \beta_0) \, d\alpha d\beta$$

Among diffracted power quantities, the quantity that is shift-invariant with respect to the angle of incidence is scattered radiance, i.e. the radiant power received per unit solid angle and emitted per unit projected source area [55]. Radiance proper is used to characterize an emitter with an appreciable source area compared to the square of

the viewing distance; whereas in our far-field treatment and angular measurements, the source area is negligible.

Therefore, I prefer to use a more direct quantity with the same functional form, i.e. scattered power per direction cosine-space unit area, $\phi(\alpha, \beta - \beta_0)$. As seen in (4.8), this quantity is shift-invariant, provided that the expression of $U_0(\hat{x}', \hat{y}'; 0)$ is also independent of incident and scatter angles.

$$\phi(\alpha, \beta - \beta_0) = \frac{\hat{r}^2}{\gamma^2} |U(\alpha, \beta - \beta_0; \hat{r})|^2 = \left|\mathcal{F}\left\{U_0(\hat{x}', \hat{y}'; 0)\, e^{i2\pi\beta_0\hat{y}}\right\}\right|^2 \tag{4.9}$$

Hence, the squared modulus of a single Fourier transform of the pupil function $U_0(\hat{x}', \hat{y}'; 0)$ directly maps the (far-field) power distribution in direction-cosine space.

Recall that in (4.9), only the part of the angular distribution that falls inside the unit circle described by $\alpha^2 + \beta^2 \leq 1$ in direction-cosine plane is propagating. The "power" falling onto direction cosines outside the unit circle, $\alpha^2 + \beta^2 > 1$, corresponds to non-radiating, evanescent waves. Hence, Harvey proposes to add the following normalization constant to equations (4.7) and (4.9) to ensure the conservation of energy [55]:

$$K_{norm} = \tag{4.10}$$

$$\begin{cases} \dfrac{\iint_{-\infty}^{+\infty} \left|\mathcal{F}\left\{U_0(\hat{x}, \hat{y}; 0)\, e^{i2\pi\beta_0\hat{y}}\right\}\right|^2 \, d\alpha d\beta}{\int_{\alpha=-1}^{1} \int_{\beta=-(1-\alpha^2)^{1/2}}^{(1-\alpha^2)^{1/2}} |\mathcal{F}\{U_0(\hat{x}, \hat{y}; 0)\, e^{i2\pi\beta_0\hat{y}}\}|^2 \, d\alpha d\beta}, & \alpha^2 + \beta^2 \leq 1 \\ 0, & \alpha^2 + \beta^2 > 1 \end{cases}$$

This normalization constant is added to the distribution equations of all power quantities. Thus, the power and intensity distributions become:

$$\phi(\alpha, \beta - \beta_0) = K_{norm} \left|\mathcal{F}\left\{U_0(\hat{x}, \hat{y}; 0)\, e^{i2\pi\beta_0\hat{y}}\right\}\right|^2 \tag{4.11}$$

$$I_{2D}(\alpha, \beta - \beta_0) = K_{norm}\, \gamma \left|\mathcal{F}\left\{U_0(\hat{x}, \hat{y}; 0)\, e^{i2\pi\beta_0\hat{y}}\right\}\right|^2 \tag{4.12}$$

This normalization constant serves to redistribute the power contained in evanescent modes equally into radiant modes.

4.2.3 Harvey's original surface scatter theory

Up to this point, the approach deals with diffraction from an empty binary aperture in free space. It can be extended to the case of an aperture containing a textured interface, by considering the additional amplitude and phase changes induced upon the diffracted wave by this interface.

For a homogeneously illuminated surface with a homogeneous local reflectance and transmittance, the amplitude change is simply $\sqrt{p_i\, f_{R,T}}$, where p_i is the incident power; $f_{R,T}$ is the fraction of power reflected off or transmitted through the surface, given by the respective Fresnel coefficients for a flat surface. Phase changes depend on the optical path difference $\hat{o}(\hat{x},\hat{y};0)$ accumulated across the aperture due to the texture, compared to a flat interface. The pupil function $U_0(\hat{x},\hat{y};0)$ becomes:

$$U_{0;R,T}(\hat{x},\hat{y};0) = \sqrt{p_i\, f_{R,T}}\; e^{i2\pi\, \hat{o}(\hat{x},\hat{y};0)} \tag{4.13}$$

In the original version of Harvey-Shack (OHS) theory, the path that rays take through the textured zone is considered to be vertical to the plane of the interface, regardless of the angle of incidence, as illustrated in Figure 4.3. Initially, this was done for reflection to air, but it has been extended to include reflection and transmission between two arbitrary media. Hence the optical path difference becomes:

$$\hat{o}_{OHS}\,(\hat{x},\hat{y}) = (n_i \pm n_s)\,\hat{h}(\hat{x},\hat{y}) \tag{4.14}$$

where $\hat{h}(\hat{x},\hat{y})$ is the wavelength-normalized surface height profile, n_i and n_s are the refractive indices of the medium light is incident from and scattered to, respectively. The plus sign is used for scattering in reflection, where $n_i = n_s$ also; and the minus sign is used for scattering in transmission.

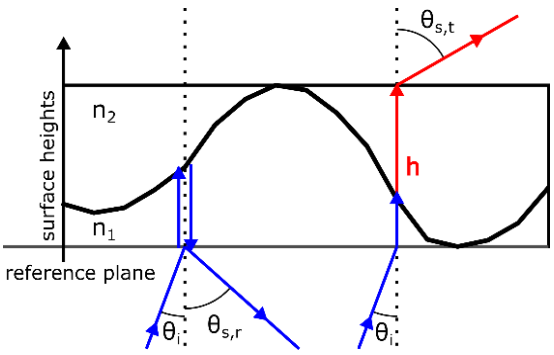

Figure 4.3. OHS interface optical path difference accumulation model.

The pupil function can thus be modelled as a phase screen:

$$U_{0,RT}\,(\hat{x},\hat{y};0) = \sqrt{p_i\, f_{R,T}}\; e^{i2\pi(n_i \pm n_s)\,\hat{h}(\hat{x},\hat{y};0)} \tag{4.15}$$

Substituting Equation (4.15) into Equation (4.11), the normalized power distribution in direction cosine space becomes:

$$\frac{\phi_{OHS}(\alpha,\beta-\beta_0)}{p_i} = K_{norm}\, f_{R,T}\, \left|\mathcal{F}\left\{e^{i2\pi(n_i \pm n_s)\,\hat{h}(\hat{x},\hat{y};0)}\; e^{i2\pi\beta_0\hat{y}}\right\}\right|^2 \tag{4.16}$$

4.2.4 Direct phase screen approach and its discrete implementation

The most straightforward way of modelling the phase screen to be Fourier-transformed is to simply use a surface height profile data obtained by AFM. This "Direct phase screen" (DPS) approach has been commonly used in the solar cell community in the past decade [42-48].

Here I will describe the discrete implementation, using a code running on a personal computer. A square AFM scan of side length L generates height data taken on NxN discrete points at regular intervals across the sample surface. It uses the discrete equivalent of Equation (4.15) for normal incidence, that uses a 2D Fast Fourier Transform (FFT) on the optical phase accumulated when light traverses the surface on these grid points:

$$\frac{P_{\alpha,\beta}}{p_i} = K_{norm}\, f_{R,T} \left| \frac{FFT_{2D}\left\{ e^{i2\pi(n_i \pm n_s)\hat{h}(N\times N)} \right\}}{N^2} \right|^2 \tag{4.17}$$

Since the modulus of each exponent element is 1, and there are N^2 of them, Parseval's theorem can be invoked to normalize the sum of the FFT distribution by dividing it by N^2.

The result of this 2D FFT operation, represented in Figure 4.4, is composed of matrix elements on NxN numerical "grid" points, and does not contain information on lateral coordinates. These lateral coordinates can be assigned by thinking of the AFM image area as a 2D cross diffraction grating with grove period L in both directions. For simplicity, consider the grating equation along one axis:

$$\frac{n_i}{n_s} sin\,\theta_i + m\frac{\lambda_0}{L\, n_s} = sin\,\theta_s \tag{4.18}$$

where θ_i and θ_s are the incident and diffracted order angles, and the integer m is the diffraction order.

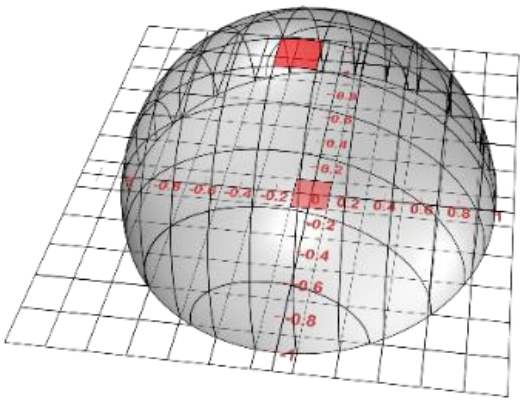

Figure 4.4. 2D FFT operation and associated direction cosine coordinates.

At normal incidence, the power of the non-diffracted beam corresponding to the order m=0 will be given by the central element ($\alpha = \beta = 0$), colored in Figure 4.4. This central element corresponds to the zenith direction of the hemisphere, and is at the center of the direction cosine coordinate system. The width of this central

element, as well as the distance between each consecutive order on any axis in direction-cosines space, is given by $\Delta\alpha = \Delta\beta = \lambda_0/(L\, n_s)$, and corresponds to the low spatial frequency limit of the AFM measurement. The power $P_{\alpha,\beta}$ contained in an element of discrete coordinates (α, β) can be thought of as distributed on an $\Delta\alpha \times \Delta\beta$ area centered around these coordinates. The high spatial frequency band limit of the AFM measurement, (determined by the distance between each scan point (i.e. L/N)) is not very crucial, as these frequencies usually correspond to evanescent waves. However, care should be taken to select a large enough grid size N, so that the diffraction hemisphere/circle does not brim over the image grid for oblique incidence angles and smaller wavelengths. Since only the matrix elements with a radial distance to this central element such as $\alpha^2 + \beta^2 \leq 1$ are propagating, the radius of the propagation hemisphere consists of $1/\Delta\alpha$ matrix elements. See Appendix B for the handling of elements that are partially outside the unit circle.

The normalization factor K_{norm} can be obtained by the inverse of the summation of all elements inside the unit circle:

$$K_{norm} = \frac{1}{\sum_{\alpha^2+\beta^2\leq 1}\left|\frac{FFT_{2D}\left\{e^{i2\pi(n_i \pm n_s)\hat{h}(N\times N)}\right\}}{N^2}\right|^2} \tag{4.19}$$

This normalization factor is usually very close to unity for most moderately rough and isotropic surface textures at normal incidence. Increasing the angle of incidence progressively shifts the power distribution out of the unit circle. Likewise, in highly rough surfaces, the power distribution becomes broader and thus extends more out of the unit circle.

The shifting effect due to oblique incidence can be incorporated in the 2D power distribution map by using the $e^{i2\pi\beta_0\hat{y}}$ term in the FFT, just as in the analytical expression, but doing this generally splits the power contained in the specular beam into two matrix elements, (unless the shift, $n_i/n_s\, sin(\theta_i)$ happens to be an exact multiple of $\Delta\alpha$). Moreover, using the $e^{i2\pi\beta_0\hat{y}}$ term generally creates more

discontinuity at the edges of the random phase screen image, which significantly amplifies spectral leakage problems, which are covered in Appendix C.

Instead, a better solution is to shift the coordinates of the observation hemisphere along one of the axes, and calculate radial distances from that shifted center. For isotropic surfaces where a circularly symmetric power distribution around the central element can be assumed, the azimuthal projection algorithm illustrated in Figure 4.5 can be used to calculate $I_{1D}(\theta)$ in the plane of oblique incidence.

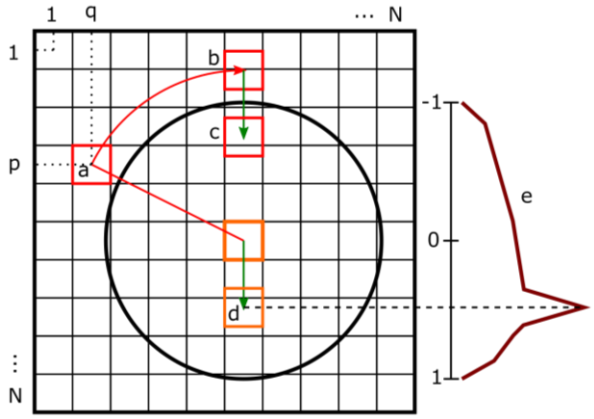

Figure 4.5. Azimuthal projection algorithm for isotropic samples. a) Position of an element with respect to the unshifted center in 2D space, b) Because of circular symmetry, only radial distance of elements needs to be considered, flattening the problem to 1D, c) applying the shift due to the angle of incidence, d) position of the specular beam, e) resulting AID, after division by the solid angles corresponding to each element with respect to the shifted center.

For each element, the radial distance in direction cosines space, $d_0 = \sqrt{\alpha^2 + \beta^2}$, to the unshifted central element is calculated. Each element is doubled to contribute one positive and one negative distance. The shift amount, $s = n_i/n_s\, sin(\theta_i)$, is then added to all these distances. The elements whose shifted distances, $d = \pm d_0 + s$, fall within $[-1,1]$ on the axis of the oblique incidence constitute the propagating elements.

For anisotropic samples such as diffraction gratings, or samples containing a superposition of random and semi-periodic textures, other algorithms can in principle be employed to calculate the intensity distributions across different planes of interest.

Finally, to obtain the radiant AID along the direction of the oblique incidence, the power diffracted into each element is divided by its corresponding solid angle $\Delta\Omega_{\alpha,\beta} \cong \Delta\alpha\ \Delta\beta/\gamma'$, where $\gamma' = \cos(\sin^{-1} d)$. $\Delta\alpha \times \Delta\beta$.

$$\frac{I_{\beta-\beta_0}}{p_i} = K_{norm}\, f_{R,T} \times Project_{(OHS),2D\to 1D} \left\{ \left| \frac{FFT_{2D}\left\{ e^{i2\pi(n_i \pm n_s)\hat{h}(N\times N)} \right\}}{N^2} \right|^2 \right\} \Big/ \Delta\Omega_{\alpha,\beta} \tag{4.20}$$

In order to make the AID graph more readable, a smoothing algorithm is used that averages data points that fall into angle bins, the width of which is taken to match the angular opening of our goniometer detector area ~0.7°, to have a similar angular integration effect. The intensity of the specular beam is not affected by this averaging.

The AID calculations according to the algorithm (4.20) with respect to scatter angle $\theta_s = \sin^{-1}\beta$ are given in Figure 4.6, and compared to angular measurements. Calculations for all samples have good qualitative match overall with the measurements when viewed on a logarithmic axis, however there are also some noticeable differences. The power distribution remains almost completely within the unit circle in direction-cosine space.

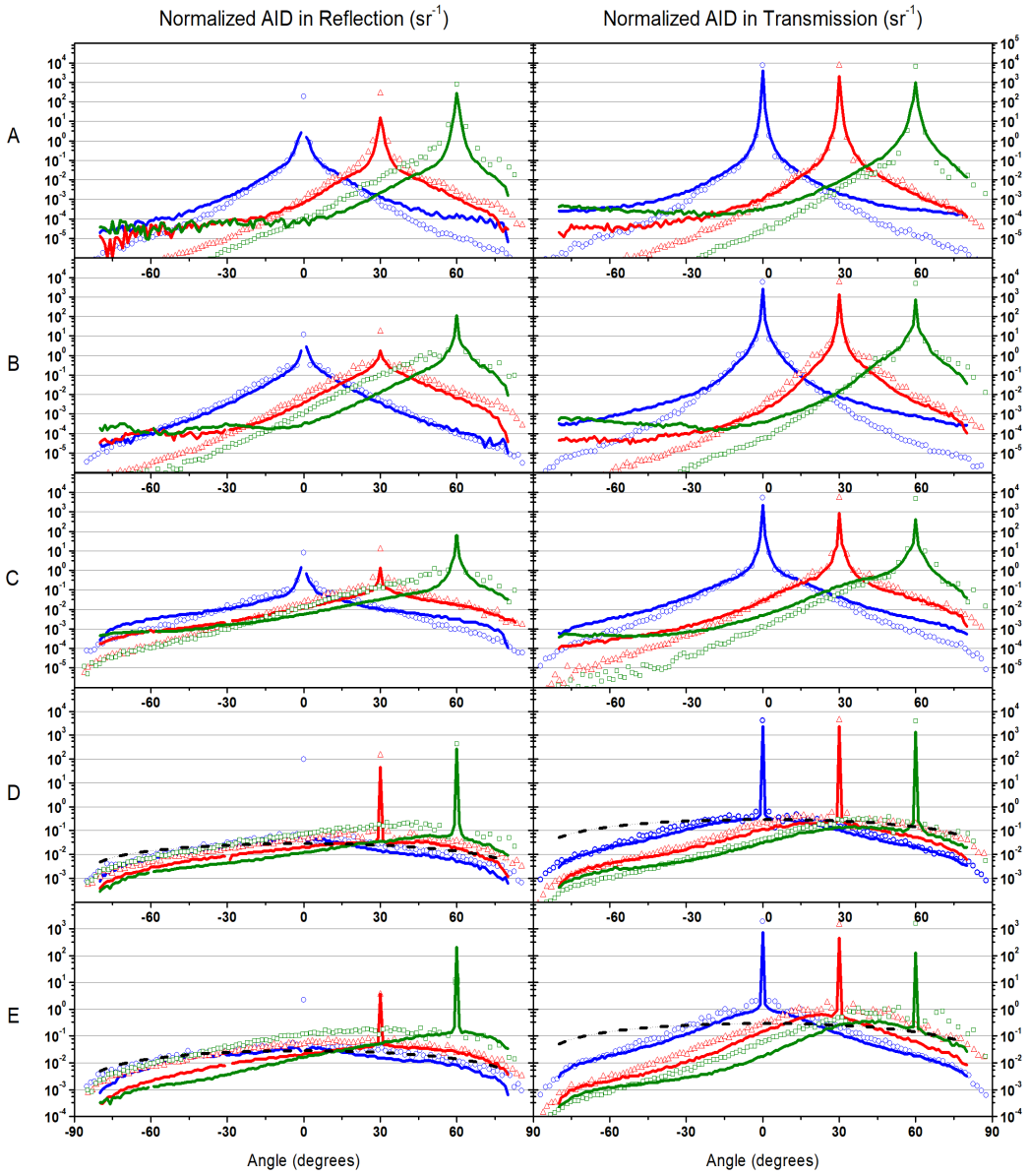

Figure 4.6. AID in reflection (right) and in transmission (left), respectively for incidence and refraction angles of 0°, 30° and 60°. Symbols represent calculations according to the OHS algorithm in (4.20), lines represent measurements. For reflection calculations, incidence is through air; for transmission, incidence is through glass (n=1.52 for samples A, B, C) or Al:ZnO (n=1.87 for samples D, E). Dashed lines represent a Lambertian intensity distribution weighted by $f_{R,T}$. Note the absence of data of a few degrees around the angle of incidence for reflected AID measurements, where the detector arm blocks incident laser beam.

The AIT etched glass samples (A, B, C) all have relatively low surface roughnesses and large autocorrelation lengths, consequently they have strong light scattering very close to the specular direction but weak scattering into higher angles, both in reflection and in transmission.

In reflection, especially for 60° incidence, calculated distributions tend to overestimate the measurements. However, in both reflection and transmission, calculated intensities fall steadily towards negative scatter angles (which will be referred to as the backscattering direction) while measurements show a plateau, which is clearly over our instrument's noise level in most cases. This plateau is already visible for normal incidence transmission in these samples, after scatter angles around 45°, and especially apparent in the backscattering direction for oblique incidence measurements, even though oblique incident reflection measurements for these samples quickly hit the noise level in the backscattering direction.

The textured Al:ZnO samples (D, E) have higher surface roughness and smaller autocorrelation lengths, with steeper local angles and feature sizes comparable or smaller to the measurement wavelength; consequently they have strong light scattering into higher angles, superimposed to a distinct specular beam that still contains a large portion of the reflected or transmitted power.

A significant proportion of the power distribution extends over the unit circle, especially in reflection and for higher angles of incidence. Consequently, diffuse components exhibit a distribution very close to Lambertian, especially in reflection.

When comparing the shape of intensity distributions, measured distributions also exhibit a relative increase in the backscattering direction. However, even more distinctly, the diffuse parts of the calculated distributions are noticeably shifted above those in measurements.

4.2.5 Surface autocorrelation method

Before the advent of the AFM techniques enabling laterally precise surface micro-topography characterization, Harvey developed, in his doctoral thesis [52], a statistical approach that uses the autocorrelation theorem of Fourier transform to model the phase variations due to the textured surface. Here a simplified version of his derivation will be presented. Using the autocorrelation theorem of Fourier transforms theory, Equation (4.11) can be expressed as:

$$\phi(\alpha, \beta - \beta_0) = K_{norm} \left| \mathcal{F}\{U_0(\hat{x}, \hat{y}; 0)\, e^{i2\pi\beta_0\hat{y}}\} \right|^2 \tag{4.21}$$
$$= K_{norm}\, \mathcal{F}\left\{ \iint_{-\infty}^{+\infty} U_{0;R,T}(\hat{x}', \hat{y}'; 0)\, U^*_{0;R,T}(\hat{x}'\text{-}\hat{x}, \hat{y}'\text{-}\hat{y}; 0)\; e^{i2\pi\beta_0\hat{y}} d\hat{x}' d\hat{y}' \right\}$$

where U_0^* denotes the complex conjugate. Once again, K_{norm} is the normalization term to redistribute power contained in evanescent modes into radiant waves, and is defined analogously to Equation (4.10).

After making the same assumptions as in the previous section, i.e. a homogeneously illuminated surface with constant reflectance and transmittance, neglecting phase variations in the near-field and near the aperture, and assuming that light accrues optical path difference vertically in the textured zone (OHS), Equation (4.15) can be substituted for the pupil function $U_{0;R,T}$:

$$\phi(\alpha, \beta - \beta_0) \tag{4.22}$$
$$= K_{norm}\, \mathcal{F}\left\{ \iint_{-\infty}^{+\infty} p_i\, f_{R,T}\, e^{i2\pi(n_i \pm n_s)[\hat{h}_1 - \hat{h}_2]}\, e^{i2\pi\beta_0\hat{y}}\, d\hat{x}' d\hat{y}' \right\}$$

In this expression, $\hat{h}_1(\hat{x}, \hat{y})$and $\hat{h}_2(\hat{x}, \hat{y})$ are two-dimensional random variables that sample the height profile ensemble $\hat{h}(\hat{x}, \hat{y})$. Harvey then makes the following additional statistical assumptions about the surface height distribution $\hat{h}$: 1) the height distribution $\hat{h}$ is Gaussian, 2) $\hat{h}(\hat{x}, \hat{y}; 0)$ is locally stationary in the statistical sense (i.e., surface is homogeneous and isotropic), 3) the random variables $\hat{h}_1(\hat{x}_1, \hat{y}_1)$ and $\hat{h}_2(\hat{x}_2, \hat{y}_2)$, produced by any two fixed pairs of spatial coordinates are jointly

normal, and 4) $\widehat{h}$ is weakly ergodic, i.e. statistics determined by space averages using a single sample function $\hat{h}_i(\hat{x}, \hat{y}; 0)$ are identical to those determined using the ensemble average $\hat{h}(\hat{x}, \hat{y}; 0)$.

Taking the expected value of random variables h_1 and h_2:

$$\phi(\alpha, \beta - \beta_0) = K_{norm}\, \mathcal{F}\left\{ \iint_{-\infty}^{+\infty} p_i\, f_{R,T}\, \mathbb{E}\langle e^{i2\pi(n_i \pm n_s)\,[\widehat{h}_1 - \widehat{h}_2]} \rangle\, e^{i2\pi\beta_0 \hat{y}}\, d\hat{x}' d\hat{y}' \right\} \tag{4.23}$$

Since the random variables are stationary, the expected value can be taken out of the integral:

$$\phi(\alpha, \beta - \beta_0) = K_{norm}\, \mathcal{F}\left\{ \mathbb{E}\langle e^{i2\pi(n_i \pm n_s)\,[\widehat{h}_1 - \widehat{h}_2]} \rangle\, p_i\, f_{R,T} \iint_{-\infty}^{+\infty} e^{i2\pi\beta_0 \hat{y}} d\hat{x}' d\hat{y}' \right\} \tag{4.24}$$

This is the joint characteristic function of two jointly normal random variables. It can be shown that [89], Equation 4.24 is equivalent to:

$$\frac{\phi(\alpha, \beta - \beta_0)}{p_i} = K_{norm}\, f_{R,T}\, \mathcal{F}\left\{ e^{-(2\pi(n_i \pm n_s)\hat{\sigma})^2 \left[1 - \frac{ACF(\hat{x}, \hat{y})}{\sigma^2}\right]}\, e^{i2\pi\beta_0 \hat{y}} \right\} \tag{4.25}$$

As previously, the $e^{i2\pi\beta_0 \hat{y}}$ term in the Fourier transform produces the shifting effect of an oblique angle of incidence in direction cosine space. The other terms in the Fourier transform can be regarded as the transfer function of the surface. It is also possible to analytically separate this formulation into a sum of direct and diffuse parts of the reflected or transmitted power distribution [52,59].

Within the assumptions used in its derivation, Equation (4.25) is equivalent to Equation (4.16) of the DPS approach. For our isotropic samples, the algorithm procedure of Figure 4.7 can then be used to calculate the AID. Figure 4.7 compares intensity distributions calculated using DPS and ACF methods, for samples B and

D, where the ACF has been calculated by inverse FFT_{2D} transforming the PSDF function.

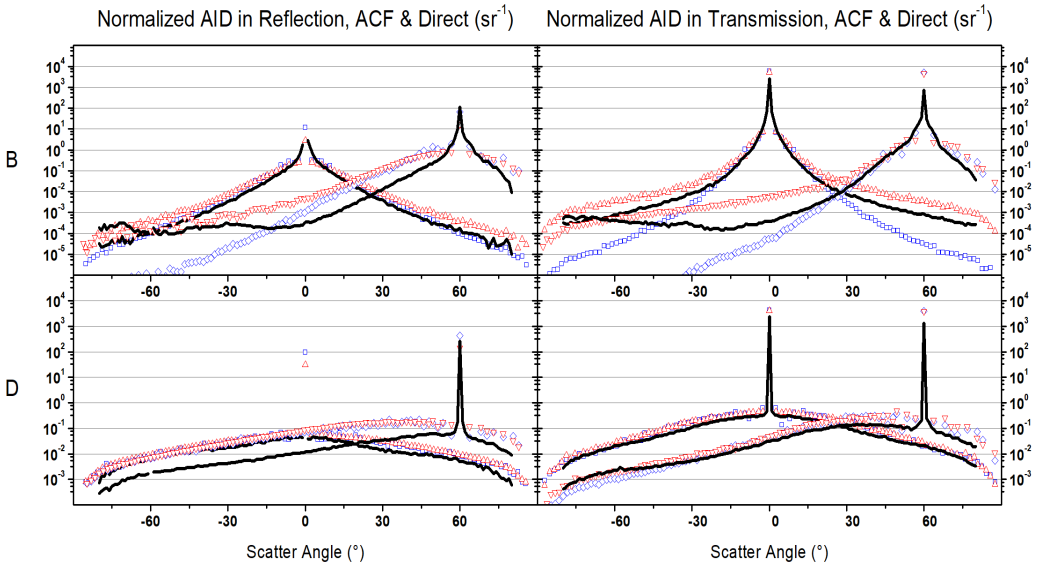

Figure 4.7. Comparison of AID calculated with OHS pupil function using DPS (blue squares) and ACF (red triangles) methods, together with angular measurements (line) for samples B and D.

The two methods yield virtually identical results for Al:ZnO samples (exemplified by D), which are very homogeneous at the 25 µm length scale of their AFM scan and have Gaussian radial ACF, despite the negative skew in their height distributions.

However, for AIT glass samples (exemplified by B), which exhibit a two-scale superposed height distribution (and two-Gaussian radial ACF), the ACF method clearly overestimates the intensity scattered to higher angles. This is probably because, unlike in the DPS approach, the reference plane with regards to which heights are measured is important in ACF method because it directly influences the $\hat{\sigma}^2$ and $ACF(\hat{x},\hat{y})$ parameters. Likewise, the superposition of the larger length scale due to the intermediate Si precipitates disturbs this reference and inflates the $\hat{\sigma}^2$

value. Moreover, for these samples, the ACF method AID also tend to flatten near the specular direction, while being superimposed to the distinct specular peak; the DPS method seems to better reproduce the progressive, gradual shape observed in measurements.

One of the most important advantages of this ACF method is that, multiple PSDFs obtained from different locations on the sample can be averaged [58,90,91], reducing the possible effect of local statistical variations, instead of relying on a single image that naturally has less "ergodic" fidelity. PSDFs originating from various surface measurement techniques that have different spatial frequency bandwidths can also be combined to obtain extended PSDFs [8,90], if needed.

For isotropic samples, a $PSDF_{2D}$ function can be azimuthally averaged; for anisotropic samples, cross sections of the $PSDF_{2D}$ surface can be taken across relevant optical directions. In the scientific community, the resulting $PSDF_{1D}$ functions are usually fitted with analytical functions (usually Gaussian or K-correlation functions) [49,59]. Such fitting parameters can give additional insights into surface characteristics. The ACF function (and thus angular power distribution quantities) can then be calculated analytically.

Overall, the ACF approach transforms the scattering problem into a method better suited to parametrization and statistical averaging, (and will provides a basis for the correction term proposed in section 4.4.1), at the cost of an extra computational step and possible loss of generality. While noting the advantages of the ACF approach, the more direct DPS approach will be used in the remainder of this dissertation for the sake of simplicity and robustness.

4.3 Generalized Harvey-Shack theory

Although the OHS theory gives qualitatively adequate results, the vertical optical phase accumulation model is clearly an oversimplification. Furthermore, it has been pointed out by several authors that, when the OHS pupil function is applied to a

surface containing a single facet angle, as can be found in a large pyramid texture, the main angle of diffraction predicted by the OHS theory increasingly overestimates the refraction angle predicted by Snell's law, as the surface facet angle increases [43,51]. Figure 4.8 illustrates this point for normal incidence reflection and transmission.

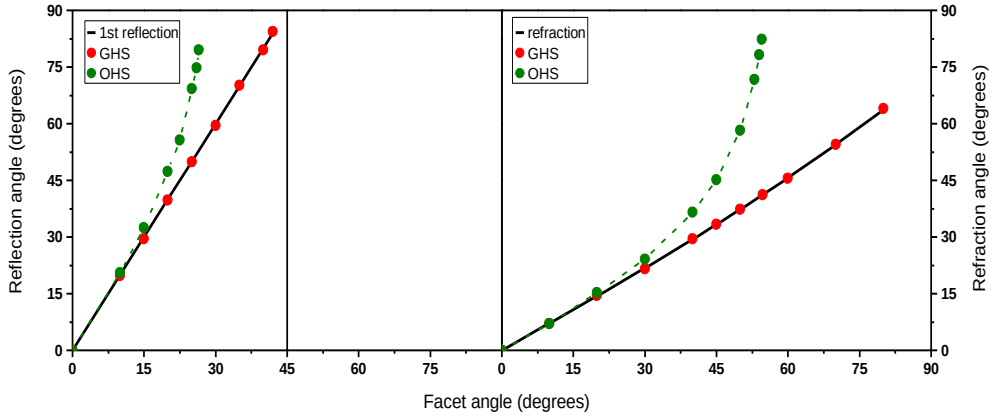

Figure 4.8. Diffraction angles in reflection and transmission predicted by OHS and GHS theories for normally incident light (λ=532 nm) on a Si pyramid surface with varied facet angles, and compared to reflection and refraction angles. n1=1 n2=3.5. Partly adapted from [51].

Already at the end of his thesis in 1976, Harvey hints at a more realistic pupil function that takes into consideration the phase differences induced by the surface texture and depending on incidence and scatter angles. The corrected pupil function is in fact that which was used by Carniglia in the context of total integrated scatter [79], and corresponds to the optical path difference accumulated by a light ray with a given incident and scatter angle when reflected off or transmitted through the surface profile; compared to a light ray with the same incident and scatter angles interacting with a flat surface, as illustrated in Figure 4.9. Alternatively, this pupil function also corresponds to the difference in the vertical components of incident and scattered plane wave wave-vectors.

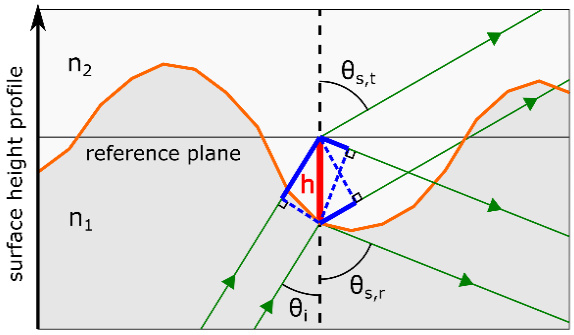

Figure 4.9. GHS interface optical path difference accumulation model.

The optical path difference and improved pupil functions become:

$$\hat{o}_{GHS} = (\gamma_i n_i \pm \gamma_s n_s)\, \hat{h}(\hat{x}, \hat{y}) \tag{4.26}$$

$$U_{0;GHS}(\hat{x}, \hat{y}; \gamma_i, \gamma_s, 0) = \sqrt{p_i\, f_{R,T}}\; e^{i2\pi(\gamma_i n_i \pm \gamma_s n_s)\, \hat{h}(\hat{x},\hat{y};0)} \tag{4.27}$$

where γ_i and γ_s are cosines of incident and scatter angles respectively. Once again, the plus sign is used for scattering in reflection, where $n_i = n_s$ also; and the minus sign is used for scattering in transmission.

This generalized version of Harvey-Shack (GHS) theory was first introduced by Krywonos et Al from 2006 [56,57,59], and was first used in the solar cell community by Haug et Al. by 2016 [51]. With this generalization, Harvey-Shack theory becomes truly non-paraxial, as illustrated by Figure 4.8, i.e. all residual phase differences originating from the textured interface or the diffraction process itself (except those that are negligible in the far-field) are accounted for.

Corrected expressions for power and are obtained by simply replacing the pupil functions in Equations (4.16) and (4.25) respectively:

$$\frac{\phi_{GHS/DPS}(\alpha, \beta - \beta_0)}{p_i} = K_{norm}\, f_{R,T} \left| \mathcal{F}\left\{ e^{i2\pi(\gamma_i n_i \pm \gamma_s n_s)\, \hat{h}(\hat{x},\hat{y};0)}\; e^{i2\pi\beta_0 \hat{y}} \right\} \right|^2 \tag{4.28}$$

$$\frac{\phi_{GHS/ACF}(\alpha, \beta - \beta_0)}{p_i} \tag{4.29}$$

$$= K_{norm}\, f_{R,T} \left| \mathcal{F}\left\{ e^{-(2\pi(\gamma_i n_i \pm \gamma_s n_s)\hat{\sigma})^2 \left[1 - \frac{ACF(\hat{x},\hat{y})}{\sigma^2}\right]} e^{i2\pi\beta_0 \hat{y}} \right\} \right|$$

However, using the GHS pupil function for any given incidence angle, every scatter angle now requires a different 2D FFT operation; and in the resulting 2D phase screen, only the matrix element corresponding to that particular scattering angle is relevant. Simple shift invariance due to the single Fourier transform is foregone. The complex amplitude distribution and related power distribution need to be reconstructed using elements of a "two-parameter family of Fourier transforms" [59], one element at a time. This is more demanding computationally, although it can still be handled by a personal computer thanks to the speed of FFT algorithms, at least for single layer scattering simulations.

In order to accomplish this, a modified version of the previous algorithm (Equation (4.20) in Figure 4.5) is used. Among NxN elements, only those (p, q) whose shifted distances, $d = \pm d_0 + s$, fall within $[-1,1]$ on the axis of the oblique incidence in direction-cosine space correspond to valid scatter angles. The FFT operation of Equation (4.17) (with the corrected pupil function) is performed for each of these elements (p, q) using their corresponding scatter angle cosines γ_s, and in the result, only the value of the element (p, q) is retained, associated to shifted distance $d = sin\,\theta_s$. The radiant AID_{1D} in the plane of the oblique incidence is reconstructed element-by-element, after scanning for all valid elements mapping to within $[-1,1]$. With this algorithm, the isotropicity of the sample can still be exploited to obtain well averaged $I_{1D}(\theta)$ results.

For anisotropic samples such as diffraction gratings, or samples containing a superposition of random and semi-periodic textures, other algorithms can in principle be employed to calculate the $I_{1D,\varphi}(\theta)$ across different planes of interest.

Using the GHS pupil function, complex amplitudes corresponding to evanescent modes lying outside the unit circle are undefined. However, due to the conservation

of energy, the sum of the normalized power distribution inside the unit circle (before applying the $f_{R,T}$ term), should be equal to 1. After calculating the radiant power distribution $\phi_{GHS}(\alpha, \beta - \beta_0)$ inside the shifted propagation hemisphere (in a separate scan step), K_{norm} can still be defined as the inverse of the total radiant power contained inside the unit circle.

$$K_{norm} = \frac{1}{\sum_{\alpha^2+\beta^2 \le 1} Reconstruct_{2D}\left\{\left|\frac{FFT_{2D}\left\{e^{i2\pi(\gamma_i n_i \pm \gamma_s n_s)\hat{h}(N\times N)}\right\}}{N^2}\right|^2\right\}} \tag{4.30}$$

Hence, the radiant AID in the plane of incidence becomes:

$$\frac{I_{\beta-\beta_0}}{p_i} = K_{norm}\, f_{R,T} \tag{4.31}$$
$$\times\, Project_{(GHS),2D\to 1D}\left\{\left|\frac{FFT_{2D}\left\{e^{i2\pi(\gamma_i n_i \pm \gamma_s n_s)\hat{h}(N\times N)}\right\}}{N^2}\right|^2\right\} \Big/ \Delta\Omega_{\alpha,\beta}$$

where $Project_{(GHS),2D\to 1D}$ with brackets denotes the element-by-element reconstruction algorithm.

Figure 4.10 compares the cosine function GHS optical path differences to the constant OHS optical path difference, for several angles of incidence, with respect to scatter angle. The GHS optical path difference multipliers ($\gamma_i n_i \pm \gamma_s n_s$) inside the exponential cause the phase accumulation to tighten (or loosen) for different scatter angles compared to the constant ($n_i \pm n_s$) OHS phase accumulation, as if the surface texture height is increased or decreased for that scatter angle. During the Fourier transform step, a tighter phase screen (with higher frequency content) has the effect of distributing more power into higher frequencies (and angles) at the expense of the central, specular frequency, and vice versa.

Note that for reflection, regardless of the incidence side, GHS pupil function is always below that of OHS, hence it results in less power distribution to higher scatter angles, compared to OHS. This difference increases with incidence angle.

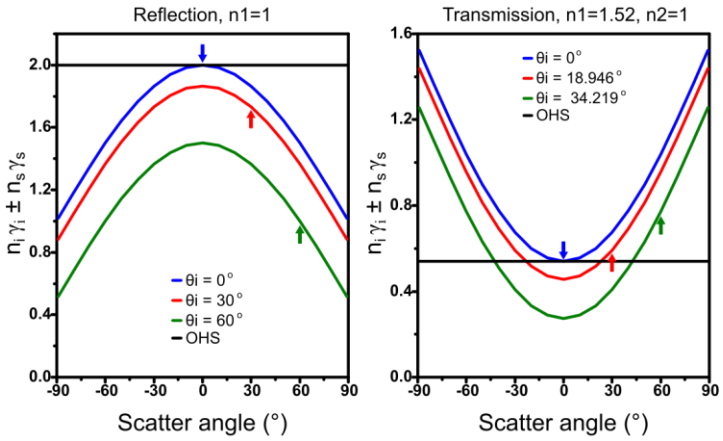

Figure 4.10. Comparison of OHS and GHS pupil functions. a) Reflection into n=1, for 0°, 30° and 60° incidence angles. b) Transmission from n_1=1.52 to n_2=1, for 0°, 30° and 60° refraction angles. c) Transmission from n_1=1 to n_2=1.52, for 0°, 30° and 60° incidence angles.

For transmission, there are scatter angles where the GHS and OHS optical path differences become equal, hence, depending on the relative refractive indices, there are spatial frequency/scatter angle regions where GHS theory predicts more (or less) scattering power compared to OHS theory. Specifically, for normal incidence transmission to a lower refractive index medium, GHS theory predicts more power scattered to higher angles. However, with increasing incidence angles, there appears a region around small polar angles where predicted scatter is less than for OHS path difference.

Note that this discussion does not take into account the normalization constant due to redistribution of power contained in evanescent frequencies, which might also differ between the two implementations.

With these effects in mind, the results of the AID calculations with respect to scatter angle $\theta_s = \sin^{-1}\beta$ according to the GHS algorithm (4.31) are given in Figure 4.11, and compared to angular measurements.

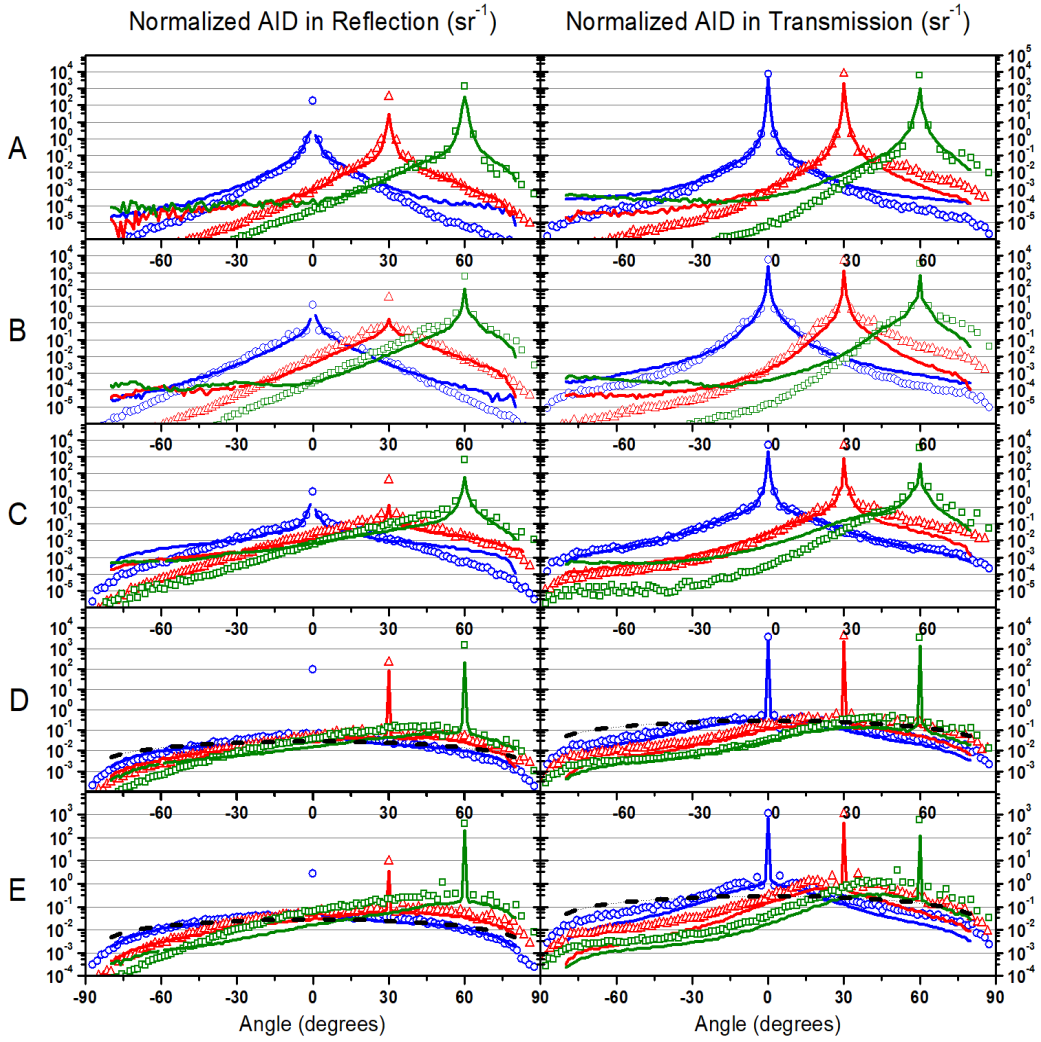

Figure 4.11. AID in reflection (right) and in transmission (left), respectively for incidence and refraction angles of 0°, 30° and 60°. Symbols represent calculations according to the GHS algorithm in (4.31), lines represent measurements. For reflection calculations, incidence is through air; for transmission, incidence is through glass (n=1.52, for samples A, B, C) or Al:ZnO (n=1.87, for samples D, E). Dashed lines represent a Lambertian intensity distribution weighted by $f_{R,T}$.

Most of the observations made for comparisons with OHS calculations hold true for GHS calculations as well.

In reflection, GHS pupil function causes more power to concentrate in the specular beam at the expense of the diffuse distribution, leading to a significantly better experimental fit, especially around the specular direction.

In transmission, the tweaks brought by GHS pupil function also result in a better experimental fit around the central polar angles as well as the specular direction.

Arguably, the improvements brought by GHS theory are relatively minor for our samples, and concern mainly intensity levels in specular beam for high angles of incidence. They might not always justify the increased computational cost, or rather, for the samples in this study OHS might be adequate enough. This is because, unlike pyramid textures or diffraction gratings (where most of the power is diffracted into specific, non-specular angles), randomly textured samples do not exhibit a discrete diffraction behavior, and even in highly diffusive surfaces most of the diffracted power is still concentrated around the specular direction, where the optical path differences between the two implementations are usually not too large.

However, two notable deviations remain:

Firstly, for AIT glass samples, calculated intensities for oblique incidence in both reflection and transmission fall steadily towards in the backscattering direction, while measurements show a plateau, which is clearly over our instrument's noise level in most cases. This plateau is already evident in normal incidence transmission for sample A and B, above scatter angles around 45°. Similar plateaus can also be observed in AID measurements published in previous literature [48]. Moreover, for AIT glass samples, calculated intensities in the forward scattering direction around and beyond the non-diffracted beam angle appear to be overestimated, especially in transmission.

For Al:ZnO samples, the magnitude of the calculated intensity distribution also exhibits a relative decrease in the backscattering direction when compared to measurements, but this is compounded by another distinct, second deviation: The diffuse parts of the calculated intensity distributions are noticeably shifted up and overestimated compared to their measured levels.

The possible explanations for these two observations will be discussed in the following sections.

4.4 Discussion on limitations and improvements to GHS theory

4.4.1 An effective medium correction factor?

The persistent overestimation of diffuse intensity compared to measurements for Al:ZnO samples with relatively rough surfaces and small lateral autocorrelation lengths suggest that the phase screen that is Fourier-transformed in Equation (4.27) could be too dense. Here, I propose a correction factor c in the pupil function such that $c < 1$, which results in a better empirical match with the measurements:

$$U_{0;GHS}(\hat{x}, \hat{y}; \gamma_i, \gamma_s, 0) = \sqrt{p_i \, f_{R,T}} \, e^{i2\pi(\gamma_i n_i \pm \gamma_s n_s) c(\gamma_i, \gamma_s) \hat{h}(\hat{x}, \hat{y}; 0)} \tag{4.32}$$

At this point, it is important to mention an improvement that has been made to the ACF version of GHS theory [57-59]. Recall that the surface roughness parameter σ in the power distribution Equation (4.25) is a quantity spread over spatial frequencies, this frequency distribution being given by the $PSDF_{2D}$ function.

Just like a grating whose period is too small compared to wavelength, high spatial frequency components will not produce optical diffraction, only evanescent waves; hence they are not "relevant" to diffraction [8,11,71]. Roughness components relevant to optical interaction can be calculated by integrating the $PSDF_{2D}$ distribution over the relevant frequency range, given by a circular domain of radius n_s/λ, shifted from the center of the $PSDF_{2D}$ by $n_i \sin\theta_i / n_{r,t} = \sin\theta_{r,t}$ for an

oblique angle of incidence [11,59]. The resulting relevant roughness σ_{rel} should replace the first σ parameter in Equation (4.25) [11,59], (but not the second, as the σ term in the denominator simply normalizes the peak of the ACF_{2D} to unity). This relevant roughness is not an intrinsic surface property, and depends, beside the surface related PSDF distribution, on the optical wavelength, incidence angle and refractive index of the medium into which scattering occurs.

Furthermore, this relevant roughness σ_{rel} can fit the bill for the corrective coefficient c, since it is a fraction of total roughness σ, which decreases with increasingly rough samples and increasing angles of incidence, as roughness components are pushed out of the relevant range.

The equivalent modification is missing in the DPS implementation, it can be introduced by setting $c(\gamma_i) = \sigma_{rel\,r,t}/\sigma_{tot}$ in the phase term. However, although the ratio $\sigma_{rel\,r,t}/\sigma_{tot}$ provides a theoretical basis in the right direction for a corrective term, for our samples it is very close to unity except at very oblique angles, and is not enough to explain the observed effect. A dichotomous search algorithm has been used in order to find the c coefficients that result in an optimal fit between calculations and measurements.

For normal incidence transmission, numerous scatter measurements were repeated from different locations across each sample, resulting in statistical variations at each scatter angle. These variations result from uncertainties due to instrumentation as well as the stochastic nature of surface scattering phenomenon itself. Intensity values calculated using the empirical pupil function given in Equation (4.32) were interpolated at measurement angles, and the squared difference between these two intensities was multiplied by $|\sin\theta_s|$. As explained in section 2.5.1, this is because for a sample with isotropic surface texture at normal incidence, the quantity $I(\theta_s) \times |\sin\theta_s|$ is proportional to the total intensity scattered across the entire hemisphere at a radial angle θ_s, not just a cross section of it as in angular measurements [42,43]. The non-diffracted peak values, where experimental uncertainties are greatest, are not taken into account. The c value resulting in the

least total residual error was determined after several iterations. This dichotomous parameter search was repeated using curves one standard deviation lower and higher than the average $I_{1D}(\theta)$, to give an estimation of the variability range of the correction factor. These optimized c coefficients and their expected range are given in Table 4.1, together with other relevant surface parameters.

Table 4.1 Empirical corrective coefficients, for normal incidence transmission, obtained using a dichotomous search optimization. Asterisks indicate values taken from the optically relevant part of two-Gaussian fit of radial autocorrelation function.

	A	*B*	*C*	*D*	*E*
σ_{tot} (nm)	20.5*	67.0*	70.0*	82.7	129.4
acl (nm)	889*	1166*	768*	321	527
most likely local angle	2°	5°	7.5°	14°	23°
$\sigma_{rel}/\sigma_{tot}$	0.996	0.997	0.996	0.965	0.989
optimized c coefficient	1.175 [0.975;1.325]	1.025 [0.825;1.250]	0.950 [0.825;1.075]	0.750 [0.600;0.900]	0.575 [0.425;0.750]

As expected, correction factors for AIT glass samples with broad textures are close to unity. Deviations, while significant, probably result from AFM images not being representative enough of these samples, with limited homogeneity at this length scale owing to their larger features, as well as goniometric measurement uncertainties. Furthermore, since these samples have high intensity distributions close to the non-diffracted beam, slight experimental deviations in those few data points can offset the optimization result.

Corrective factors for both Al:ZnO samples are significantly less than 1; with sample E exhibiting the steepest angles that require the smallest factor. While deviations remain significant, a corrective factor beyond the $\sigma_{rel\,r,t}/\sigma_{tot}$ ratio is the likeliest explanation. Other factors specific to Al:ZnO samples, such as scattering caused by residual roughness in the nominally flat glass/ZnO interface, would all have the opposite effect of greater scattering into high angles in measurements.

AID calculations with optimized c coefficients are shown in Figure 4.12. Also included are transmission calculations with correction factors for refraction angles of 30° and 60°, (calculated without the $|\sin\theta_s|$ multiplier to intensity), but the dichotomous search fitting is less reliable in oblique incidence, due to the compounding effect of the secondary interactions on the measured $I_{1D}(\theta)$ AID, which is the subject of the next section.

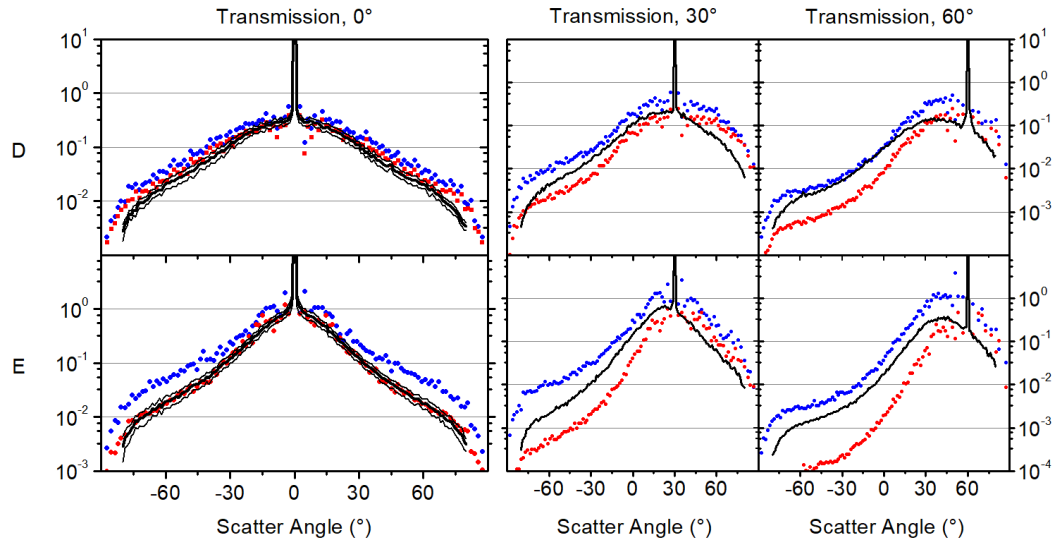

Figure 4.12. AID in transmission, for refraction angles of 0°, 30° and 60°, for samples D and E, calculated with optimized corrective coefficients (red triangles) for fitting measurements (lines), and without the corrective coefficient (blue squares).

A possible physical explanation for this behavior could be the onset of effective medium effects, which are not taken into account in SST. These samples exhibit moderately large vertical and small lateral features compared to the wavelength in the material, resulting in relatively steep local surface angles. The incident light around peaks and pits of these textures experiences a gradual refractive index change, resulting in less overall optical phase accumulation compared to a texture

with abrupt refractive index change. This would manifest as an effective reduction in the height profile of the roughness zone.

Consider hypothetical pyramidal textures as illustrated in Figure 4.13: a) features a steep facet angle with a large base, corresponding to the geometric optics regime. b) contains small heights with dimensions at the order of the wavelength and large lateral features (similar to sample A and B). It has slow phase accumulation due to shallow slopes, which results in weak scattering at high angles. c) features a facet angle identical to a), however with small heights at the order of the wavelength as b), but with smaller lateral features. Even though the phase accumulation on each facet is identical to that of a), there are numerous regions with comparatively small phase change around tips and pits, which translate to reduced high frequency content in the Fourier transform, when compared to a). Moreover, c) is more susceptible to effective medium approximation due to reduced feature dimensions, such that the effective height profile starts to decrease compared to the actual profile around tips and pits, which also decreases high angle scattering. According to Equation (4.27), in order to enhance high angle scattering from a small texture, facet angles could be increased as in d), similar to samples D and E with their skewed height distribution. However, pronounced reduction of effective height profile due to effective medium effects opposes this enhancement.

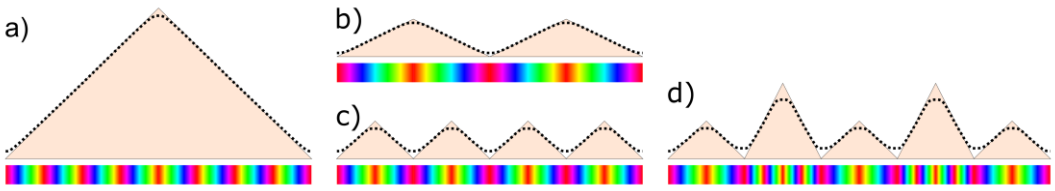

Figure 4.13. Phase accumulation on pyramid facets with different facet angles and sizes. Colors stand for the optical phase accumulated when light traverses each profile. Dotted lines suggest an equivalent height profile, encompassing effective medium effects

Consider now the missing $\sigma_{rel\,r,t}/\sigma_{tot}$ ratio. The smaller textures c) and d) would have PSDF that extend more toward high spatial frequencies, and therefore have smaller corrective $\sigma_{rel\,r,t}/\sigma_{tot}$ ratios compared to the larger textures a) and b). However, this ratio is very close to unity in our samples for normal incidence, even though the features are already smaller than to the wavelength. Therefore, a correction factor due to effective medium effects might be more than merely a DPS method analogue of the $\sigma_{rel}/\sigma_{tot}$ correction ratio.

If the roughness zone between the material and air acts like a graded medium, another consequence would be a decrease in reflectivity and increase in transmissivity compared to that given by Fresnel coefficients for a flat interface. This additional change will be proportionally much more important in reflection. Moreover, in normal incidence reflection, light reflected from the sample backside and transmitted from the front is superimposed on the desired first reflection scatter, which nearly doubles the measured signal, and masks the observed discrepancy. The analogous effect in transmission scatter is negligible. These effects prevent a similar quantitative dichotomous search for reflection. However, the presence of the same overestimation in the $I_{1D}(\theta)$ AID for oblique incidence reflection compared to measurements, where reflection from the substrate backside is blocked by the aperture, Figure 3.2b, suggests that a similar phenomenon also exists in reflection for the Al:ZnO samples D and E.

Effective medium approximation is a complicated phenomenon, and an associated correction factor, if confirmed, would likely be a complicated function of the autocorrelation length, surface roughness, refractive indices as well as the local surface geometry (volume fraction and distribution of local angles). The uncertainties inherent in the metrology of AID measurements are not insignificant, and further investigations with a greater range of samples and shorter wavelength lasers are needed to confirm the existence of an effective medium correction factor.

4.4.2 Effects of secondary interactions

Another general limitation of SST is that it concerns only primary interactions of incident light with the surface. As such, shadowing events and secondary interactions at the surface topography are not considered. A possible explanation for the increased backscattering and reduced forward scattering observed across the samples is a redistribution of part of the scattered power due to the presence of such secondary interactions. This broad backscattering enhancement is of course distinct from the localized, coherent retroreflection phenomenon predicted by higher order small-amplitude perturbation approaches [81-83].

The angle between a local facet plane and light scatter direction decreases with a high content of surface slope angles and with increasing scatter angle, rendering a secondary interaction more likely, in which scattered light reflects off another adjacent surface topographic feature. A similar argument can be made with increasing incidence angles and the probability of shadowing events, where a tall local surface feature blocks light from reaching the average surface plane.

While it is not possible to know the effects of such interactions without performing rigorous calculations on well-defined surface geometries, it can be suggested, as a first approximation, that a secondary interaction tends to spread out the power contained in affected (forward) directions to all scatter directions more-or-less equally. Since for a random texture, the forward scatter direction close to the non-diffracted beam contains much more scattered power, a slight redistribution away from this direction could compensate for a large relative increase across all backscatter directions.

Notably, these scatter events do not take place only on the plane of incidence, (which is the plane of AID measurements), they affect the light scattered in any azimuthal direction with similar probability. A small part of this light undergoing secondary interaction across a different azimuthal direction could scatter back in the plane of incidence and be detected by the scanning detector. However, unlike primary

scattering in the plane of incidence, such interactions involving other azimuthal directions would result in a change in the polarization direction of the detected light, as illustrated in Figure 4.14a.

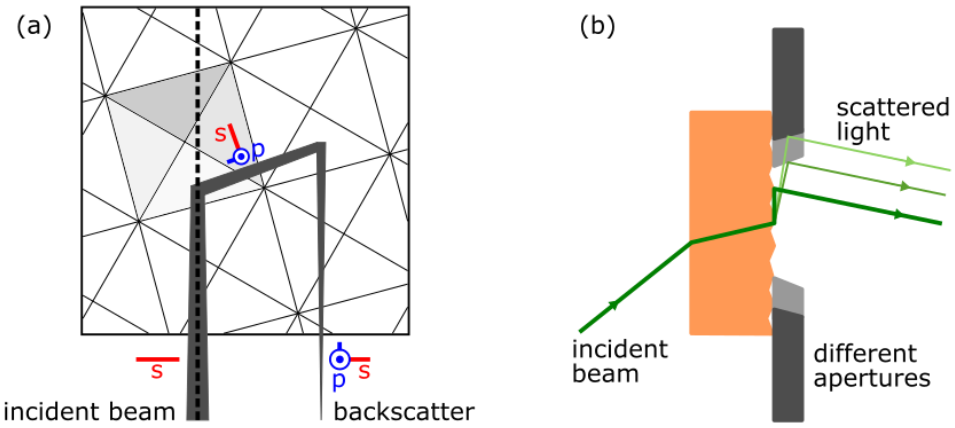

Figure 4.14. a) Illustration of secondary interactions on a pyramid-like surface texture, top view. b) Side view of goniometer aperture illustrating a secondary interaction from the surface topography (dark green line) or sides of the aperture with different radii (lighter green lines).

To test this hypothesis, some of the scatter measurements were repeated with a polarizer placed in front of the scanning detector. These results are given in Figure 4.15 (Left), and exhibit a proportional increase of intensity measured with p polarizer in the backscattering direction (or towards high angles for normal incidence), and reduction of intensity measured with s polarizer. This observation is in line with the possible presence of secondary interactions that could explain the backscattering plateaus in the angular measurements in Figures 4.6, 4.7, 4.11 and 4.12.

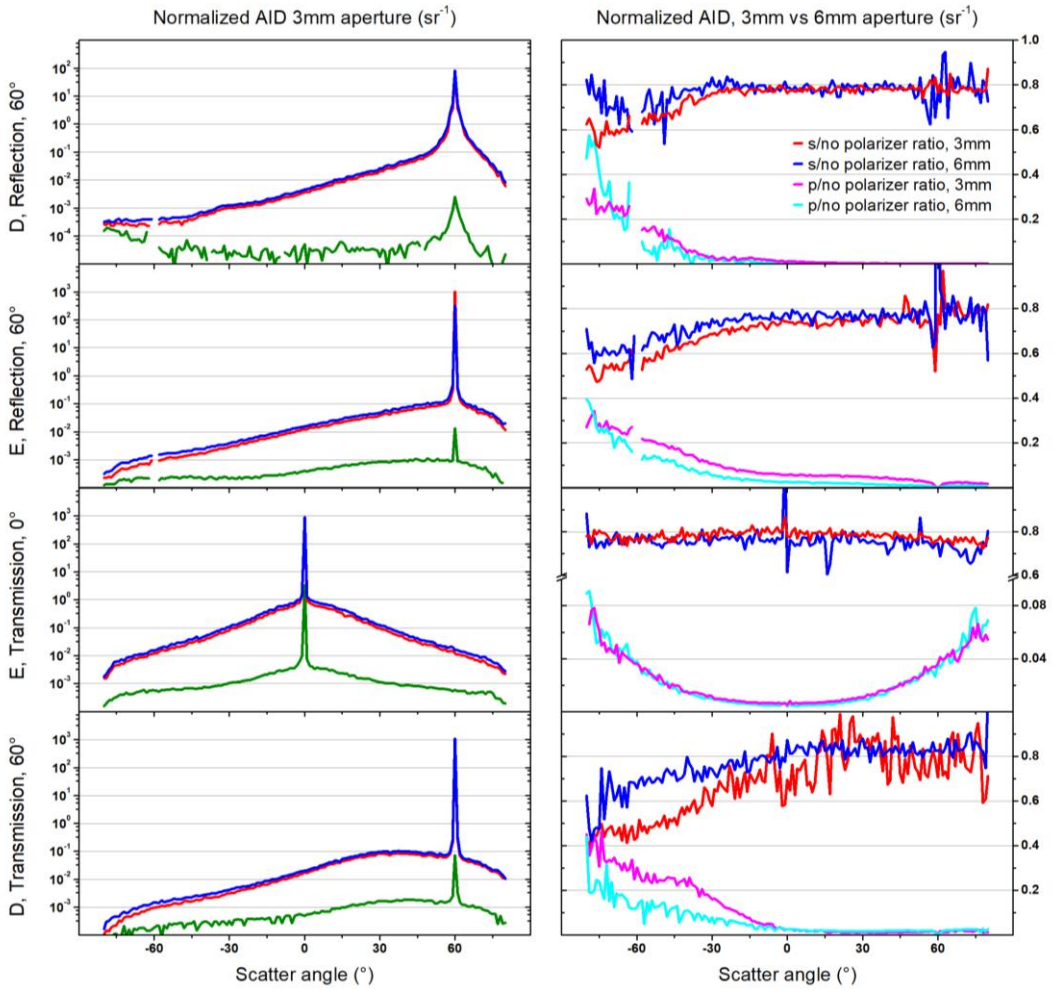

Figure 4.15. Left: AID measurements with s polarizer (red), p polarizer (green) and without polarizer (blue) in front of the detector. Incident beam is s polarized. Right: s/no polarizer and p/no polarizer ratios, measured using 3mm and 6mm diameter aperture sizes.

However, it is also possible that the observed polarization changes have a non-topographic, experiment-related source. For example, such secondary scattering events could also happen on the sides of the small aperture surrounding the sample surface, as illustrated in Figure 4.14b. In order to check for this instrumentation effect, the previous measurements were repeated using apertures of different diameters, 3mm and 6mm. The sides of a larger diameter aperture, that has the same

thickness as a small diameter one, subtends a smaller solid angle with respect to the incident beam area, and therefore should produce fewer secondary interactions, if non-topographic secondary scattering is predominant. The resulting s/no polarizer and p/no polarizer intensity ratios are given in Figure 4.15 (Right), and show little difference, suggesting that secondary interactions are indeed originating from the surface topography.

From a purely geometric optics perspective, the effect of secondary interactions should be negligible for the small slopes composing our samples. The redistribution of power to all combined backscatter directions should indeed make up a small percentage of the overall radiated power, which is concentrated mainly near the non-diffracted beam direction. But the effects are still detectable, and the superposition makes precise quantitative interpretation of low level scattering difficult. While it is not possible to integrate these effects directly into the pupil function, it might be possible to add them to the 2D power distribution map heuristically.

An example to a case where secondary interactions seriously change the scattered power distribution could be found in the large pyramid texture of Figure 4.8. GHS SST naturally predicts that a facet with 45° slope reflects normally incident light parallel to the surface. Beyond this facet angle, all power distribution is evanescent. However, it can be readily shown that normally incident light reflects twice from a textured crystalline silicon surface with 54.7° slope pyramids, resulting in a final reflected ray with an angle around 39° (4*54.74°-180°) with respect to the normal direction; and the reflected intensity is less than that expected from a single pass Fresnel coefficient due to the additional interaction. In textures where these effects are dominant, such as with large anisotropic features, SST should be supplemented by ray tracing or some other rigorous methods.

4.5 Scattering into optically denser media

Scattering into an optically denser medium with refractive index n_s can be handled with the same algorithms, but keep in mind that spatial frequencies of the Fourier transform, i.e. direction cosines, $\Delta\alpha = \Delta\beta = \lambda/(L\, n_s)$ depend on n_s.

In Figure 4.16, the GHS optical path difference multiplier $|\gamma_i n_i - \gamma_s n_s|$ is plotted with respect to scatter angle, for scattering in transmission into n_s=1.87.

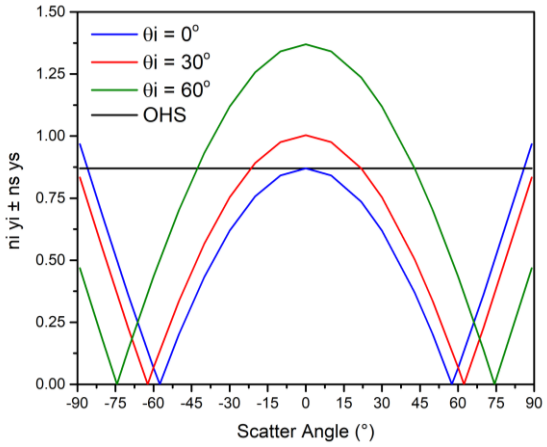

Figure 4.16. GHS pupil function, with respect to scatter angle, transmission from n_1=1.87 to n_2=1, for 0°, 30° and 60° incidence angles.

Interestingly, GHS model predicts that for transmission to a medium with higher refractive index, there are scatter angles corresponding to the condition ($\gamma_i n_i = \gamma_s n_s$) for which the optical path difference becomes zero, hence there is no diffraction and power distribution vanishes at those angles. The simpler OHS model does not have this property.

To illustrate this, AID results calculated using GHS Equation (4.31) for light incident from air and scattering from sample D are given in Figure 4.17 (blue lines), for 0° and 30° angles of incidence. Sample D was chosen because, in both reflection and transmission into air, it has a near Lambertian scattering response that is easy to interpret.

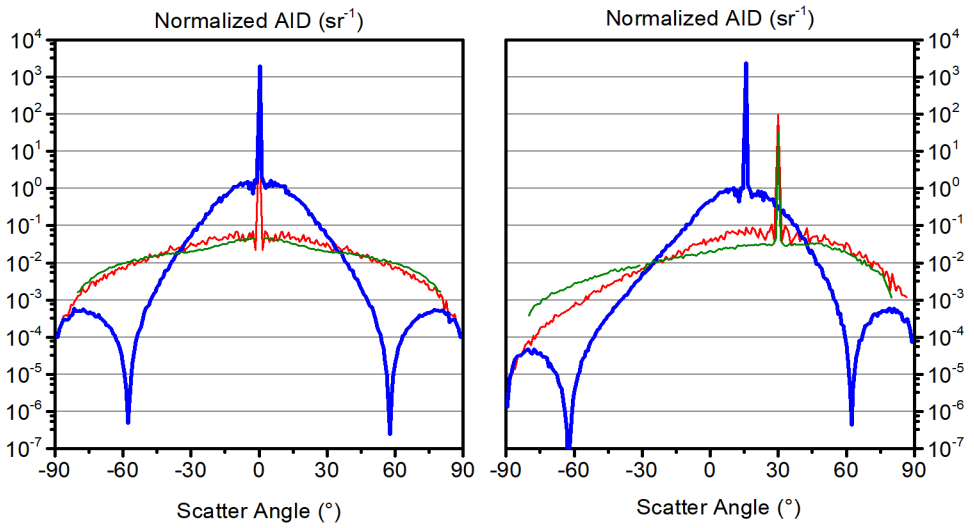

Figure 4.17. AID calculations for light scattering from sample D, for 0° and 30° incidence from air. Blue lines show transmission into ns=1.87, red lines show reflection into air, (green) lines show reflection measurements.

Experimental verification of AID in transmission into an optically denser medium in general, and the dips in scatter corresponding to the condition ($\gamma_i n_i = \gamma_s n_s$) in particular are very difficult, and would require specialized configurations [51,92] with well-aligned spherical lenses. Even with such a configuration, a slight redistribution of power due to secondary interactions could render the observation of low-level dips impossible.

This phenomenon is to be contrasted with the Yoneda phenomenon [78,85] predicted by the reduced Rayleigh equations method for weakly rough surfaces and verified experimentally [92]. It consists of a sharp peak in scattered power just above the critical angle, when the scattering occurs into the optically denser medium. This arises from the coupled nature of the tangential wave vectors of the scattered reflected and transmitted modes, and is independent of the angle of incidence [78]. When a mode scattered into the optically less dense medium becomes evanescent, its scattered power is redistributed into its coupled mode scattered into the optically denser medium. It can be considered a scattering analogue of Rayleigh's anomalies observed in gratings. SST does not take into account effects such as the coupling

between individual scattered reflected and transmitted modes. In this model, the coupling between reflected and transmitted scatter is done at the hemisphere level using $f_{R,T}$ coefficients, after the angular distribution for each has been calculated using the RS diffraction integral.

However, if the prediction of dips in the transmission AID into an optically denser medium holds, the scattered power would be more constrained around small polar angles. The $I_{2D}(\theta, \varphi)$ AID distribution, which is very nearly Lambertian in air, would not extend into higher angles. As a consequence, GHS SST predicts that Lambertian randomization, necessary for $4n^2$ Yablonovitch limit light trapping, cannot be obtained by a single pass from the front surface of a photonic random texture. Additional interactions at the rear surface would be necessary for full randomization. Therefore, a two-stage randomization process such as the one in [41] should be considered for the modelling of scattering in thin film solar cells.

4.6 Conclusion

In this chapter, the Harvey-Shack SST has been introduced, and its different versions have been applied to the AID calculations of two types of surface textures intended for use in the solar industry.

The autocorrelation function (ACF) approach is suited for well-behaved surfaces and lends itself better to parametrization and PSDF averaging to reduce experimental uncertainties, but requires some statistical assumptions that are not always fulfilled. The equivalent and more direct phase screen (DPS) approach seems to be more general and robust in that regard, and performs as well for sample height profiles that are adequately representative of the real surfaces.

With regard to the choice of pupil function, the generalized Harvey-Shack (GHS) theory uses the correct phase accumulation term, which makes it truly non-paraxial in the far-field, and the extra computational cost can be handled by relative ease. The simpler, less computationally demanding original version (OHS) can still produce

adequate results for isotropic textured samples, in which the scattered power is mostly contained in angle ranges where the difference between the two phase-accumulation models is not too large.

Moreover, in contrast to the OHS model, the GHS model applied to scattering from air into an optically denser medium predict AID distributions concentrated to small polar angles, constrained by the existence of specific angles where no scattering occurs. Therefore, the GHS model predicts that ideal Lambertian scattering distribution (and therefore $4n^2$ Yablonovitch limit light trapping) cannot be achieved by a single pass through the front surface of a random photonic texture.

Comparisons of GHS implementations with independent angular measurements show remarkable general agreement. while also revealing two possible limitations of SST, which were examined in detail.

The first one consists of a regular decrease of wide angle scattering in rougher textures with small lateral features that could be explained by an effective decrease in height profile, due to the onset effective medium effects. This limitation of SST modelling could arguably point out to a physical limitation of achievable high angle scattering inside thin absorber materials using photonic surface texturing, since making steeper textures at the nanoscale will be less and less effective.

The second limitation of SST is that it concerns only primary interactions of incident light with the surface. An increase in scattering towards negative scatter angles at the expense of forward scattering, observed across all samples (especially for oblique incidence), has been experimentally linked to the presence of secondary interactions at the surface topography, that serve to redistribute part of the scattered power.

CHAPTER 5

INVESTIGATION OF NEAR-FIELD TERMS

"Nearly everything is really interesting if you go into it deeply enough."
Richard Feynman

5.1 Introduction

In the previous chapter, the Harvey-Shack SST, itself based on an approximation of the Rayleigh-Sommerfeld (RS) scalar diffraction integral, has been laid down and validated by comparing its results to far-field AID measurements. On the other hand, there have been numerous studies over the years to validate the applicability of RS diffraction integrals [86,87] to evaluate the fields in the near-field. Analytical solutions can be obtained only for a few simple cases, such as for a spherical wave incident on a circular aperture, where the source (or focal) point and observation point lie on the optical axis [93-95]. The validity of replacing the empty aperture with a thin phase object (considered as a zero-thickness phase shifting foil, as in Harvey-Shack surface modelling) is also investigated, albeit with simple, homogeneous phase apertures [95]. Approximations to the integral kernel of the full RS formulae are often used that make analytical approaches possible. Some of these, such as the Fresnel and Fraunhofer approximations are commonly known [96], while some are newly proposed [97], each with their specific applications and validity ranges.

For more complex apertures/scattering objects, numerical methods based on Fourier optics need to be employed. Most of these methods fall in two main categories: The RS convolution integral can be directly evaluated [98,99] in the spatial domain, by

calculating the FFT of both the pupil function and the impulse response of free space, then elementwise multiplying the resulting matrices, before calculating the inverse FFT of the result to obtain the field/complex amplitudes.

Alternatively, the angular spectrum of the plane waves [100,101] emanating from the aperture can be calculated in the spatial frequency domain by taking the FFT of the pupil function, which is then multiplied by the transfer function of free space, before calculating the inverse FFT of the result to obtain the field/complex amplitudes.

Note that both of the aforementioned methods calculate the complex amplitudes on a plane of observation some distance away from the aperture. On the other hand, the Harvey approach of Equation (5.1) purposes to evaluate the RS direct convolution integral, but on an observation hemisphere centered around the aperture using the reciprocal direction-cosine coordinates of the angular spectrum method. In this regard, it can be considered a middle ground better suited for situations where the angular distribution is important, such as in solar cells.

$$U(\alpha,\beta;\,\hat{r}) = \gamma\frac{e^{i2\pi\hat{r}}}{\hat{r}}\iint_{-\infty}^{+\infty} U_0(\hat{x}',\hat{y}';0)\left(\frac{1}{2\pi\hat{l}}-i\right)\frac{\hat{r}^2}{\hat{l}^2}e^{i2\pi\widehat{W}}e^{-i2\pi(\alpha\hat{x}'+\beta\hat{y}')}\,d\hat{x}'d\hat{y}' \tag{5.1}$$

In the past decade, OHS theory based models using far-field approximations of Equation (5.1) such as those presented in section 4.2 have been used to estimate the AID inside thin layers [42-50], even though the constant OHS pupil function does not predict the dips in transmission AID for scattering into an optically denser medium. These OHS theory based models have also been incorportated in multilayer device simulations for absorption and current enhancement calculation in solar cells and other optoelectronic devices [47,48].

Leaving the GHS theory pupil function consideration momentarily aside, is it justified to utilize the far-field approximation of the RS scalar diffraction integral to model the AID to within a distance close to the considered diffraction aperture (i.e.,

the AFM scan area)? For instance, Dominé, who introduced the OHS theory to the solar cell community, takes the practical applicability range of a partially approximated RS diffraction integral (Equation (5.1) without the near-field reactive *B* term, defined in section 5.2) at about $r > 3\lambda$ [43], but doesn't address the effect of the other terms neglected in the far-field. Moving closer to the aperture, is it justified to model the AID inside very thin active layers with a thickness of just a few wavelengths, or less?

As a step towards answering these questions, a modified version of the element-by-element reconstruction method, used for the nonparaxial GHS theory in the previous section, will be employed to calculate the near-aperture and near-field terms of the RS diffraction integral that are no longer negligible when the observation point is close to the aperture.

5.2 Revisiting near-field terms of the Rayleigh-Sommerfeld integral

Let us consider again the general form of the RS diffraction integral be evaluated over an observation hemisphere centered around the aperture, but corrected in Equation (5.2) to account for scattering into a medium of refractive index n_s:

$$U(\alpha,\beta;\,\hat{r}) = \gamma\frac{e^{i2\pi n_s\hat{r}}}{n_s\hat{r}} \times \iint_{-\infty}^{+\infty} U_0(\hat{x}',\hat{y}';0)\left(\frac{1}{2\pi n_s\hat{l}} - i\right)\frac{\hat{r}^2}{\hat{l}^2}e^{i2\pi n_s\widehat{W}}e^{-i2\pi n_s(\alpha\hat{x}'+\beta\hat{y}')}\,d\hat{x}'d\hat{y}' \tag{5.2}$$

The scaling effect of n_s on coordinates $(\hat{x},\hat{y})$ of the Fourier kernel is already taken care of in the discrete algorithm, where $\Delta\alpha = \Delta\beta = \lambda_0/(L\,n_s)$.

This expression contains the Fourier transform of the multiplication of four terms:

$$A = U_0(\hat{x}',\hat{y}';0) = e^{i2\pi(\gamma_i n_i \pm \gamma_s n_s)\,\hat{h}(\hat{x},\hat{y};0)} \tag{5.3}$$

$$B = \left(\frac{1}{2\pi n_s \hat{l}} - i\right)$$

$$C = \frac{\hat{r}^2}{\hat{l}^2}$$

$$D = e^{i2\pi n_s \widehat{W}} = e^{i2\pi n_s[(\hat{l}-\hat{r})+(\alpha\hat{x}'+\beta\hat{y}')]}$$

A is the random phase screen term, i.e. it corresponds to the optical phase acquired when light traverses the rough texture. *B* is composed of two terms: $-i$, which leads to the usual far-field radiative terms; and the $1/2\pi n_s \hat{l}$ term, which is the near-field [53,66], reactive term corresponding to evanescent waves. *C* acts like an amplitude-like geometric weighting term during the integration. *D* can be considered as a deterministic phase screen term due to the diffraction geometry. As will be seen in the examples below, in the near-aperture region this term has a fast oscillating argument. In fact, Harvey proceeds [52,53] to make the binomial expansion of $\hat{l}$ in terms of $(\hat{x}, \hat{y})$, and shows that $\widehat{W}$ can be written as a sum of constituent terms identified as conventional wavefront aberrations. Here I will take a numerical approach.

When the observation radius r is not much larger than the aperture size, the terms *C* and *D* are no longer negligible. Moreover, the evaluation of the *A* term should also change, because the angle term γ_s can no longer be considered constant across the aperture. When the observation radius r is no longer much larger than the wavelength, the term *B* also becomes non negligible. However, for any given r, it is possible to numerically calculate these terms. A geometric visualization of these terms is presented in Figure 5.1.

As in the previous section, the effect of the angle of incidence is accounted by shifting the center of the observation hemisphere in direction cosine space.

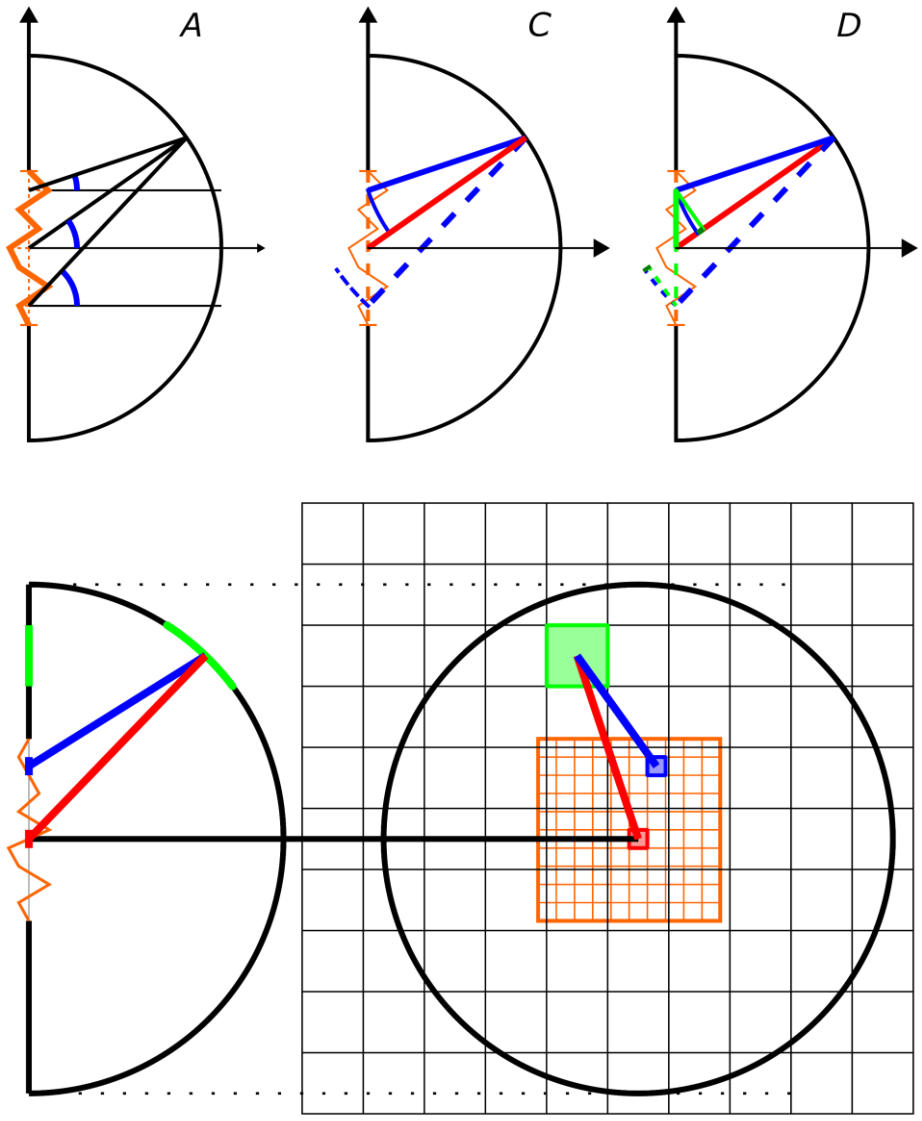

Figure 5.1. Top: Geometric visualization of near-field terms A, C and D. The $(\hat{l} - \hat{r}) + (\alpha\hat{x}' + \beta\hat{y}')$ quantity in term D corresponds to the small distance in bright green. Bottom: Geometric visualization of the direction cosine space (black) centered on the real, aperture space (orange), with distances $\hat{r}$ (red) and $\hat{l}$ (blue).

Because each of these terms depends on the scattering angle γ_s, the complex amplitude distribution $U(\alpha, \beta; \hat{r})$ and $I_{2D}(\alpha, \beta)$ cannot be obtained by a single Fourier transform operation, i.e. Equation (4.2) corresponds to a "two-parameter family" of Fourier transforms. But this is exactly the same difficulty faced by the

GHS theory in the far-field, and can be overcome by the same element-by-element reconstruction method. For each matrix element (green in Figure 5.1 Bottom) corresponding to a scatter angle inside the unit circle in direction cosine space, four NxN 2D screens corresponding to each term are calculated numerically by scanning the angle θ_s (for *A*) and distances $\hat{r}$ (for *C* and *D*), $\hat{l}$ (for *B*, *C* and *D*) and $\alpha\hat{x}' + \beta\hat{y}'$ (for *D*) across the aperture. In the resulting FFT transform after elementwise multiplication of the four terms, only the element corresponding to the correct scatter angle is retained.

The results of some $I_{1D}(\theta)$ calculations along the plane of incidence will now be presented for sample D, for three different observation hemisphere radii. However, it is no longer possible to use the previous azimuthal averaging algorithm, to recreate the equivalent of each valid scatter element (of the 2D hemipshere) on the 1D incidence plane. This is because, unlike the far-field isotropic random phase screen term used in the previous section, the four terms do not have circular symmetry around the central element. Therefore the AID is more noisy, being composed of just $1/\Delta\alpha$ elements, or 47 data points in the case of scattering into air.

5.2.1 Case 1: r=5000µm, n_i=1.87→n_s=1, θ_i=15.508° (θ_t=30°)

This large observation hemisphere radius is chosen to verify that the approach to calculate the near-field and near aperture terms converge with the previous far-field calculations. In Figure 5.2, the first 4 images show the modulus of the amplitude-like terms *B* and *C*, and the argument of the phase terms *A* and *D*. In these examples, these terms are illustrated at the scatter angle corresponding to matrix elements (p, q)=(100,100), which remain inside the shifted diffraction hemisphere, at a radial angle θ=38.9° and an azimuth angle φ=10.7°. The FFT result of the elementwise multiplication of these four terms in presented in 2D and 3D perspectives. The element-by-element reconstructed power distribution and the resulting AID match very well with previous far-field calculations, while the red line in the AID graph shows the angular measurement result.

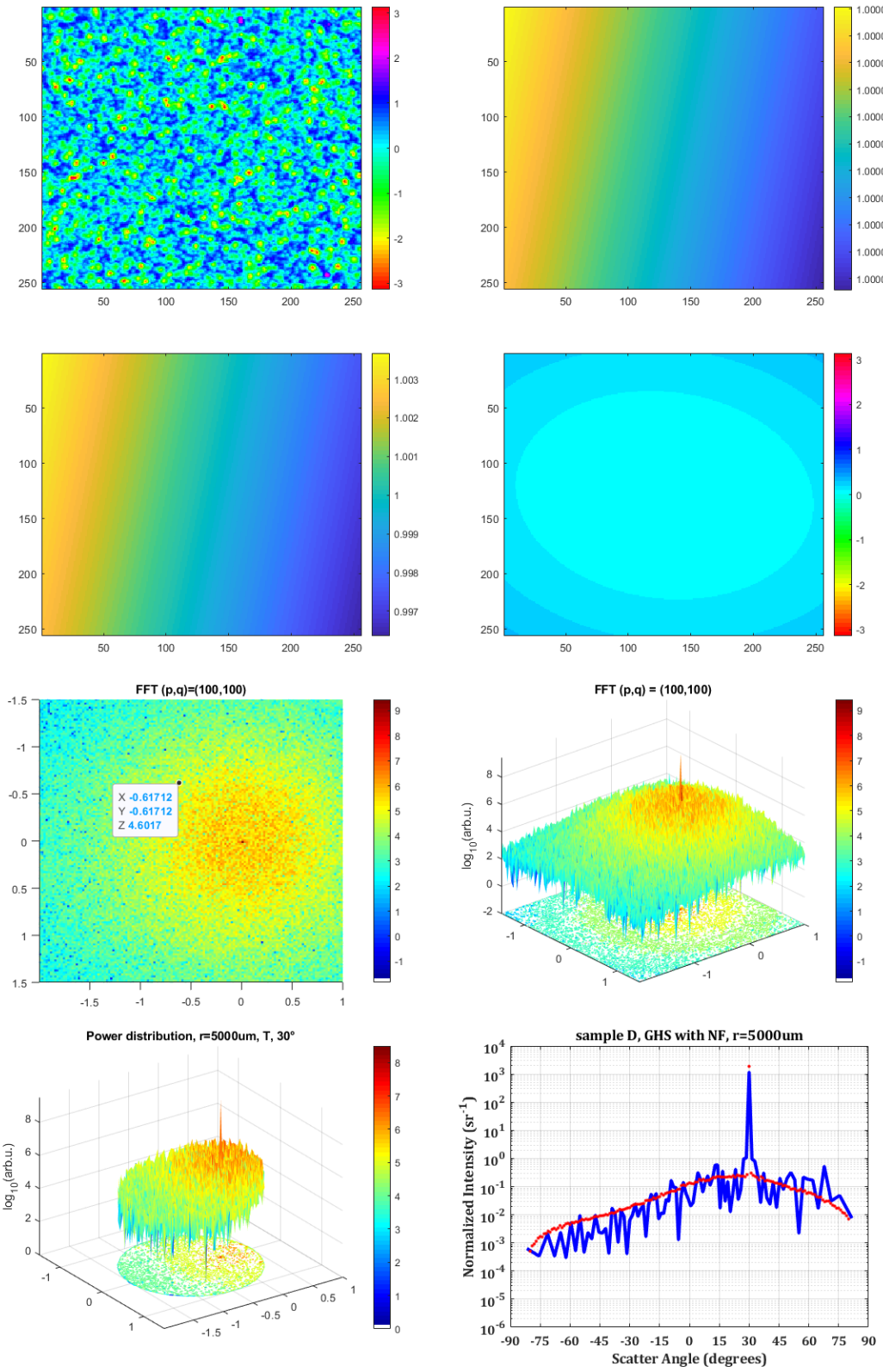

Figure 5.2. Select calculation steps for r=5000μm, θ_i=15.508°

5.2.2 Case 2: r=50μm, n_i=1.87→n_s=1, θ_i=15.508° (θ_t=30°)

In this example, the observation hemisphere radius becomes comparable to the aperture size, which is the AFM scan length of L=25μm. Figure 5.3a illustrates an on-scale representation of this diffraction geometry.

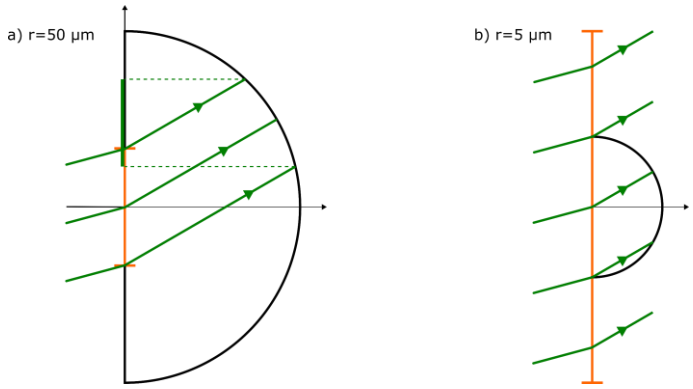

Figure 5.3. Diffraction geometries with a) r=50μm, b) r=5μm observation radii, under θ_i=15.508 incidence angle (θ_t=30°)

Figure 5.4 reproduces the previous calculation steps for r=50μm, with the four terms calculated for the scatter angle corresponding to the matrix element (p, q)=(100,100). As the radius decreases, near aperture terms *C* and *D* increasingly become non-negligible. On the FFT for this to the matrix element (p, q)=(100,100), and especially on the element-by-element reconstructed 2D power distribution, the image of the AFM scan area can clearly be seen on the observation hemisphere as a square projection.

Consequently, when the aperture size is not negligible, the 'angular intensity' distribution that is calculated by this routine can be interpreted as a convolution of the true angle spread function with the extent of the aperture.

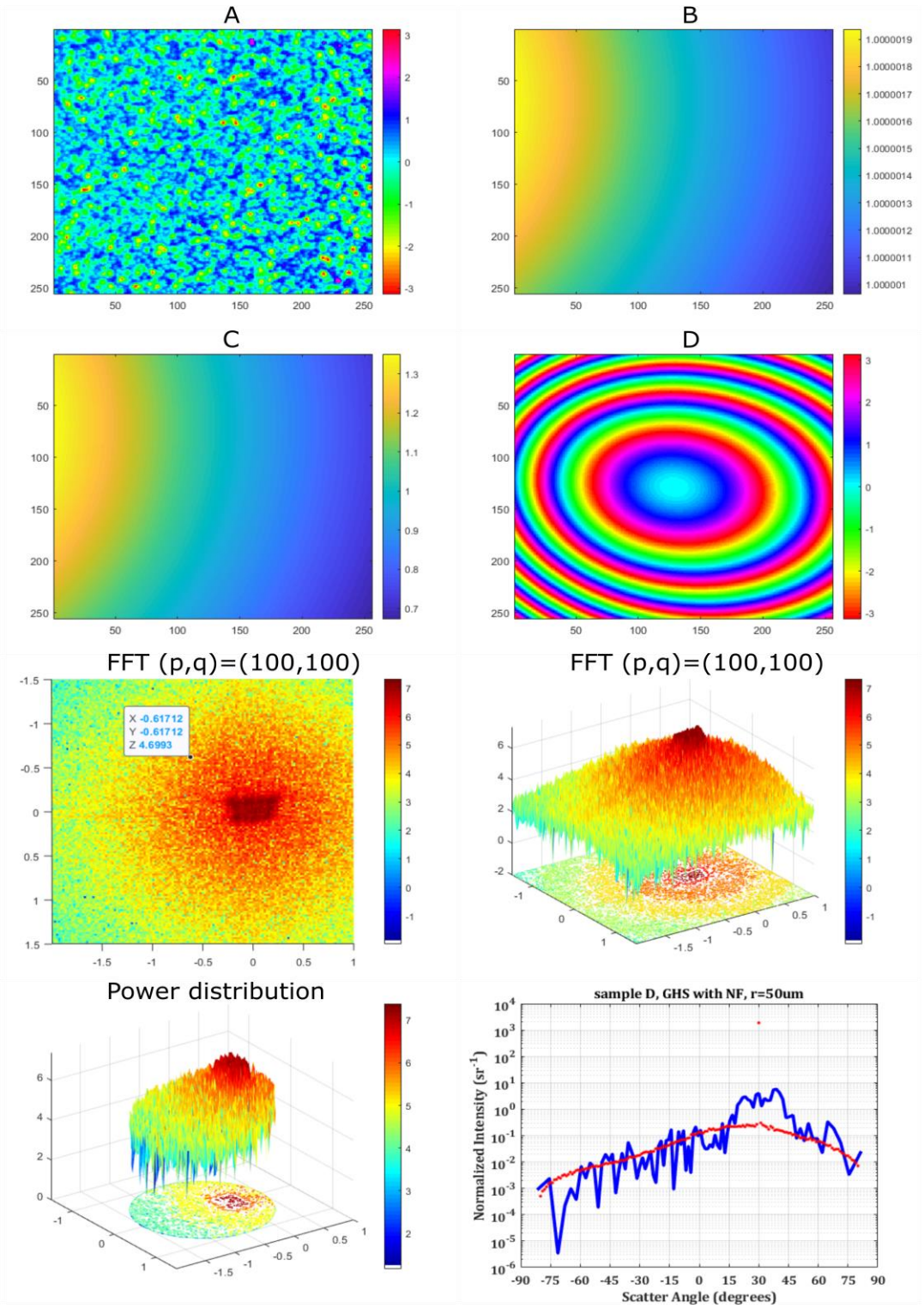

Figure 5.4. Select calculation steps for r=50μm, θ_i=15.508° (θ_t=30°)

5.2.3 Case 3: r=5µm, n_i=1→n_s=1.87, 15.508° (θ_t=30°)

In this example, the observation hemisphere radius becomes smaller than the aperture size of L=25µm. Figure 5.3b illustrates an on-scale representation of this diffraction geometry.

Figure 5.5 reproduces the previous calculation steps for r=5µm, with the four terms calculated for the scatter angle corresponding to the matrix element (p, q)=(100,100).

When the edges of the observation hemisphere gets close to the aperture, the weighting terms B and C become very high for the element (p, q) that is retained in the FFT. This leads to an increase in the 'angular power' and 'angular intensity' distributions towards higher scattering angles. This is expected from a physical point, since the distance from the scattering dipoles on the surface to the local observation point gets very small.

The power distribution starts to mirror the troughs and crests of the surface texture - phase object situated below. The algorithm described in Figure 5.1 only allows an observation hemisphere centered on the AFM image aperture. However, if the power distribution at different position on the aperture is required, it is possible to use a simple translation of the AFM image center to that another point. When this is done, the power distribution changes to mirror the local phase object around this new point.

However, even more than in the previous example, it is not correct anymore to interpret these results as an "angular distribution", because the incidence is not through a small aperture at the center of the hemisphere.

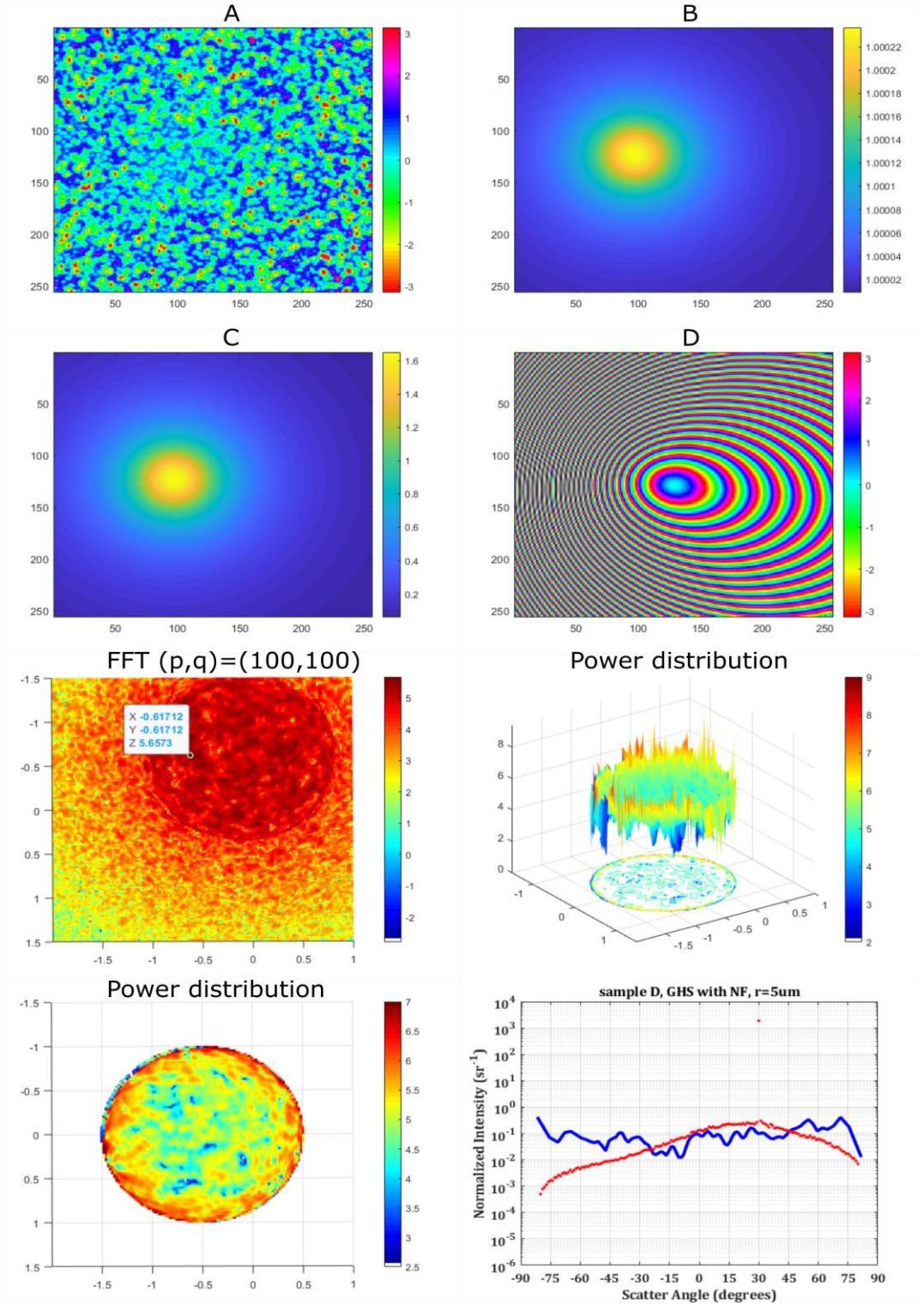

Figure 5.5. Select calculation steps for r=5μm, θ_i=15.508° (θ_t=30°)

5.2.4 Case 4: r=5 μm with window function, n_i=1.87→n_s=1, 15.508° (θ_t=30°)

If an angular distribution with respect to the polar angle is desired, e.g. to be used in an absorption enhancement calculation, it is possible to utilize a 'virtual aperture' or window function. Figure 5.6 presents such a window function that can be used to restrict the matrix terms that are going to affect the AID calculation.

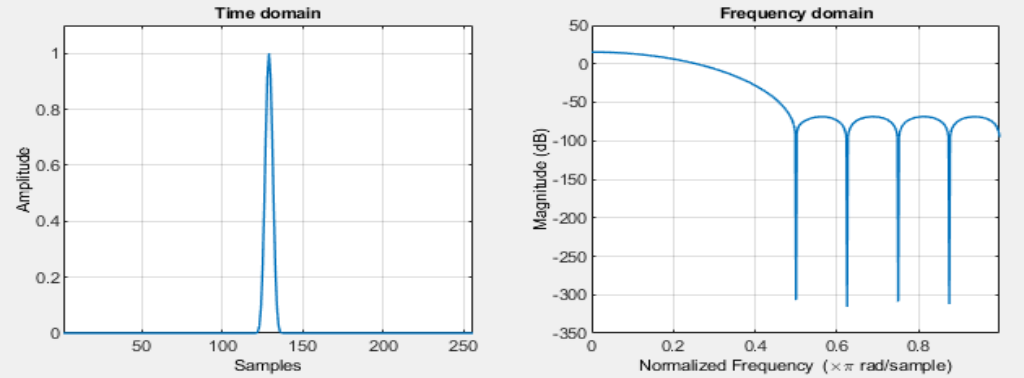

Figure 5.6. 2D Nuttall [n=16] window [102] placed at the center of an [N=256] square matrix. The rest of the matrix elements are filled with zeros.

Figure 5.7 reproduces the results of Figure 5.5 with the inclusion of this window function in each FFT operation. The increase in power towards the edges of the observation hemisphere is remedied. The intensity distribution result can be once again considered an "angular distribution". This AID is more similar to the far-field distribution, but without the non-diffracted peak. The power that is concentrated in the non-diffracted peak in the far-field seems to be distributed to a broad range of angles, and which also changes with the phase surface below if this latter is translated. This broadening in frequency space can be explained intuitively using Fourier optics arguments, by the narrowing of spatial coordinates from which diffraction occurs near the surface, when the observation hemisphere shrinks.

The downside to the use of a window function is that the matrix elements contributing to the result are constricted to those at the center of the aperture. The

decrease in the number of effective matrix elements would result a greater uncertainty in the frequency domain. This could partly explain the broadening of the AID around the peak. The window function could also introduce numerical artefacts such as FFT side lobes, whose effects could probably be seen in the placement of secondary peaks around the central one.

Both of these problems could be mitigated by using an AFM image with denser points per line, which in turn would allow a finer window function, at the cost of computational complexity.

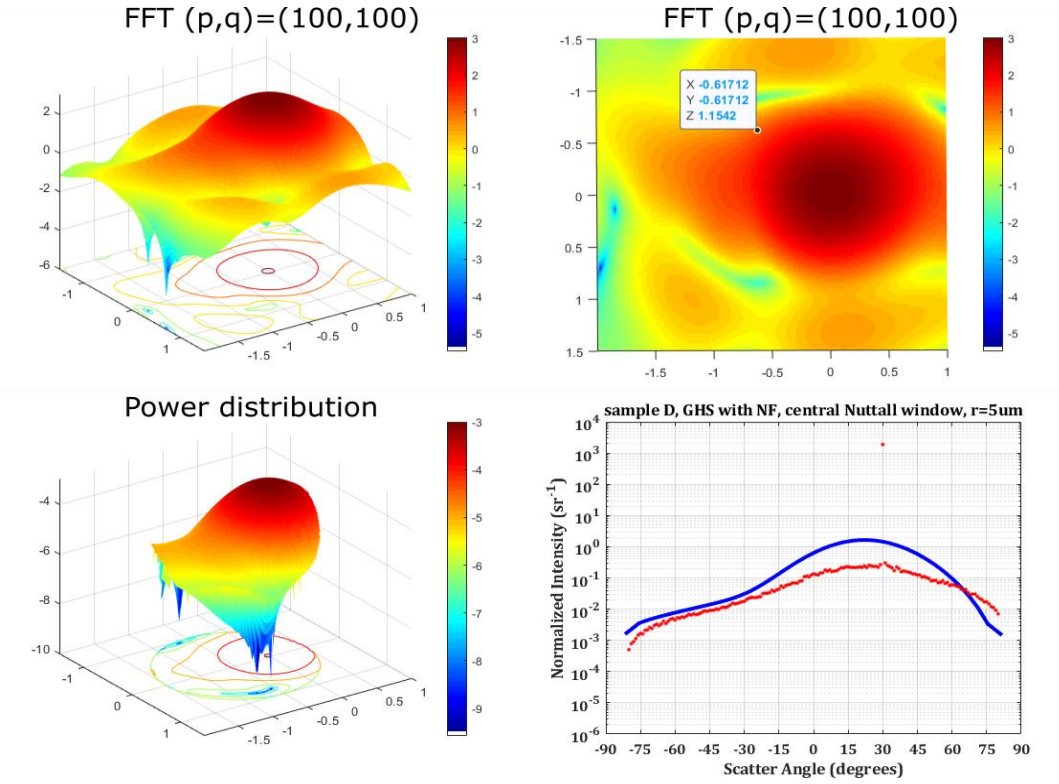

Figure 5.7. Results for r=5μm, θ_i=15.508°, using a central Nuttall window function

5.2.5 Case 5: r=5 μm with window function, n_i=1.87→n_s=1, θ_i=30° (θ_t=15.508°)

A similar calculation is performed for scattering into the optically denser medium, using the same central Nuttall window function, the results of which are presented

in Figure 5.8. The disappearance of scattering towards scatter angles satisfying the condition $\gamma_i n_i = \gamma_s n_s$ is clearly visible once again.

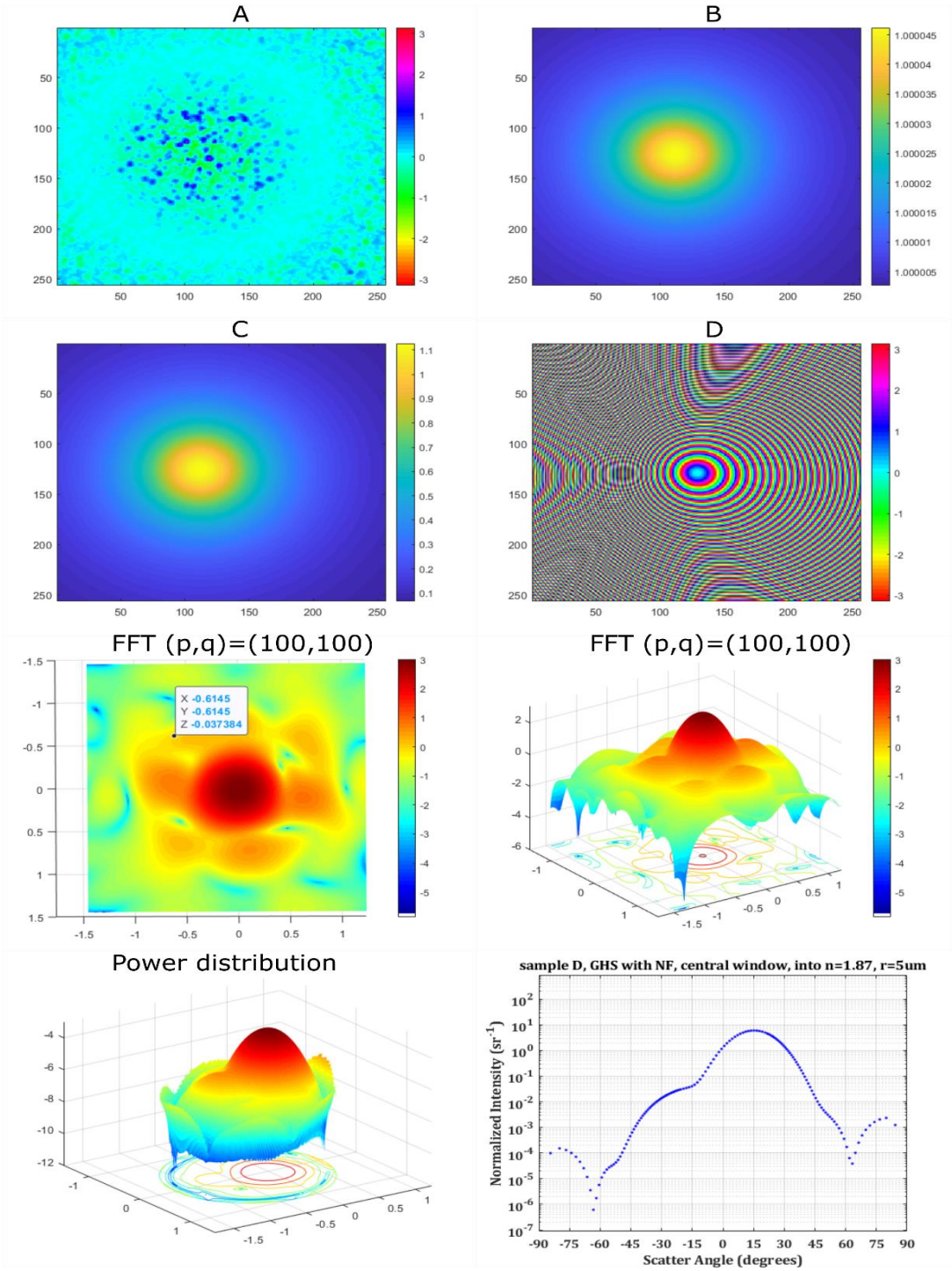

Figure 5.8. Results for r=5μm, θ_i=30°, using a central Nuttall window function

Similar calculations could be made for even smaller observation radii, where the near-field term B become more important. The use of well-selected window functions would be even more difficult but necessary to obtain true 'angular distributions' of intensity in those cases. However, the relationship between the electric and magnetic fields in the vicinity of the randomly textured surface, especially in the presence of a thin absorber medium, is likely to be very complex. How far close to the surface these SST based predictions remain accurate is another matter that should be investigated using rigorous electromagnetic simulations possibly supported by scanning near-field optical microscopy (SNOM) [33,103] characterization.

5.3 Total intensity distribution

Recall that TID representation was defined as a 2D AID integrated along the azimuthal φ coordinate, which corresponds to the total intensity scattered alongside equivalent polar angles θ_s.

The GHS theory algorithm used in this chapter to find non-azimuthally-averaged 2D AID involves the element-by-element FFT reconstruction step, performed for matrix elements corresponding to valid scatter angles inside a shifted observation hemisphere. The resulting normalized 2D power distribution is multiplied by the GHS normalization constant K_{norm}, and the value of each element is divided by the corresponding solid angle $\Delta\Omega_{\alpha,\beta} \cong \Delta\alpha\,\Delta\beta/\gamma$, where $\gamma = cos(sin^{-1}\, d_0)$, to obtain a radiant AID $I_{2D}(\alpha, \beta)$.

To obtain the $TID(\theta_s)$, these elements are sorted according to their radial distance in direction cosine space d_0, from the center of the hemisphere, Next, values of elements with identical radial distances are averaged. Each radial distance is associated with a thin ring area between that of its neighbours, except the first element (zenith direction) which is associated with a circular area surrounded by the first ring area. The intensity of each element is multiplied with its associated area:

this operation corresponds to a numerical integration along azimuthal (φ) coordinates. Figure 5.9 illustrates an example of such a TID calculation, made for the previous case of 30° incidence on sample D.

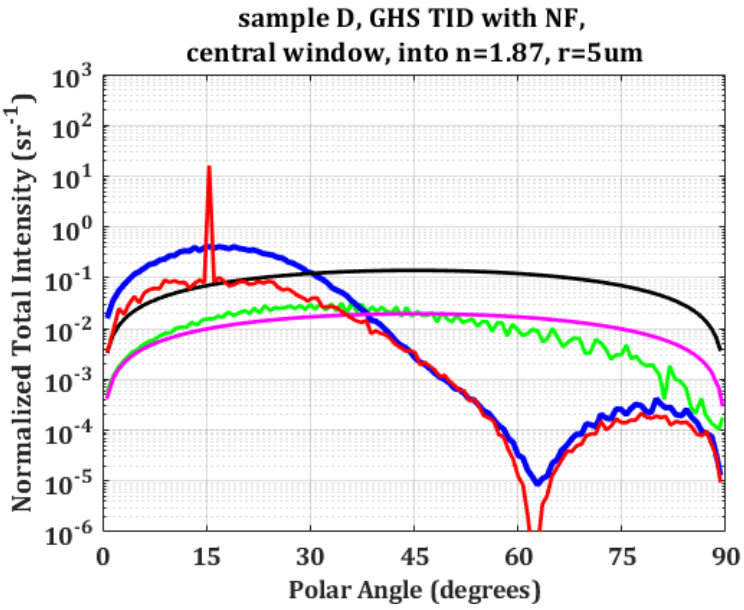

Figure 5.9. TID for sample D, with incidence angle θ_i=30°. (blue) and (green) show results respectively for transmission and reflection, for r=5μm, using a central Nuttall window function. (red) shows a TID for transmission calculated in the far-field. (black) and (pink) curves represent Lambertian distributions, calculated using Equation (2.9) and weighted by $f_{R,T}$, respectively for transmission and reflection.

It can be clearly seen that near the aperture (r=5μm), the intensity distribution is much broader until about 30°, whereas in the far-field it is concentrated in the non-diffracted peak.

However, the decrease of scattering towards scatter angles satisfying $\gamma_i n_i = \gamma_s n_s$ is clear in both cases. This reinforces one of the previous conclusions that this phenomenon, if experimentally verified, would constitute a serious theoretical limitation towards achieving $4n^2$ Yablonovitch limit light trapping, at least in a single pass, through a randomly textured photonic interface. The existence of dips in

scattering into an optically denser medium forces the TID away from the case of the ideal Lambertian distribution for most of high polar scatter angle range. This is the case even though the TID distribution for the coupled case in reflection is predicted to be almost completely Lambertian, which is confirmed by AID measurements in the far-field, from Figure 4.11.

5.4 Conclusion

A numerical method has been laid down to calculate the near-aperture and near-field terms of the RS scalar diffraction integral. These are terms that had been neglected so far in the solar cell community when using the SST to model the intensity distributions in thin film solar cells. This novel method has been applied to the scattering of light from a complex phase object such as a rough random surface texture.

The results show that, when the observation hemisphere approaches the surface profile, the aperture should be likewise restricted to a small region of the original surface profile by means of a virtual aperture. The AID results calculated under these conditions show a broadening of the main intensity component that forms a non-diffracted peak in the far-field. This can be explained, from a physical point of view, by the narrowing of spatial coordinates from which light is scattered near the surface, which causes a broadening of the angular distribution of light in the frequency space. The AID results also closely mirror the troughs and crests of the phase object below, as can be expected.

Another important feature is the continuous presence of the angle range with scattering dips when light is scattered into the optically denser medium. This phenomenon, if confirmed, would have negative consequences on the light trapping potential achievable by such random photonic textures, at least when the first pass through the absorber medium is concerned.

These results are given within the inaccuracies inherent in the scalar nature of the method, especially for applications to the very-near-field, where the coupling between the electric and magnetic fields is complex and cannot be ignored. An assertive validation of these results does require rigorous electromagnetic simulations over a large number of statistical realizations of a randomly textured surface, possibly supported by scanning near-field optical microscopy (SNOM) characterization.

While the main motivation of this thesis remains towards thin film solar cell applications, the computational method proposed in this section can in principle be applied to other geometries and problems, including the application of RS diffraction integral to an observation plane, similar to Equation (4.1), a given distance away from the aperture, as is usually done outside of the Harvey-Shack approach.

Compared to other numerical methods for near-field diffraction pattern calculation based on the direct evaluation of the RS convolution integral or the angular spectrum of plane waves method, this novel method should be computationally more intensive due to the large number of FFT operations, and especially due to the need to recalculate all four terms from scratch for each FFT. However, note that the recalculation of at least the *A* term cannot be dispensed with using more conventional methods (even for observation planes), because the phase object itself changes depending on the scatter angle (or the position on the observation plane).

CHAPTER 6

CONCLUSIONS AND FUTURE PROSPECTS

"The scepter, learning, physic must
All follow this, and come to dust."
Cymbeline, Shakespeare

In this thesis, I have set out to investigate the Harvey-Shack nonparaxial scalar diffraction theory applied to the scattering of light from rough dielectric surface textures intended for use in thin film solar cells as light trapping interfaces.

In order to approach this subject, an angular light intensity measurement instrument has been purpose-designed and built. It consists of a sample stage that can rotate to set an incident angle, and a detector arm that can revolve around the same center with high angular resolution, thus enabling operation both in reflection and transmission mode.

Harvey-Shack scalar surface scattering theory is a method that established itself in the modelling of thin film layers in the solar cell community. It is based on the Fourier transform of the optical phase light accumulates while traversing the rough surface texture to evaluate the far-field approximation of the Rayleigh-Sommerfeld diffraction integral, observed on a hemisphere centered around the sample aperture. Different versions of Harvey-Shack theory can be found in the literature. These were identified and implemented in computational algorithms that run on a personal computer.

Among these versions, the autocorrelation function (ACF) approach is suited for well-behaved surfaces and lends itself better to parametrization and averaging to

reduce experimental uncertainties, but requires some statistical assumptions that are not always fulfilled. The equivalent and more direct phase screen (DPS) approach seems to be more robust in that regard, and performs as well for sample height profiles that are adequately representative of the real surfaces.

With regard to the choice of the pupil function to be Fourier-transformed, the generalized Harvey-Shack (GHS) theory uses the correct phase accumulation term, which makes it truly non-paraxial in the far-field, and the extra computational cost can be handled by relative ease. The simpler, less computationally demanding original Harvey-Shack (OHS) theory can still produce adequate results for isotropic textured samples, in which the scattered power is mostly contained in angle ranges where the difference between the two phase-accumulation models is not too large.

Moreover, in contrast to the OHS model, the GHS model applied to scattering from air into an optically denser medium predicts angular intensity distributions concentrated to small polar angles, constrained by the existence of specific angles where no scattering occurs. Therefore, the GHS model predicts that ideal Lambertian scattering distribution (and therefore $4n^2$ Yablonovitch limit light trapping) cannot be achieved by a single pass through the front surface of a random photonic texture.

All of these results show remarkably good general fit to actual far-field intensity measurements, the GHS predictions being the more accurate. However, these comparisons also reveal two possible limitations of scalar scattering theory:

The first one consists of a regular decrease of wide angle scattering in rougher textures with small lateral features that could be explained by an effective decrease in height profile, which can be attributed to effective medium effects. This limitation of scalar scattering theory modelling could arguably point out to another physical limitation of achievable high angle scattering inside thin absorber materials using photonic surface texturing, since making steeper textures at the nanoscale will be less and less effective.

The second limitation of scalar scattering theory is that it concerns only primary interactions of incident light with the surface. An increase in scattering towards negative scatter angles at the expense of forward scattering, observed across all samples (especially for oblique incidence), has been experimentally linked to the presence of secondary interactions at the surface topography, that serve to redistribute part of the scattered power.

In addition, the terms of the near-aperture and near-field terms of the RS scalar diffraction integral were investigated using a novel modification to the GHS algorithm. These are the terms that were previously neglected in the solar cell community, but can be relevant to modelling the intensity distributions in thin film solar cells using the scalar scattering theory. This novel method has been applied to the scattering of light from a complex phase object such as a rough random surface texture.

The results show that, when the observation hemisphere approaches the surface profile, the aperture should be likewise restricted to a small region of the original surface profile by means of a virtual aperture. The angular intensity distribution results calculated under these conditions show a broadening of the main intensity component that forms a non-diffracted peak in the far-field. This can be explained, from a physical point of view, by the narrowing of spatial coordinates from which light is scattered near the surface, which causes a broadening of the angular distribution of light in the frequency space. The angular intensity distribution results also closely mirror the troughs and crests of the phase object below, as can be expected.

As a future prospect ensuing from this thesis, a validation of such near-field results can be attempted by using rigorous electromagnetic simulations or scanning near-field optical microscopy characterization. This near-field computational method could also in principle be applied to other geometries and problems, including the application of Rayleigh-Sommerfeld diffraction integral to an observation plane at a

given distance away from the aperture, as is usually done outside of the Harvey-Shack approach.

Furthermore, this dissertation focuses on s-polarized incident waves, whose effects are more easily modelled using such a scalar scattering theory. When p-polarized incident waves are used, or indeed when the observation plane is not the plane of incidence, more complicated polarization related effects will come at play. This is especially true in scatter in reflection, where depending on the angle of incidence, quasi-Brewster like angle ranges appear, with significant decrease in scattering. Remaining within the scope of scalar scattering theory, a modelling of these effects could be attempted by replacing the constant fresnel weighting coefficients that depend only on the incidence angle and used throughout this work; by a two-dimensional “polarization screen”, that would also depend on the polar and azimuthal locations of the scatter angle with respect to the incident angle.

REFERENCES

[1] M. Skolnik, Radar Handbook. New York: McGraw-Hill, 3rd ed., 2008.

[2] L. Tsang, G.T.J. Kong, and R. Shin, Theory of Microwave Remote Sensing. New York: Wiley-Interscience, 1st ed., 1985.

[3] I. Woodhouse, Introduction to Microwave Remote Sensing. Boca Raton: CRC Press Taylor&Francis, 2006.

[4] S. Liang, Comprehensive Remote Sensing. Amsterdam: Elsevier, 2017.

[5] H. Gong, Y. Shao, T. Zhang, L. Liu and Z. Gao, "Scattering mechanisms for the “Ear” feature of Lop Nur Lake Basin", Remote Sens., vol. 6, no. 5, pp. 4546-4562, 2014.

[6] M. Mangiameli, A. Candiano, G. Fargione, A. Gennaro and G. Mussumeci, "Multispectral satellite imagery processing to recognize the archaeological features: The NW part of Mount Etna (Sicily, Italy)", Math Meth Appl Sci., special issue, pp. 1-7, 2019.

[7] N. Atalan Çayırezmez, P. Ertepınar Kaymakçı and G. D. Summers, "Remote sensing at Kerkenes: Combining geophysical and other methods", Yerbilimleri, vol. 29, no. 2, pp. 87–100, 2008.

[8] J. C. Stover, Optical Scattering: Measurement and Analysis. Bellingham: SPIE Press, 3rd ed., 2012.

[9] J. E. Harvey, K. L. Lewotsky and A. Kotha, "Effects of surface scatter on the optical performance of x-ray synchrotron beam-line mirrors", Appl. Opt., vol. 34, no. 16, pp. 3024-3032, 1995.

[10] J. E. Harvey, N. Choi, A. Krywonos, G. L. Peterson and M. E. Bruner, "Image degradation due to scattering effects in two-mirror telescopes", Opt. Eng., vol. 49, no. 6, 063202, 2010.

[11] J. E. Harvey, N. Choi, S. Schroeder and A. Duparré, "Total integrated scatter from surfaces with arbitrary roughness, correlation widths, and incident angles", Opt. Eng., vol. 51, no. 1, 013402, 2012.

[12] R. P. Breault, "Chapter 38: Control of Stray Light". In M. Bass (Ed), Handbook of Optics. New York: McGraw-Hill, 1994.

[13] "N. Holzschuch and R. Pacanowski, ""A Two-Scale Microfacet Reflectance Model Combining Reflection and Diffraction"", ACM Trans. Graph., vol. 36, no. 4, pp. 12-23, 2017."

[14] P. Würfel, Physics of Solar Cells. Weinheim: Wiley-VCH Verlag GmbH&Co, 2009.

[15] E. Yablonovitch, "Statistical ray optics", J. Opt. Soc. Am., vol. 72, no. 7, pp. 899-907, 1982.

[16] H. W. Deckman, C. B. Roxlo and E. Yablonovitch, "Maximum statistical increase of optical absorption in textured semiconductor films", Opt. Lett., vol. 8, no. 9, pp. 491-493, 1983.

[17] National Renewable Energy Laboratory (NREL), "Reference Solar Spectral Irradiance: Air Mass 1.5", https://rredc.nrel.gov/solar//spectra/am1.5/, [Online; accessed 28.01.2020]

[18] M. A. Green and M. Keevers "Optical properties of intrinsic silicon at 300 K", Prog. Photovolt., vol. 3, no. 3, pp. 189-192, 1995.

[19] J. Nelson, The Physics of Solar Cells, p. 279 and 282. London: Imperial College Press, 2003.

[20] F.-J. Haug and C. Ballif, "Light management in thin film silicon solar cells", Energy Environ. Sci., vol. 8, no. 3, pp. 824-837, 2015.

[21] L. Zeng, Y. Yi, C. Hong, J. Liu, N. Feng, X. Duan, and L. C. Kimerling, "Efficiency enhancement in Si solar cells by textured photonic crystal back reflector", Appl. Phys. Lett., vol. 89, no. 11, 111111, 2006.

[22] Z. Yu, A. Raman and S. Fan, "Fundamental limit of nanophotonic light trapping in solar cells", Proc. Natl. Acad. Sci. U.S.A, vol. 107, no. 41, pp. 17491-17496, 2010.

[23] Z. Yu, A. Raman and S. Fan, "Nanophotonic light-trapping theory for solar cells", Appl. Phys. A, vol. 105, no. 2, pp 329-339, 2011.

[24] S. Mokkapati and K. R. Catchpole, "Nanophotonic light trapping in solar cells", J. Appl. Phys, vol. 102, no. 10, 101101, 2012.

[25] A. P. Amalathas and M. M Alkaisi, "Nanostructures for light trapping in thin film solar cells", Micromachines, vol. 10, no. 9, p. 619, 2019.

[26] F.-J. Haug, A. Naqavi and C. Ballif, "Diffraction and absorption enhancement from textured back reflectors of thin film solar cells", J. Appl. Phys., vol. 112, no. 2, 024516, 2012.

[27] M. Python, E. Vallat-Sauvain, J. Bailat, D. Domine, L. Fesquet, A. Shah and C. Ballif, "Relation between substrate surface morphology and microcrystalline silicon solar cell performance", J. Non-Cryst. Solids, vol. 354, no. 19-25, pp. 2258-2262 (2008).

[28] M. Zeman, R. A. C. M. M. van Swaaij, J. W. Metselaar and R. E. I. Schropp, "Optical modeling of a-Si:H solar cells with rough interfaces: Effect of back contact and interface roughness", J. Appl. Phys., vol. 88, no. 11, pp. 6436-6443, 2000.

[29] H. Stiebig, T. Brammer, T. Repmann, O. Kluth, N. Senoussaoui, A. Lambertz and H. Wagner, “Light scattering in microcrystalline silicon thin-film solar cells”, Proc. 16th EU-PVSEC Glasgow, pp. 549-552, 2000.

[30] J. Krč, M. Zeman, F. Smole and M. Topič, "Optical modeling of a-Si:H solar cells deposited on textured glass/SnO2 substrates", J. Appl. Phys., vol. 92, no. 2, pp. 749-755, 2002.

[31] J. Krc, F. Smole and M. Topič, "Analysis of Light Scattering in amorphous Si:H solar cells by a one-dimensional semi-coherent optical model", Prog. Photovolt: Res. Appl., vol. 11, no. 1, pp. 15-26 (2003).

[32] K. Jäger and M. Zeman, "A scattering model for surface-textured thin films", Appl. Phys. Lett., vol. 95, no. 17, 171108, 2009.

[33] C. Rockstuhl, F. Lederer, K. Bittkau and R. Carius, "Light localization at randomly textured surfaces for solar-cell applications", Appl. Phys. Lett., vol. 91, no. 17, 171104, 2007.

[34] C. Rockstuhl, S. Fahr, F. Lederer, K. Bittkau, T. Beckers and R. Carius, "Local versus global absorption in thin-film solar cells with randomly textured surfaces", Appl. Phys. Lett., vol. 93, no. 6, 061105, 2008.

[35] C. Rockstuhl, S. Fahr, K. Bittkau, T. Beckers, R. Carius, F.-J. Haug, T. Söderström, C. Ballif, and F. Lederer, "Comparison and optimization of randomly textured surfaces in thin-film solar cells", Opt. Express, vol. 18, no. S3, A335-A342, 2010.

[36] S. C. Kim, "Simulation of rough surface of CIGS (CuInGaSe) solar cell by RCWA (rigorous coupled wave analysis) considering the incoherency of light", J. Opt. Soc. Korea, vol. 18, no. 2, pp. 180-183, 2014.

[37] M. Sever, J. Krč, A. Čampa, and M. Topič, "Rigorous modelling of light scattering in solar cells based on finite element method and Huygens' expansion", Opt. Express, vol. 23, no. 24, pp. A1549-A1563, 2015.

[38] K. Bittkau, M. Schulte, M. Klein, T. Beckers and R. Carius, "Modeling of light scattering properties from surface profile in thin-film solar cells by Fourier transform techniques", Thin Solid Films, vol. 519, no. 19, pp. 6538-6543, 2011.

[39] C. Battaglia, M. Boccard, F.-J. Haug and C. Ballif, "Light trapping in solar cells: When does a Lambertian scatterer scatter Lambertianly?", J. Appl. Phys., vol. 112, no. 9, 094504, 2012.

[40] C. Battaglia, C.-M. Hsu, K. Söderström, J. Escarré , F.-J. Haug, M. Charrière, M. Boccard, M. Despeisse, D. T. L. Alexander, M. Cantoni, Y. Cui and C. Ballif, "Light trapping in solar cells: can periodic beat random?", ACS Nano., vol. 6, no. 3, pp. 2790-2797, 2012.

[41] M. Boccard, C. Battaglia, F.-J. Haug, M. Despeisse and C. Ballif, "Light trapping in solar cells: Analytical modeling", Appl. Phys. Lett., vol. 101, no.15, 151105, 2012.

[42] D. Dominé, F.-J. Haug, C. Battaglia and C. Ballif, "Modeling of light scattering from micro- and nanotextured surfaces", J. Appl. Phys., vol. 107, no. 4, 044504, 2010.

[43] D. Dominé, The Role of Front Electrodes and Intermediate Reflectors in The Optoelectronic Properties of High-Efficiency Micromorph Solar Cells (Ph.D. Dissertation, Université de Neuchâtel), 2009.

[44] K. Jäger, M. Fischer, R. A. C. M. M. van Swaaij and M. Zeman, "A scattering model for nano-textured interface and its application in optoelectrical simulations of thin film solar cells", J. Appl. Phys., vol. 111, no. 8, 083108, 2012.

[45] O. Isabella, Light management in thin-film silicon solar cells (Ph.D. Dissertation, Delft University of Technology), 2013.

[46] K. Jäger, On the scalar scattering theory for thin-film solar cells (Ph.D. Dissertation, Delft University of Technology), 2012.

[47] T. Lanz, B. Ruhstaller, C. Battaglia, and C. Ballif, "Extended light scattering model incorporating coherence for thin-film silicon solar cells", J. Appl. Phys., vol. 110, no. 3, 033111, 2011.

[48] T. Lanz, K. Lapagna, S. Altazin, M. Boccard, F.-J. Haug, C. Ballif and B. Ruhstaller, "Light trapping in solar cells: Numerical modeling with measured surface textures", Opt. Express, vol. 23, no. 11, pp. A540-A547, 2015.

[49] N. Sahraei, S. Venkataraj, A. G. Aberle and M. Peters, "Optimum feature size of randomly textured glass substrates for maximum scattering inside thin-film silicon solar cells", Proc. SPIE, vol. 8981, Physics, Simulation, and Photonic Engineering of Photovoltaic Devices III, 89811D, 2014.

[50] N. Sahraei, K. Forberich, S. Venkataraj, A. G. Aberle, and M. Peters, "Analytical solution for haze values of aluminium-induced texture (AIT) glass superstrates for a-Si:H solar cells", Opt. Express, vol. 22, no. S1, pp. A53-A67, 2014.

[51] F.-J. Haug, M. Bräuninger and C. Ballif, "Fourier light scattering model for treating textures deeper than the wavelength", Opt. Express, vol. 25, no. 4, pp. A14-A22, 2017.

[52] J. E. Harvey, Light Scattering Characteristics of Optical Surfaces (Ph.D. Dissertation, University of Arizona), 1976.

[53] J. E. Harvey and R. V. Shack, "Aberrations of diffracted wave fields", Appl. Opt., vol. 17, no. 18, pp. 3003-3009, 1978.

[54] J. E. Harvey, "A Fourier Treatment of near-field scalar diffraction theory", Am. J. Phys., vol. 47, no. 11, pp. 974-980, 1979.

[55] J. E. Harvey, C. L. Vernold, A. Krywonos, and P. L. Thompson, "Diffracted radiance: a fundamental quantity in nonparaxial scalar diffraction theory", Appl. Opt., vol. 38, no. 31, pp. 6469-6481, 1999.

[56] J. E. Harvey, A. Krywonos and D. Bogunovic, "Nonparaxial scalar treatment of sinusoidal phase gratings", J. Opt. Soc. Am. A, vol. 23, no. 4, pp. 858-865, 2006.

[57] J. E. Harvey, N. Choi and A. Krywonos, "Scattering from moderately rough interfaces between two arbitrary media", Proc. SPIE, vol. 7794, Optical System Contamination: Effects, Measurements, and Control, 77940V, 2010.

[58] S. Schröder, A. Duparré, L. Coriand, A. Tünnermann, D. H. Penalver and J. E. Harvey, "Modeling of light scattering in different regimes of surface roughness", Opt. Express, vol. 19, no. 10, pp. 9820-9835, 2011.

[59] A. Krywonos, J. E. Harvey and N. Choi, "Linear systems formulation of scattering theory for rough surfaces with arbitrary incident and scattering angles", J. Opt. Soc. Am. A, vol. 28, no. 6, pp. 1121-1138, 2011.

[60] A. Krywonos, Predicting Surface Scatter Using A Linear Systems Formulation of Non-paraxial Scalar Diffraction (Ph.D. Dissertation, University of Central Florida), 2006.

[61] D. Nečas and P. Klapetek, "Gwyddion: an open-source software for SPM data analysis", Cent. Eur. J. Phys., vol. 10, no. 1, pp. 181-188, 2012.

[62] H. Cui, P. J. Gress, P. R. Campbell and M. Green, "Developments in the aluminium induced texturing (AIT) glass process", Glass Technol. Part A, vol. 53, no. 4, pp. 158-165, 2012.

[63] M. Ünal, H. Nasser, M. Günöven, I. Sökmen, A. Tankut and R. Turan, "Effect of aluminum thickness and etching time of aluminum induced texturing process on soda lime glass substrates for thin solar cell applications", Phys. Status Solidi C, vol. 12, no. 9-11, pp. 1201-1205, 2015.

[64] M. Ünal, A. Tankut, S. Canlı and R. Turan, "Near-unity haze by aluminum induced glass texturing: structural evolution of Al/glass interface and its impact on texturing", Opt. Mater. Express, vol. 7, no. 9, pp. 3051-3064, 2017.

[65] H. Nasser, E. Özkol, A. Bek and R. Turan, "High haze nature of textured Al:ZnO with Ag nanoparticles for light management in thin film solar cells", Opt. Mater. Express, vol. 5, no. 5, pp. 932-942, 2015.

[66] R. R. McLeod and K. H. Wagner, "Vector Fourier optics of anisotropic materials", Adv. Opt. Photon., vol. 6, no. 4, pp. 368-412, 2014.

[67] S. O. Rice, "Reflection of electromagnetic wave by slightly rough surfaces", Comm. Pure Appl. Math., vol. 4, no. 2-3, pp. 351-378, 1951.

[68] J. M. Elson and J. M. Bennett, "Vector Scattering Theory", Opt. Eng., vol. 18, no. 2, pp. 116-124, 1979.

[69] E. L. Church, and J. M. Zavada, "Residual surface roughness of diamond-turned optics,", Appl. Opt., vol. 14, pp. 1788-1795, 1975.

[70] E. L. Church, H. A. Jenkinson and J. M. Zavada, "Measurement of the finish of diamond-turned metal surfaces by differential light scattering,", Opt. Eng., vol. 16, no. 4, pp. 360-374, 1977.

[71] E. L. Church, H. A. Jenkinson and J. M. Zavada, "Relationship between surface scattering and microtopographic features", Opt. Eng., vol. 18, no. 2, pp. 125-136, 1979.

[72] P. Beckmann and A. Spizzichino, The Scattering of Electromagnetic Waves from Rough Surfaces. New York: Pergamon, 1963.

[73] G.C. Brown, V. Celli, M.Haller and A.Marvin, "Vector theory of light scattering from a rough surface: Unitary and reciprocal expansions", Surf. Sci., vol. 136, no. 2-3, pp. 381-397, 1984.

[74] A. R. McGurn, A. A. Maradudin, and V. Celli, "Localization effects in the scattering of light from a randomly rough grating", Phys. Rev. B Condens. Matter., vol. 31, no. 8, pp. 4866-4871, 1985.

[75] J.J. Greffet, "Scattering of electromagnetic waves by rough dielectric surfaces", Phys. Rev. B Condens. Matter., vol. 37, no. 11, pp. 6436-6441, 1988.

[76] A. Soubret, G. Berginc, and C. Bourrely, "Application of reduced Rayleigh equations to electromagnetic wave scattering by two-dimensional randomly rough surfaces", Phys. Rev. B, vol. 63, no. 24, 245411, 2001.

[77] I. Simonsen, Å. Larsen, E. Andreassen, E. Ommundsen, and K. Nord-Varhaug, "Haze of surface random systems: An approximate analytic approach", Phys. Rev. A, vol. 79, no. 6, 063813, 2009.

[78] J.-P. Banon, Ø. S. Hetland, and I. Simonsen, "Physics of polarized light scattering from weakly rough dielectric surfaces: Yoneda and Brewster scattering phenomena", Phys. Rev. A, vol. 99, no. 2, 023834, 2019.

[79] C. K. Carniglia, "Scalar Scattering Theory for Multilayer Optical Coatings", Opt. Eng., vol. 18, no. 2, pp. 104-115, 1979.

[80] H. E. Bennett, J. O. Porteus, "Relation between surface roughness and specular reflectance at normal incidence", J. Opt. Soc. Am., vol. 51, no. 2, pp. 123-129, 1961.

[81] I. Simonsen, A. A. Maradudin, and T. A. Leskova, "Scattering of electromagnetic waves from two-dimensional randomly rough perfectly conducting surfaces: The full angular intensity distribution", Phys. Rev. A, vol. 81, no. 1, 013806, 2010.

[82] T. Nordam, P. A. Letnes and I. Simonsen, "Numerical simulations of scattering of light from two-dimensional rough surfaces using the reduced Rayleigh equation", Front. Phys., vol. 1, (2013).

[83] P. A. Letnes, A. A. Maradudin, T. Nordam, and I. Simonsen, "Calculation of the Mueller matrix for scattering of light from two-dimensional rough surfaces", Phys. Rev. A, vol. 86, no 3, 031803, 2012.

[84] Ø. S. Hetland, A. A. Maradudin, T. Nordam, and I. Simonsen, "Numerical studies of the scattering of light from a two-dimensional randomly rough interface between two dielectric media", Phys. Rev. A, vol. 93, no. 5, 053819, 2016.

[85] Ø. S. Hetland, A. A. Maradudin, T. Nordam, P. A. Letnes, and I. Simonsen, "Numerical studies of the transmission of light through a two-dimensional randomly rough interface", Phys. Rev. A, vol. 95, no 4, 043808, 2017.

[86] Lord Rayleigh, "On the passage of waves through apertures in plane screens, and allied problems", Philos. Mag., vol. 43, no. 263, pp. 259-272, 1897.

[87] A. Sommerfeld, "Zur mathematischen Theorie der Beugungsercheinungen", Nachr. Kgl.Wiss. Göttingen, vol. 4, pp. 338-342, 1894.

[88] J. W. Goodman, Introduction to Fourier Optics. Englewood: Roberts & Company Publishers, 3rd ed., 2004.

[89] A. Papoulis, Probability, Random Variables, and Stochastic Processes. New York: McGraw-Hill, 1965.

[90] A. Duparré, J. Ferré-Borrull, S. Gliech, G. Notni, J. Steinert and J. M. Bennett, "Surface characterization techniques for determining the root-mean-square roughness and power spectral densities of optical components", Appl. Opt., vol. 41, no. 1, pp. 154-171, 2002.

[91] J. Ferré-Borrull, J. Steinert and A. Duparré, "Extending the capabilities of scanning probe microscopy for microroughness analysis in surface engineering", Surf. Interface Anal., vol. 33, no. 2, pp. 92-95, 2002.

[92] A. K. Gonzalez-Alcalde, J.-P. Banon, Ø. S. Hetland, A. A. Maradudin, E. R. Méndez, T. Nordam and I. Simonsen, "Experimental and numerical studies of the scattering of light from a two-dimensional randomly rough interface in the presence of total internal reflection: Optical Yoneda peaks", Opt. Express, vol. 24, no.23, pp. 25995-26005, 2016.

[93] E. Wolf and E. W. Marchand, "Comparison of the Kirchhoff and the Rayleigh–Sommerfeld Theories of Diffraction at an Aperture", J. Opt. Soc. Am., vol. 54, no. 5, pp. 587-594, 1964.

[94] J. C. Heurtley, "Scalar Rayleigh–Sommerfeld and Kirchhoff diffraction integrals: A comparison of exact evaluations for axial points*", J. Opt. Soc. Am., vol. 63, no, 8, pp. 1003-1008, 1973.

[95] M. Totzeck, "Validity of the scalar Kirchhoff and Rayleigh-Sommerfeld diffraction theories in the near field of small phase objects", J. Opt. Soc. Am. A, vol. 8, no. 1, pp. 27-32, 1991.

[96] G. D. Gillen and S. Guha, "Modeling and propagation of near-field diffraction patterns: A more complete approach", Am. J. Phys., vol. 72, no. 9, pp. 1195-1201, 2004.

[97] N. A. Ochoa, "Alternative approach to evaluate the Rayleigh-Sommerfeld diffraction integrals using tilted spherical waves", Opt. Express, vol. 25, no. 10, pp. 12008-12019, 2017.

[98] F. Shen and A. Wang, "Fast-Fourier-transform based numerical integration method for the Rayleigh-Sommerfeld diffraction formula", Appl. Opt., vol. 45, no. 6, pp. 1102-1110, 2006.

[99] S. Wang, Z. Li, J. Wu and Z. Wang, "Accelerated near-field algorithm of sparse apertures by non-uniform fast Fourier transform", Opt. Express, vol. 27, no. 14, pp. 19102-19118, 2019.

[100] A. Carbajal-Dominguez, J.B. Arroyo, J.E. Gomez Correa and G.M. Niconoff, "Numerical calculation of near field scalar diffraction using angular spectrum of plane waves theory and FFT", Rev. Mex. de Fis., vol. 56, no. 2, pp. 159-164, 2010.

[101] C. J. R. Sheppard, J. Lin and S. S. Kou, "Rayleigh–Sommerfeld diffraction formula in k space", J. Opt. Soc. Am. A, vol. 30, no. 6, pp. 1180-1183, 2013.

[102] K. M. M. Prabhu, Window functions and their applications in signal processing. Boca Raton: CRC Press Taylor&Francis, 2014.

[103] A. Bek, Apertureless SNOM: A New Tool for Nano-Optics (Ph.D. Dissertation, École Polytechnique Fédérale de Lausanne), 2004.

APPENDICES

"Hic sunt dracones."

A. Measurement calibrations and corrections

A.1 Intensity measurement calibrations

As explained in the experimental section 3.2, all experimental scatter measurements were performed using a 3 mm diameter diffuser film on the detector arm in front of the 1 mm core diameter optical fiber. To obtain the normalized AID, the diffuse signal measured at scatter angles is divided by the incident beam signal (laser beam measured directly by the same collector without a sample), and by the constant detector solid angle.

The use of this diffuser disk has the advantage of spatially averaging the signal over a larger collection area, resulting in a smoother measured signal, as illustrated in Figure A.1.

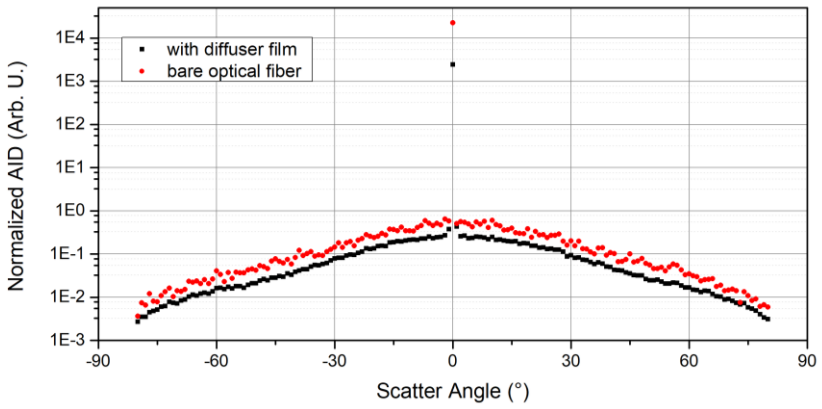

Figure A.1. Angular measurements for normal incidence transmission for sample D, with and without a diffuser film in front of the optical fiber. The scatter signal has been normalized with the incident signal and the larger (film) collector solid angle.

The alternative option of using a lens to focus the scattered light onto the optical fiber core would require a precise alignment which would be difficult to maintain in practical conditions. It would also lead to a larger collector footprint, blocking the incident light over a larger range of incident angles in reflection.

However, the coupling of light from a 3mm diffuser disk to a 1mm fiber core situated at a distance of few millimeters does not happen without losses. These coupling losses would not affect the intensity level if they are identical for a relatively homogeneous, diffuse scatter signal and the direct laser beam signal. However, as illustrated in Figure A.2, coupling losses are clearly not identical for light incident relatively homogeneously across the diffuser film area and concentrated at its center.

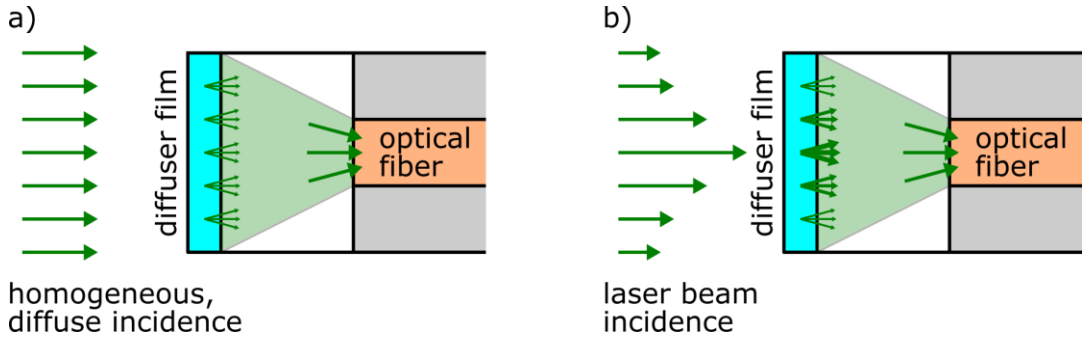

Figure A.2. Coupling losses for a) relatively homogeneous diffuse incident light and b) direct laser beam aligned to the center of the diffuser film.

Therefore, the case with the diffuse film has to be calibrated with respect to the case with a bare optical fiber. This can be accomplished by dividing the optical coupling losses into elementary quantities that can be measured. The calibration factor to adjust the diffuse (non-direct-beam) signal, measured with a diffuser film (compared to a signal measured without diffuser film, would be:

$$\frac{\text{signal,bare,diffuse}}{\text{signal,film,diffuse}} = \frac{\text{direct power collection ratio} \times \text{geometric collection mismatch} \times \text{solid angle ratio}}{\text{diffuse power collection ratio}}$$

$$\frac{\text{signal, bare, diffuse}}{\text{signal, film, diffuse}} = \frac{\frac{\text{direct power, film}}{\text{direct power, bare}} \times \frac{\text{power collected, bare}}{\text{power collected, detector.}} \times \frac{\text{solid A, film}}{\text{solid A, bare}}}{\frac{\text{diffuse power, film}}{\text{diffuse power, bare}}}$$

The peak power collection ratio is the ratio of the signal measured with the laser beam aligned to the center of the diffuser film in the position illustrated in Figure A.2b, to the signal measured with the laser beam aligned to the center of the optical fiber (with the diffuser film placed directly on the fiber to account for film reflectance). After numerous measurements, this ratio is estimated to be (0.20 ±2.7e-2).

The geometric collection mismatch results from the fact that the laser beam has a Gaussian beam width ω_0 of about 1.45 mm. Therefore, the bare optical fiber core of 1 mm diameter cannot collect all of the laser beam power. The power contained within a radius of $\mathrm{r_{fiber}} = 0.5$ mm from the Gaussian beam center is:

$$\frac{\mathrm{P(r_{fiber})}}{\mathrm{P_\infty}} = 1 - \exp\left(\frac{-2 * \mathrm{r_{fiber}}^2}{{\omega_0}^2}\right)$$

After numerous measurements of beam width, the geometric collection mismatch is estimated to be (0.61 ±3.7e-3).

The solid angle ratio is the ratio of the solid angles subtended by the 3 mm diameter diffuser film placed at 242 mm from the aperture center, versus the 1 mm bare optical fiber core placed at 244 mm, giving a ratio of 9.15. Uncertainties related to distances are neglected.

The diffuse power collection ratio is estimated similarly to the direct power collection ratio but using a diffuse light source such as a halogen lamp. After numerous measurements, it is estimated to be (0.86 ±3.7e-2).

$$\frac{\text{signal, bare, diffuse}}{\text{signal, film, diffuse}} = \frac{(0.20 \pm 2.7\text{e-}2) \times (0.61 \pm 3.7\text{e-}3) \times 9.15}{(0.86 \pm 3.7\text{e-}2)} = (1.29 \pm 1.39\text{e-}1)$$

This is a relation of the type $f(x_1, x_2, x_3) = c.x_1.x_2.x_3$. The standard deviation σ_{cal} for the overall calibration factor has been calculated by propagating the uncertainties $\sigma_{1,2,3}$ of the three multiplicative factors according to:

$$\sigma_{cal}{}^2 = c^2.(\overline{x_1}.\sigma_2{}^2.\sigma_3{}^2 + \overline{x_2}.\sigma_1{}^2.\sigma_3{}^2 + \overline{x_3}.\sigma_1{}^2.\sigma_2{}^2)$$

This calibration factor is applied to all non-direct-beam scatter measurements. The calibration factor concerning the direct-beam reduces simply to the geometric collection mismatch factor, or (0.61 ±3.7e-3).

A.2 Peak signal level corrections to account for lock-in time constant

The angular light scattering scans have been generally performed using a lock-in time constant of 100 ms, which is enough to follow the signal level across the diffuse angle range. However, during the measurement of the direct beam, the signal level changes by several orders of magnitude in a very short time, and for the corresponding data point the lock-in time constant is usually not fast enough to reach correct level by the time the measurement is taken. The resulting errors are illustrated in Figure A.3.

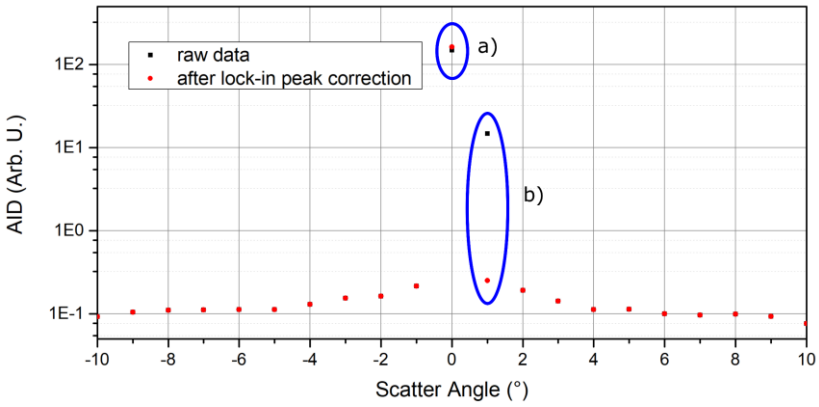

Figure A.3. Lock-in measurement error and its correction. The measurement is not fast enough to a) increase to and b) decrease to the correct signal level.

These errors can be remedied using the following procedure presented in Figure A.4. Raw data points are indicated with circles. Base points B1 and B2 correspond to the signal level just before and after the peak. B2 can be constructed using the data point after it and the ratio leading to the first base point B1. H is the raw data point corresponding to the peak, and it is underestimated. L is the raw data point after the peak, and it is overestimated. X corresponds to the true peak signal level.

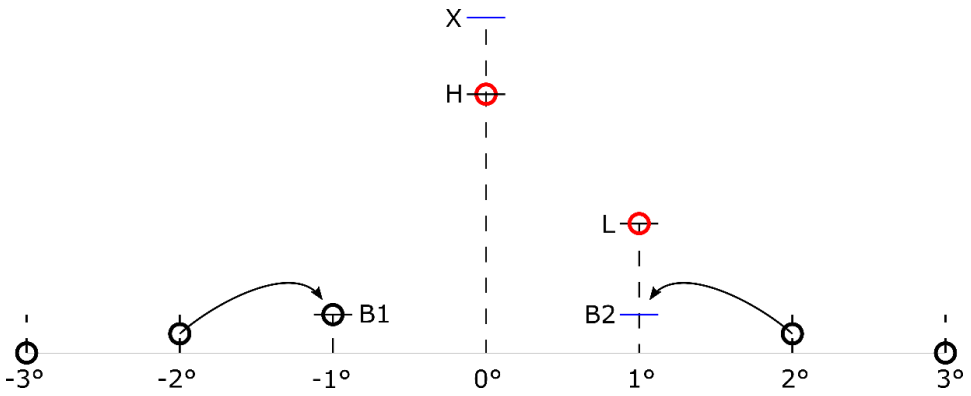

Figure A.4. Peak signal level correction points.

Assuming that the data points are measured at equal time intervals, and therefore that the error ratio between successive points is the same, the following quadratic relation is obtained:

$$\frac{\mathrm{H}-\mathrm{B1}}{\mathrm{X}-\mathrm{B1}} = 1 - \frac{\mathrm{L}-\mathrm{B2}}{\mathrm{X}-\mathrm{B2}} = \frac{\mathrm{X}-\mathrm{L}}{\mathrm{X}-\mathrm{B2}}$$

The two solutions of this quadratic relation give the corrected peak data point X, and a refinement of base point B2.

B. Circling the Square: elements partly outside the diffraction hemisphere

The discrete algorithms for power calculation $P_{\alpha,\beta}$ such as Equation (4.17) give the 2D power map for each matrix element corresponding to a scatter angle. Algorithms for intensity distributions $I_{2D}(\alpha,\beta)$ or $I_{1D}(\beta-\beta_0)$ such as Equations (4.20) or (4.31) require normalization by the solid angle $\Delta\Omega_{\alpha,\beta}$ corresponding to those scattering

matrix elements. This is straightforward for most matrix elements that are fully inside the diffraction hemisphere, but not so for elements that are partially outside, such as the ones colored in Figure B.1. The center (α, β) of the blue-colored element is inside the unit circle, but part of the square $\Delta\alpha \times \Delta\beta$ (and therefore part of the power contained in that element) is outside. Likewise, the center (α, β) of the red-colored element is outside, but part of its square $\Delta\alpha \times \Delta\beta$ is inside the unit circle. Depending on the AFM scan size and refractive index of the medium into which scattering occurs, such elements will constitute a sizable angle range (around 75° to 90° for L=25µm and n_s=1).

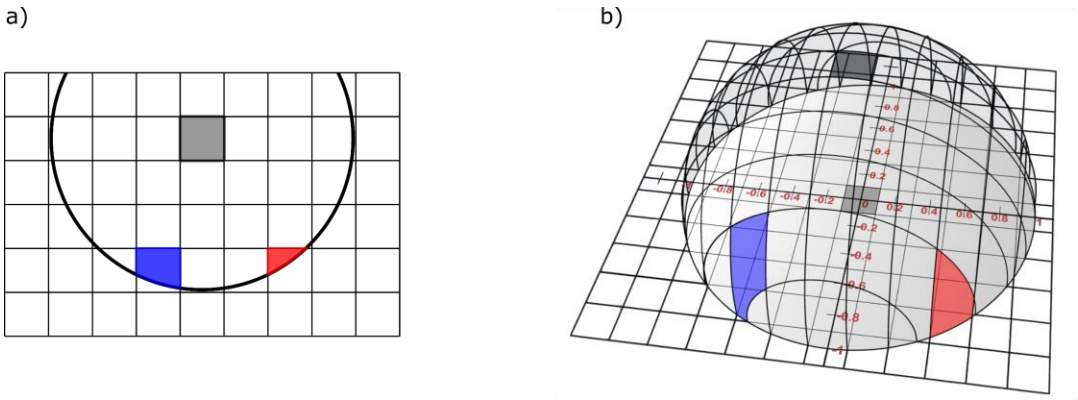

Figure B.1. Matrix elements partly inside the unit circle.

For such elements, the area contained inside the unit circle (illustrated in the colored parts of Figure B.1a) and the area projected onto the unit hemisphere (giving corresponding solid angles, as illustrated in Figure B.1b) are calculated numerically using surface integrals. Furthermore, for such elements, the radial distance to the center of the unit circle is calculated not from the center of the square $\Delta\alpha \times \Delta\beta$, which can be outside the unit circle (as in the red-colored elements), but from the geometric center of the polygon remaining inside the unit circle. This polygon can have three, four or five corners, depending on how many corners of the square $\Delta\alpha \times \Delta\beta$ are outside the unit circle.

Finally, the intensity is calculated by multiplying the scattered power for that matrix element by the area ratio of the square remaining inside the unit circle, and dividing by the corresponding solid angle.

C. Spectral leakage problems

A consequence of the finite nature of the 2D FFT operation is the spectral leakage phenomenon, illustrated in Figure C.1. The FFT operation treats the phase screen as a periodic function at the boundaries, which is not the case for random isotropic textured samples. The discontinuity at the edges result in a characteristic “cross” pattern after the 2D FFT. Samples with larger lateral features compared to their AFM image size (such as samples A, B and C) tend to suffer more from this effect. The preferred solution is to use a window function to smoothly decrease the height profile to zero near the image edges. The use of a well-selected window function can eliminate almost the entire leakage artefact without significantly altering the power distribution of the central elements.

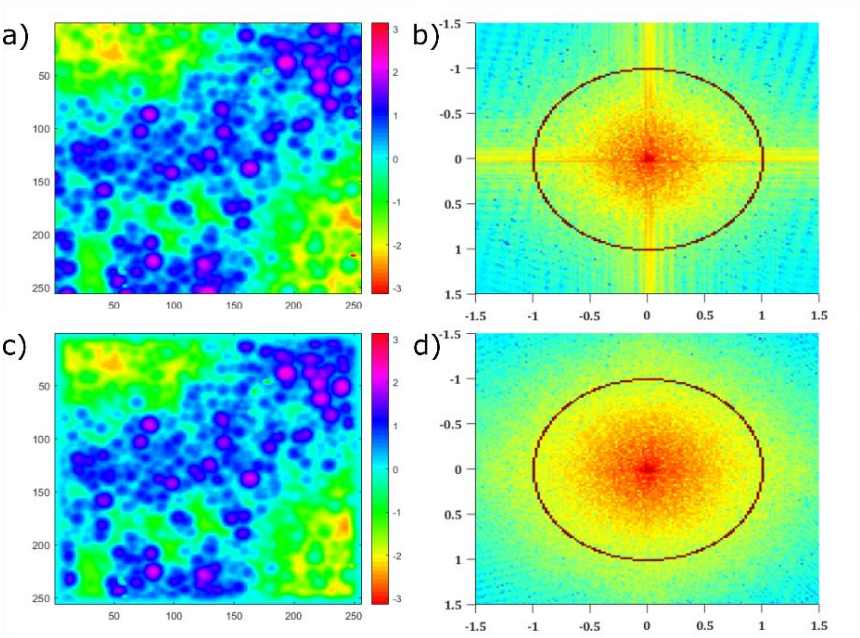

Figure C.1. a) Phase screen resulting from normal incidence reflection for sample A, and b) its corresponding 2D power distribution map. c) and d) The same results with a tapered cosine (Tukey) window function (with parameter 0.1) [102] applied to the AFM image.

CURRICULUM VITAE

GÜNÖVEN, METE

28 January 1984, Ankara, Turkey
mete.gunoven@gmail.com,
+90 532 622 86 16
Class B driver's license

EDUCATION

Degree	Institution	Graduation
Ph.D.	Middle East Technical University (METU) Micro and Nanotechnology	2020
M.Eng.	Institut National des Sciences Appliquées (INSA) de Lyon Science et Génie des Matériaux	2007
High School	Lycée Charles de Gaulle, Ankara	2002

WORK EXPERIENCE

Year	Place	Function
2020	Kalyon Solar Technologies and Production Corporation	Research Engineer
2015 - 2017	Advanced Research Laboratories, Bilkent University Quantum Cascade Laser development project Characterization specialist	Research Assistant
2012 - 2017	Center for Solar Energy Research and Applications (GÜNAM), METU Responsible for Optical and Electrical Characterization	Research Assistant
2007	Nanofabrication and Nanocharacterisation Research Center (CRN2), University of Sherbrooke, Canada Design and fabrication of a THz emission antenna	Intern Engineer
2006	Composite Materials Research Center, METU Manufacturing parameters of aluminum foams	Intern Engineer

KNOWLEDGE AND SKILLS

Languages	English, French
Computer Skills	C++, Matlab, Labview, Origin, Comsol AutoCAD, Inkscape, Photoshop, MS Office

PERSONAL INTERESTS

Scale model building
Swimming, competitive level rowing in high-school